An Asymptotic Solution of the Problem
of Nonlinear Waves in a Viscous Liquid

D. F. Belonozhko, A. I. Grigor'ev, and S. O. Shiryaeva

Yaroslavl State University, Yaroslavl, Russia
e-mail: grigr@uniyar.ac.ru
Received April 11, 2002

Abstract—A strict solution of the problem of temporal evolution of the shape of a periodic wave on the surface of a viscous infinitely deep liquid is obtained for the first time in an approximation quadratic in the wave amplitude. © 2002 MAIK "Nauka/Interperiodica".

Introduction. Despite a long history of investigations of finite-amplitude waves, all strict results were obtained within the framework of the ideal liquid approximation (see, e.g., [1–7] and references therein). The most correct attempts at accounting for the influence of viscosity upon a nonlinear evolution of the shape of the free liquid surface were made using the approximation of small viscosity within the framework of the boundary layer theory [8–10] applicable only in the case of large Reynolds numbers. However, a quite correct analytical formulation of the problem of determining the shape of a wave propagating on the surface of a viscous, infinitely deep liquid is possible in an approximation quadratic in the wave amplitude [11].

The study of the wave motions of finite amplitude in a viscous liquid is important from the standpoint of both the basic theory and numerous technical applications. For example, an analysis performed within the framework of an approximation quadratic in the wave amplitude [12–14] predicted the possibility of instability of a liquid surface with respect to elastic stresses, inactive surfactants contained in the liquid, and redistribution of the electric charge at a finite velocity over the surface. Detailed theoretical analysis of these effects is also possible only within high-order approximations in the wave amplitude. Our study has been performed in this context.

Formulation of the general problem. Consider an incompressible liquid with the density ρ, kinematic viscosity ν, and surface tension γ occupying the half-space $z \leq 0$ in the Cartesian coordinate system $OXYZ$ and occurring under the action of a gravitational field $\mathbf{g}$ ($\mathbf{g} \parallel -\mathbf{n}_z$) and a constant external pressure P_0. Our aim is to describe the profile of a wave freely propagating over the liquid surface along the OX axis in an approximation quadratic in the wave amplitude.

Let $u = u(x, z, t)$ and $v = v(x, z, t)$ be the horizontal and vertical components of the velocity field of the liquid; $\mathbf{n}_x$ and $\mathbf{n}_z$ will denote the unit vectors in the horizontal and vertical directions, respectively. The required analytical expression for the wave profile $\xi = \xi(x, t)$ and the velocity field $\mathbf{U}(\mathbf{r}, t) = u\mathbf{n}_x + v\mathbf{n}_z$ must be a solution to the following boundary- and initial-value problem:

$$\frac{\partial \mathbf{U}}{\partial t} + \mathrm{rot}(\mathbf{U}) \times \mathbf{U} = -\mathrm{grad}\left(\frac{1}{\rho}p + \frac{U^2}{2} + gz\right) + \nu\Delta\mathbf{U};$$

$$\mathrm{div}\mathbf{U} = 0;$$

$$z = \xi: \ \frac{\partial\xi}{\partial t} + u\frac{\partial\xi}{\partial x} = v;$$

$$p - 2\rho\nu\mathbf{n}\cdot((\mathbf{n}\cdot\boldsymbol{\nabla})\mathbf{U}) - P_0 = \gamma\mathrm{div}(\mathbf{n});$$

$$\boldsymbol{\tau}\cdot((\mathbf{n}\cdot\boldsymbol{\nabla})\mathbf{U}) + \mathbf{n}\cdot((\boldsymbol{\tau}\cdot\boldsymbol{\nabla})\mathbf{U}) = 0;$$

$$z \longrightarrow -\infty: \ U \longrightarrow 0;$$

$$t = 0: \ x = F(x);$$

$$z \leq \xi: \ \mathbf{U} = \mathbf{U}^0 = \mathbf{U}^0(x, z) = u^0(x, z)\mathbf{n}_x + v^0(x, z)\mathbf{n}_z,$$

where t is the time; $\boldsymbol{\tau}$ and $\mathbf{n}$ are the unit vectors of tangent and normal to the surface.

Second-order problem formulation. The procedure of separating the above problem into problems of the first and second order of smallness was described in detail elsewhere [11]. The solution to the first-order problem is well known and will not be considered here. The main result of the first-order analysis is the dispersion equation

$$\nu^2(q^2 + k^2)^2 + \omega_0^2 = 4q\nu^2 k^3;$$

$$\omega_0^2 = k(g + k^2\gamma/\rho); \quad q = \sqrt{k^2 + S/\nu},$$

where S is the complex frequency. The nonlinear analysis will employ only one solution of the dispersion equation, namely, that occurring on the upper sheet of the Riemann surface and denoted below by S.

Representing the vector field of velocities in the second-order approximation $\mathbf{U}_2(\mathbf{r}, t)$ via two scalar fields, $\varphi_2 \equiv \varphi_2(\mathbf{r}, t)$ and $\psi_2 \equiv \psi_2(\mathbf{r}, t)$,

$$\mathbf{U}_2(\mathbf{r}, t) = \hat{\mathbf{N}}_1 \varphi_2 + \hat{\mathbf{N}}_2 \psi_2;$$

$$\hat{\mathbf{N}}_1 \equiv \mathbf{n}_x \frac{\partial}{\partial x} + \mathbf{n}_z \frac{\partial}{\partial z}; \quad \hat{\mathbf{N}}_2 \equiv -\mathbf{n}_z \frac{\partial}{\partial z} + \mathbf{n}_z \frac{\partial}{\partial x},$$

we can mathematically formulate the second problem as follows [11]:

$$\frac{\partial \psi_2}{\partial t} - \nu \Delta \psi_2$$
$$= a^2(\eta_0 \exp(2L) + (\eta_1 \cos(h) + \eta_2 \sin(h))\exp(2L)$$
$$+ (\Pi_1 \cos(2\theta + h) + \Pi_2 \sin(2\theta + h))\exp(L+1))$$
$$\times \exp(2T); \quad \Delta \varphi_2 = 0;$$

$$z = 0: \quad \frac{\partial \xi_2}{\partial t} - \frac{\partial \varphi_2}{\partial z} - \frac{\partial \psi_2}{\partial x} = a^2(H_1 \cos(2\theta) - H_2 \sin(\theta))\exp(2T); \tag{1}$$

$$-\rho g \xi_2 - \frac{\partial \varphi_2}{\partial t} - 2\rho\nu\left(\frac{\partial^2 \varphi_2}{\partial z^2} + \frac{\partial^2 \psi_2}{\partial x \partial z}\right) + \gamma \frac{\partial^2 \xi_2}{\partial x^2} = a^2(Z_1 + Z_1 \cos(2\theta) - Z_2 \sin(2\theta))\exp(2T); \tag{2}$$

$$2\frac{\partial^2 \varphi_2}{\partial x \partial z} + \frac{\partial^2 \psi_2}{\partial x^2} - \frac{\partial^2 \psi_2}{\partial z^2} = a^2(2H_2 - \kappa_1 + G_1 \cos(2\theta) - G_2 \sin(2\theta))\exp(2T); \tag{3}$$

$$z \longrightarrow -\infty: \quad \frac{\partial \varphi_2}{\partial x} - \frac{\partial \psi_2}{\partial z} \longrightarrow 0; \quad \frac{\partial \varphi_2}{\partial z} + \frac{\partial \psi_2}{\partial x} \longrightarrow 0. \tag{4}$$

$$S_R = \mathrm{Re}(S); \quad S_I = \mathrm{Im}(S);$$

$$q_R = \mathrm{Re}[\sqrt{k^2 + S/\nu}]; \quad q_I = \mathrm{Im}[\sqrt{k^2 + S/\nu}];$$

$$D_0 = S_R + 2\nu k^2; \quad C_1 = q_R^2 - q_I^2;$$

$$C_2 = 2q_R q_I; \quad C_3 = C_1 - k^2;$$

$$l = kz; \quad L = q_R z; \quad h = q_I z;$$

$$\theta = S_I t - kx; \quad T = S_R t;$$

$$\eta_0 = -(\nu k)^2 C_2 2 q_I;$$

$$\eta_1 = \frac{\nu k}{(k + q_R)^2 + q_I^2}(S_I B_1 - D_0 B_2);$$

$$\eta_2 = \frac{\nu k}{(k + q_R)^2 + q_I^2}(D_0 B_1 + S_I B_2);$$

$$\Pi_1 = \frac{\nu k}{(3k + q_R)^2 + q_I^2}(D_0 M_2 + S_I M_1);$$

$$\Pi_2 = \frac{\nu k}{(3k + q_R)^2 + q_I^2}(D_0 M_1 - S_I M_2);$$

$$B_1 = (k + q_R)C_3 + q_I C_2; \quad B_2 = (k + q_R)C_2 - q_I C_3;$$

$$M_1 = (3k + q_R)C_3 + q_I C_2;$$

$$M_2 = (3k + q_R)C_2 - q_I C_3;$$

$$H_1 = k(D_0 - 2\nu k q_R); \quad H_2 = k(S_I - 2\nu k q_I);$$

$$Z_1 = \nu k^2 \rho(D_0 + 2\nu(q_I^2 - q_R^2)) - \frac{\rho}{2}(S_I^2 - S_R^2 D_0);$$

$$G_1 = -k(2H_2 + \kappa_1);$$

$$Z_2 = \nu k^2 \rho(S_I - 4\nu q_I q_R) + \rho S_I(S_R + \nu k^2);$$

$$G_2 = k(2H_1 + \kappa_2);$$

$$\kappa_1 = kS_I - q_I(k^2 - q_I^2 + 3q_R^2)\nu;$$

$$\kappa_2 = kS_R + \nu(k^2(2k - q_R) + q_R(3q_I^2 - q_R^2)).$$

Here, relation (1) is the kinematic condition on the free liquid surface; (2) is the condition for the pressure on the free surface; (3) is the condition of zero tangential stresses on the free surface; and (4) is the condition of the absence of motions at the infinite depth. The S_R value entering into the definition of T is negative; this quantity characterizes the wave damping in the linear approximation.

Solution of the problem. A partial solution to the total problem of determining the profile of a wave propagating on the surface of the infinitely deep liquid, valid to within second-order terms in deviation from the equilibrium plane, is as follows:

$$\xi = a\cos(\theta)\exp(T)$$
$$+ a^2(\Lambda_1 \cos(2\theta) - \Lambda_2 \sin(2\theta))\exp(2T); \tag{5}$$

$$J_1 = \mathrm{Re}[\sqrt{2(k^2 + q_I^2)}]; \quad J_2 = \mathrm{Im}[\sqrt{2(k^2 + q_I^2)}];$$

$$\alpha_1 = q_I^2 + q_R^2; \quad \alpha_2 = q_I^2 - q_R^2;$$

$$D_1 = k - q_R; \quad D_2 = 3k + q_R; \quad D_3 = k + q_R;$$

$$D_4 = 4q_I(k^3 - 3k^2 q_R + k(q_I^2 - 5q_R^2) - q_R\alpha_1);$$

$$D_5 = 4kq_I(5k^4 - 8k^3 q_R + 2k^2(3q_I^2 - 7q_R^2) + \alpha_1^2);$$

$$D_6 = 2(3k^4 + 4k^2 q_I^2 + q_I^4$$
$$+ 4k(k^2 + 2q_I^2)q_R - 2k^2 q_R^2 - 4kq_R^3 - q_R^4);$$

$$D_8 = 3k^2 + \alpha_1;$$

$$D_7 = 21k^6 + 22k^5 q_R + k^4(27q_I^2 - 25q_R^2) + 6kq_R\alpha_1^2$$
$$+ \alpha_1^3 + k^2\alpha_1(7q_I^2 + 3q_R^2) + 4k^3(15q_I^2 q_R - 7q_R^3);$$

$$b_1 = 2(3k^3 + k^2 q_R + 3k\alpha_2 - q_R\alpha_1);$$

$$b_2 = 21k^5 + k^4 q_R + 2\alpha_2 k^2(13k + q_R) + \alpha_1^2(5k + q_R);$$

$$b_3 = -q_I(7k^2 - q_I^2 + 2kq_R - q_R^2);$$

$$b_4 = 2k^2(9k^3 + 5kq_I^2 + 15k^2 q_R + q_I^2 q_R + 7kq_R^2 + q_R^3);$$

$$b_5 = -2q_I(k^2 + q_I^2 + 6kq_R + q_R^2);$$

$$b_6 = -q_I(k^4 + 32k^3 q_R + 2k^2\alpha_2 + \alpha_1^2);$$

$$\Omega_1 = k\nu(q_I^2 + D_2^2)^{-1};$$

$$b_7 = -3k^2 + 5kq_I^2 - k^2 q_R + q_I^2 q_R + 3kq_R^2 + q_R^3;$$

$$\Omega_2 = \Omega_1(4(S_R^2 + S_I^2) + 4\nu(q_I^2 + D_1 D_2)S_R$$
$$- 8\nu q_I D_3 S_I + \nu^2(q_I^2 + D_1^2)(q_I^2 + D_2^2))^{-1};$$

$$\delta_1 = 2k\rho\Omega_1$$
$$\times ((D_1 D_2 - q_I^2)S_R + 4kq_I S_I + 2\nu k^2(D_1 D_2 - q_I^2));$$

$$\delta_2 = 2k\rho\Omega_1(-4kq_I S_R + (D_1 D_2 - q_I^2)S_I - 8\nu k^3 q_I);$$

$$d_1 = -\Omega_2(D_4(S_R^2 + S_I^2) + \nu D_5 S_R$$
$$- \nu(q_I^2 + D_3^2)^2(D_1 D_2 - q_I^2)S_I$$
$$+ 8\nu^2 k^3 q_I(D_1^2 + q_I^2)(D_2 D_3 + q_I^2));$$

$$d_2 = \Omega_2(D_6(S_R^2 + S_I^2) + \nu D_7 S_R - 4\nu kq_I(q_I^2 + D_3^2)^2 S_I$$
$$+ 2\nu^2 k^2(q_I^2 + D_1^2)((D_8 + 4kq_R)^2 - 4k^2 q_I^2);$$

$$\chi_1 = -2\Omega_2(b_1(S_R^2 + S_I^2) + \nu b_2 S_R$$
$$+ \nu(q_I^2 + D_3^2)b_3 S_I + \nu^2(q_I^2 + D_1^2)b_4);$$

$$\chi_2 = -2\Omega_2(b_5(S_R^2 + S_I^2) + \nu b_6 S_R$$
$$+ \nu(q_I^2 + D_3^2)b_7 S_I + 2\nu^2 k^2 q_I(D_1^2 + q_I^2)(D_1 D_2 - q_I^2));$$

$$K_1 = 2\rho(\chi_1 + H_1); \quad K_2 = 2\rho(\chi_2 + H_2);$$

$$K_3 = 4k\rho(d_1 q_I + d_2 D_3 - G_2 + 2kH_1);$$

$$K_4 = -4k\rho(d_2 q_I - d_1 D_3 + G_1 + 2kH_2);$$

$$K_5 = 2k(-Z_1 + \delta_1 + 2\nu\rho(q_I\chi_2 + k\chi_1 - q_R\chi_1 + 2kH_1));$$

$$K_6 = 2k(-Z_2 + \delta_2 - 2\nu\rho(q_R\chi_2 + q_I\chi_1 - k\chi_2 - 2kH_1));$$

$$K_7 = -8\nu k^2\rho(d_1 q_I + d_2 D_3 - G_2 + 2k(\chi_1 + 2H_1));$$

$$K_8 = 8\nu k^2\rho(d_2 q_I - d_1 D_3 + G_1 + 2k(\chi_2 + 2H_2));$$

$$K_9 = 8k^3(Z_1 - \delta_1$$
$$+ 2\nu\rho[d_1 q_I - G_2 - q_I\chi_2 + D_3(d_2 + \chi_1) + 2kH_1]);$$

$$\beta_1 = 4\rho; \quad \beta_2 = 16\nu k^2\rho;$$

$$K_{10} = 8k^3(Z_2 - \delta_2$$
$$+ 2\nu\rho\{d_2 q_I + G_1 + k\chi_2 - D_3(d_1 - \chi_2) + 2kH_2\});$$

$$\beta_3 = 2k(\rho g + 4k^2\gamma);$$

$$\hat{S} = \begin{bmatrix} S_R^2 & S_R S_I & S_I^2 & S_R & S_I & 1 \end{bmatrix};$$

$$\hat{J} = \begin{bmatrix} J_R^2 & J_R J_I & J_I^2 & J_R & J_I & 1 \end{bmatrix}^T;$$

$$\hat{\zeta}_1 = \begin{bmatrix} \beta_1 & 0 & -\beta_1 & 0 & 0 & 4k^2\beta_1 \\ 0 & -4\beta_1 & 0 & 0 & 0 & 0 \\ -\beta_1 & 0 & \beta_1 & 0 & 0 & -4k^2\beta_1 \\ \beta_2 & 0 & -\beta_2 & -4k\beta_2 & 0 & 4k^2\beta_2 \\ 0 & -2\beta_2 & 0 & 0 & 4k\beta_2 & 0 \\ \beta_3 & 0 & -\beta_3 & 0 & 0 & -4k^2\beta_3 \end{bmatrix};$$

$$\hat{\zeta}_3 = \begin{bmatrix} 0 & 0 & 0 & K_1 & -K_2 & K_5 \\ 0 & 0 & 0 & -2K_2 & -2K_1 & -2K_6 \\ 0 & 0 & 0 & -K_1 & K_2 & -K_5 \\ 0 & 0 & 0 & 0 & 0 & K_7 \\ 0 & 0 & 0 & 0 & 0 & K_8 \\ 0 & 0 & 0 & K_3 & K_4 & K_9 \end{bmatrix}^T;$$

$$\hat{\zeta}_2 = \begin{bmatrix} 0 & 2\beta_1 & 0 & 0 & 0 & 0 \\ 2\beta_1 & 0 & -2\beta_1 & 0 & 0 & 8k^2\beta_1 \\ 0 & -2\beta_1 & 0 & 0 & 0 & 0 \\ 0 & 2\beta_2 & 0 & 0 & -4k\beta_2 & 0 \\ \beta_2 & 0 & -\beta_2 & -4k\beta_2 & 0 & 4k^2\beta_2 \\ 0 & 2\beta_3 & 0 & 0 & 0 & 0 \end{bmatrix};$$

$$\hat{\zeta}_3 = \begin{bmatrix} 0 & 0 & 0 & K_2 & K_1 & K_6 \\ 0 & 0 & 0 & 2K_1 & -2K_2 & 2K_5 \\ 0 & 0 & 0 & -K_2 & -K_1 & -K_6 \\ 0 & 0 & 0 & 0 & 0 & -K_8 \\ 0 & 0 & 0 & 0 & 0 & K_7 \\ 0 & 0 & 0 & -K_4 & K_3 & K_{10} \end{bmatrix}^T ;$$

$$\Lambda_1 = \frac{(\hat{S}\hat{\zeta}_1\hat{J})(\hat{S}\hat{\zeta}_3\hat{J}) + (\hat{S}\hat{\zeta}_2\hat{J})(\hat{S}\hat{\zeta}_4\hat{J})}{(\hat{S}\hat{\zeta}_1\hat{J})^2 + (\hat{S}\hat{\zeta}_2\hat{J})^2};$$

$$\Lambda_2 = \frac{(\hat{S}\hat{\zeta}_1\hat{J})(\hat{S}\hat{\zeta}_4\hat{J}) - (\hat{S}\hat{\zeta}_2\hat{J})(\hat{S}\hat{\zeta}_3\hat{J})}{(\hat{S}\hat{\zeta}_1\hat{J})^2 + (\hat{S}\hat{\zeta}_2\hat{J})^2}.$$

The set of quantities in square brackets is considered as a matrix; symbol T indicates the operation of matrix transposition. In the formulas for Λ_1 and Λ_2, expressions in parentheses are the matrix products.

It is interesting to compare the solution obtained to the results of Nayfeh [4], who studied an analogous problem for the ideal liquid. According to [4], direct expansion of the solution in an approximation quadratic in the wave amplitude yields the following expressions:

$$\xi = a\cos(\theta_0) + a^2\Lambda_0\cos(2\theta_0);$$

$$\Lambda_0 = \frac{(\rho g k + \gamma k^3)}{2(\rho g - 2\gamma k^2)}; \quad \theta_0 = kx - \omega_0 t. \tag{6}$$

For $\gamma = 0$, the solution represents a Stokes wave [1, 2]. For $\nu \longrightarrow 0$, it can be readily shown that expression (5) for the wave profile in a viscous liquid converts into formula (6) for the ideal liquid.
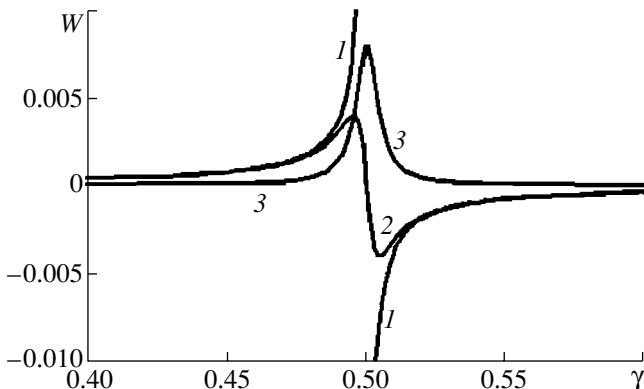
Plots of the amplitudes of dimensionless quadratic corrections $W(\gamma)$ to the wave profile in Eqs. (5) and (6) versus the dimensionless surface tension (for $a = 0.01$): (*1*) for the ideal liquid, $W(\gamma) = a^2\Lambda_0(\gamma)$; (*2, 3*) for a viscous liquid with $\nu = 10^{-3}$, $W(\gamma) = a^2\Lambda_1(\gamma, \nu)$ and $a^2\Lambda_2(\gamma, \nu)$, respectively.

A comparative analysis of the solutions (5) and (6) obtained for the viscous and ideal liquids, respectively, showed that most significant difference takes place for the dimensionless parameters corresponding to a resonance interaction of modes. For $\gamma k^2 = 0.5\rho g$, Eq. (6) for the ideal (nonviscous) liquid indicates that the correction quadratic in the first-order wave amplitude becomes infinitely large, which corresponds to the principal mode producing a resonance amplification of the wave with a twice smaller wavelength.

The figure, plotted in dimensionless variables ($k = g = \rho = 1$), shows the amplitudes of the second terms of solutions (5) and (6) as functions of the dimensionless surface tension γ for the dimensionless parameters $\nu = 10^{-3}$ and $a = 0.01$. This selection of the dimensionless variables allows the results obtained within the framework of the viscous and nonviscous liquid models to be compared for a wave on the water surface with a wavelength of 2.4 cm and an amplitude of 0.3 mm. As can be seen from this figure, the two solutions coincide in the region of γ far from the resonance. Near the resonance value of $\gamma = 0.5$, the solution, taking into account the viscosity, has a nonzero coefficient Λ_2 at $\sin(2\theta)$. For this reason, the phase of the wave determined in the second-order approximation is shifted relative to that of the principal wave. The amplitude of the square correction $\sqrt{\Lambda_1^2 + \Lambda_2^2}$ remains smaller as compared to the amplitude of the principal wave ($a = 0.01$) even at a resonance value of $\gamma = 0.5$. This implies that the solution (5) is valid at all γ values, whereas the solution (6) based on the nonviscous approximation predicts a resonant growth in the amplitude.

Conclusion. An asymptotic solution of the problem of wave propagation on the surface of an infinitely deep liquid of arbitrary viscosity, valid in an approximation quadratic in the wave amplitude, generalizes the concept of the "Stokes wave" (determined for the ideal liquid) to the case of viscous liquids. A comparison of the solution obtained to that known for the ideal liquid shows that even a small viscosity plays a significant role in the wave profile formation under the conditions of resonance intermode interaction.

REFERENCES

1. J. J. Stoker, *Water Waves* (Wiley, New York, 1957; Inostrannaya Literatura, Moscow, 1959).

2. G. B. Whitham, *Linear and Nonlinear Waves* (Wiley, New York, 1974; Mir, Moscow, 1977).

3. R. V. Gol'dshteĭn and V. A. Gorodtsov, *Mechanics of Continuous Media* (Nauka, Moscow, 2000), Part 1.

4. A. H. Nayfeh, J. Fluid Mech. **48**, 385 (1971).

5. I. Shugan and K. Voliak, J. Fluid Mech. **368**, 321 (1998).

6. K. Trulsen and I. Kliakhandler, Phys. Fluids **12** (10), 2432 (2000).

7. M. S. Longet-Higgins, J. Fluid Mech. **423**, 275 (2000).

8. I. M. Mindlin, Izv. Akad. Nauk, Mekh. Zhidk. Gaza, No. 3, 135 (1994).

9. S. V. Nesterov, Izv. Akad. Nauk, Mekh. Zhidk. Gaza, No. 4, 116 (1995).

10. A. V. Fedorov and W. K. Melvil, J. Fluid Mech. **354**, 1 (1998).

11. S. O. Shiryaeva, D. F. Belonozhko, V. B. Svetovoǐ, and A. I. Grigor'ev, Preprint No. 31, IMI RAN (Yaroslavl, 2001).

12. S. O. Shiryaeva, A. I. Grigor'ev, and V. A. Koromyslov, Pis'ma Zh. Tekh. Fiz. **22** (4), 89 (1996) [Tech. Phys. Lett. **22**, 173 (1996)].

13. S. O. Shiryaeva, D. F. Belonozhko, and A. I. Grigor'ev, Zh. Tekh. Fiz. **68** (2), 22 (1998) [Tech. Phys. **43**, 151 (1998)].

14. D. F. Belonozhko and A. I. Grigor'ev, Pis'ma Zh. Tekh. Fiz. **25** (22), 1 (1999) [Tech. Phys. Lett. **25**, 884 (1999)].

Translated by P. Pozdeev

An Analytical Solution of the Problem
of Second-Order Thermal Slip

V. N. Popov

Pomorskiĭ State University, Arkhangelsk, Russia
e-mail: popov.vasily@pomorsu.ru
Received April 18, 2002

Abstract—Results obtained by applying exact analytical methods to description of the second-order thermal slip are presented and compared to the published data. © *2002 MAIK "Nauka/Interperiodica".*

Gradients of the hydrodynamic quantities (temperature, mass flow rate, concentration) in a rarefied gas lead to a phenomenon of the gas slip along a streamlined surface. The gas slip effect on a plane solid surface have been studied in sufficient detail using both exact and approximate methods. A less studied aspect of this problem is taking into account the second-order derivatives of the hydrodynamic quantities in the boundary conditions. This is necessary, in particular, for constructing a theory of the thermophoresis of high-thermal-conductivity particles in which case the second-order effects play a determining role. An allowance for these effects led to theoretical predictions of a negative (proceeding in the direction of temperature gradient) thermophoresis of aerosol particles at small Knudsen numbers ($0.01 < \mathrm{Kn} < 0.3$) [1–4]. Taking into account that the published results were obtained by numerical [1, 2] or approximate [3, 4] methods, studying the problem by exact analytical methods would be of importance from the standpoint of both the basic theory and applications.

Consider a simple monoatomic gas filling the half-space $x > 0$ bounded by a plane solid surface $x = 0$. In the gas, let a temperature gradient in the normal direction be created. We assume that the temperature gradient is slowly varying along the surface in the direction of the y axis. Thus, the $\partial T/\partial x$ and $\partial^2 T/\partial x \partial y$ values are nonzero, the first of these quantities leading to a temperature jump at the solid boundary and the second, to the so-called second-order thermal slip.

The rate of the gas slip relative to the streamlined surface is given by the expression

$$U|_S = K_T \beta_R \lambda \nu k, \quad k = \frac{1}{T_\omega} \frac{\partial^2 T}{\partial x \partial y}\bigg|_S,$$

where S and T_ω are the surface area and temperature of the gas particles, respectively; λ is the mean free path length of the gas particles; ν is the kinematic viscosity; K_T is the thermal slip coefficient of a rarefied gas at the plane solid surface; and β_R is the second-order thermal

slip coefficient. Once the K_T value is known, the problem reduces to determining the β_R value.

Let us assume that

$$\frac{\lambda}{T_\omega}\bigg|\frac{\partial T}{\partial x}\bigg| \ll 1, \quad \frac{\lambda^2}{T_\omega}\bigg|\frac{\partial^2 T}{\partial x \partial y}\bigg| \ll 1.$$

In this case, the problems admits linearization whereby the distribution of gas molecules with respect to coordinates and velocities can be represented as

$$f = f^{(0)}(1 + C_y \varphi(x, C_x)),$$

where $f^{(0)}$ is the local equilibrium distribution function in the Chapman–Enskog approximation and $\varphi(x, C_x)$ is a solution to the equation ($\mu = C_x$)

$$\mu \frac{\partial \varphi}{\partial x} + \varphi(x, \mu) = \frac{1}{\sqrt{\pi}} \int_{-\infty}^{\infty} \exp(-\tau^2)\varphi(x, \tau)d\tau$$

$$- k[Z_1(x, \mu) + \gamma(\mu^2 + 1/2)Z_2(x, \mu)], \qquad (1)$$

$$Z(x, \mu) = \int_0^{\infty} \exp(-x/\eta)F(\eta, \mu)A(\eta)d\eta,$$

$$F(\eta, \mu) = \eta P \frac{1}{\eta - \mu} I + \exp(\eta^2)\Omega(\eta)\delta(\eta - \mu),$$

$$\Omega(\eta) = \sqrt{\pi}\Delta^{-1}(\eta) + \eta t(\eta)I,$$

$$\Delta^{-1}(\eta) = \frac{1}{2}\begin{bmatrix} -(\eta^2 - 5/2) & -\gamma(\eta^2 - 3/2) \\ \gamma^{-1} & 3 \end{bmatrix},$$

$$t(\eta) = \int_{-\infty}^{\infty} \frac{\exp(-\mu^2)d\mu}{\mu - \eta} = -2\sqrt{\pi}\exp(-\eta^2)\int_0^{\eta}\exp(t^2)dt,$$

$$A(\eta) = [A_1(\eta), A_2(\eta)]^t,$$

$$Z(x, \mu) = [Z_1(x, \mu), Z_2(x, \mu)]^t$$

with the boundary conditions

$$\varphi(0, \mu) = 0 \quad (\mu > 0), \quad \varphi(\infty, \mu) = 2U|_S. \quad (2)$$

In Eq. (1), $Z(x, \mu)$ is the distribution function from a problem of the temperature jump at a plane solid surface [5], $A(\eta)$ are the coefficients of expansion in eigenvectors of the continuum for the solution to a problem of the temperature jump at a plane solid surface, symbol t denotes transposition, $\gamma^2 = 2/3$, Px^{-1} is the distribution with respect to the mean value of the integral of x^{-1}, and $\delta(x)$ is the Dirac delta function.

Introducing the column vector $Y(x, \mu) = [\varphi(x, \mu), 0]^t$, we can rewrite Eqs. (1) and (2) in the vector form:

$$\mu \frac{\partial Y}{\partial x} + Y(x, \mu)$$

$$= \frac{1}{\sqrt{\pi}} \int_{-\infty}^{\infty} \exp(-\tau^2) Y(x, \tau) d\tau - kK(\mu)Z(x, \mu), \quad (3)$$

$$Y(0, \mu) = \begin{bmatrix} 0 \\ 0 \end{bmatrix} \quad (\mu > 0), \quad Y(\infty, \mu) = \begin{bmatrix} 2U|_S \\ 0 \end{bmatrix}, \quad (4)$$

$$K(\mu) = \begin{bmatrix} 1 & \gamma(\mu^2 + 1/2) \\ 0 & 0 \end{bmatrix}.$$

A general solution to Eq. (3) will be found in the form of a sum of a general solution to the corresponding homogeneous equation and a partial solution to the inhomogeneous equation. The former is as follows [6]:

$$Y_0(x, \mu) = B_0 + B_1(x - \mu)$$

$$+ \int_0^{\infty} \exp(-x/\eta)\Phi(\eta, \mu)B(\eta)d\eta,$$

$$\Phi(\eta, \mu) = \frac{1}{\sqrt{\pi}}\eta P \frac{1}{\eta - \mu} + \exp(\eta^2)\lambda(\eta)\delta(\eta - \mu),$$

$$\lambda(z) = 1 + \frac{1}{\sqrt{\pi}} z \int \frac{\exp(-\eta^2)}{n - z} d\eta,$$

where B_0, B_1, and $B(\eta)$ are unknown column vectors, the components of which have to be determined.

A partial solution to the inhomogeneous equation (3) can be found in the following form:

$$Y_1(x, \mu) = \int_0^{\infty} \exp(-x/\eta)G(\eta, \mu)d\eta, \quad (5)$$

$$\int_0^{\infty} \exp(-\mu^2)G(\eta, \mu)d\mu = 0. \quad (6)$$

Substituting expression (5) into Eq. (3), we obtain the characteristic equation

$$\left(1 - \frac{\mu}{\eta}\right)G(\eta, \mu) = -kK(\mu)F(\eta, \mu)A(\eta),$$

the solution to which in the space of generalized functions is

$$G(\eta, \mu)$$

$$= k\eta P \frac{1}{\eta - \mu}K(\mu)F(\eta, \mu)A(\eta) + g(\eta)\delta(\eta - \mu). \quad (7)$$

The explicit form of $g(\eta)$ is obtained upon substituting (7) into (6):

$$g(\eta)$$

$$= k\eta \exp(\eta^2)\frac{1}{\sqrt{\pi}} \int_{-\infty}^{\infty} P\frac{1}{\mu - \eta}K(\mu)F(\eta, \mu)A(\eta)d\mu.$$

Using the relations derived in [7], we obtain $g(\eta) \equiv [0, 0]$. Then,

$$Y(x, \mu) = B_0 + B_1(x - \mu)$$

$$+ \int_0^{\infty} \exp(-x/\eta)\Phi(\eta, \mu)B(\eta)d\eta$$

$$+ kK(\mu)\int_0^{\infty} \exp(-x/\eta)\eta P\frac{1}{\eta - \mu}F(\eta, \mu)A(\eta)d\eta.$$

The solution constructed for $B_0 = [2U_0, 0]^t$ and $B_1 = [0, 0]^t$ satisfies the boundary condition (4) at infinity. With an allowance for the boundary condition (4) on the wall, we arrive at a vector singular integral equation with a Cauchy-type kernel:

$$\begin{bmatrix} -2U|_S \\ 0 \end{bmatrix} = \frac{1}{\sqrt{\pi}}\int_0^{\infty}\frac{\eta B(\eta)d\eta}{\eta - \mu} + \exp(\mu^2)\lambda(\mu)B(\mu)$$

$$+ kK(\mu)\int_0^{\infty}\eta P\frac{1}{\eta - \mu}F(\eta, \mu)A(\eta)d\eta \quad (\mu > 0). \quad (8)$$

Using the relations derived in [7], we obtain

$$\int_0^{\infty}\eta P\frac{1}{\eta - \mu}F(\eta, \mu)A(\eta)d\eta$$

$$= \left[\mu\int_0^{\infty}F(\eta, \mu)A(\eta)d\eta\right]'_{\mu} = (2\mu - \varepsilon_T)\begin{bmatrix} -1 \\ 1/\gamma \end{bmatrix} + \varepsilon_n\begin{bmatrix} 1 \\ 0 \end{bmatrix},$$

where it was taken into account that [5]

$$\int_0^\infty F(\eta, \mu)A(\eta)d\eta = (\mu - \varepsilon_T)\begin{bmatrix} -1 \\ 1/\gamma \end{bmatrix} + \varepsilon_n\begin{bmatrix} 1 \\ 0 \end{bmatrix}.$$

Substituting the obtained integral into Eq. (8) and passing to the scalar representation, we arrive at the equation $(B(\eta) = [n(\eta), 0]^t)$

$$f(\mu) = \frac{1}{\sqrt{\pi}}\int_0^\infty \frac{\eta n(\eta)d\eta}{\eta - \mu} + \exp(\mu^2)\lambda(\mu)n(\mu) \quad (\mu > 0),$$
(9)

$$f(\mu) = [-2U|_S - (2\mu - \varepsilon_T)(\mu^2 - 1/2) - \varepsilon_n]k.$$

Introducing a supplementary function

$$N(z) = \frac{1}{2\pi i}\int_0^\infty \frac{\eta n(\eta)}{\eta - z}d\eta$$
(10)

and using the boundary values of $N^\pm(\mu)$ and $\lambda^\pm(\mu)$ on the upper and lower edges of the cut, we reduce Eq. (9) to the problem of determining an analytical function from the preset jump:

$$\frac{2f(\mu)\mu \exp(-\mu^2)}{X(-\mu)} = N^+(\mu)X^+(\mu) - N^-(\mu)X^-(\mu)$$
(11)

$$(\mu > 0),$$

where [6]

$$X(z) = \frac{1}{z}\exp\frac{1}{\pi}\int_0^\infty \frac{\zeta(\tau)}{\tau - z}d\tau,$$

$$\zeta(\tau) = -\pi/2 - \arctan\frac{\lambda(\tau)}{\sqrt{\pi}\tau \exp(-\tau^2)},$$

and $\theta(\tau) = \arg\lambda^+(\tau)$ is a regular branch of the argument of the function $\lambda^+(\tau)$ set by the condition $\theta(0) = 0$.

Taking into account the behavior of all functions entering into relation (11), the solution to this problem can be written as

$$N(z) = \frac{1}{X(z)}\frac{1}{\pi i}\int_0^\infty \frac{f(\mu)\mu \exp(-\mu^2)}{X(-\mu)}\frac{d\mu}{\mu - z}.$$
(12)

The function $N(z)$ determined by expression (10) vanishes at infinity. Let us require that the solution (12) would possess the same property. Expanding (12) into series in the vicinity of an infinitely remote point, we obtain

$$U|_S = \frac{k}{2}[(Q_1 - 2Q_3) + \varepsilon_T(Q_2 + 1/2) + \varepsilon_n].$$

Substituting the corresponding Loyalka integrals $Q_1 = -1.01619$, $Q_2 = -1.2663$, and $Q_3 = -1.8207$ [8] and the values of $\varepsilon_T = 1.3013$ and $\varepsilon_n = -0.5633$ [5], we eventually arrive at

$$U|_S = 0.5323k.$$

Passing to the dimensional variables, we obtain $\beta_R = 2.3524$. Taking into account that the rate of electrophoresis of high-thermal-conductivity particles in the region of small Knudsen numbers is given by the formula [4]

$$U_T = \tau v \text{Kn}\nabla\ln T, \quad \tau = -2K_T(C_T + \beta_R - \beta_B),$$

where $K_T = 1.14995$, $C_T = 2.204939$, and $\beta_B = 5.798445$, we finally determine $\tau = 2.85442$. Here, C_T is the coefficient of the temperature jump at the plane solid surface and β_B is the Barnett slip coefficient. Note that the second-order thermal slip coefficient β_R determined in this study theoretically confirms the possibility of negative (proceeding in the direction of the temperature gradient) thermophoresis (for comparison, $\tau = 3.258$ [2]).

REFERENCES

1. S. L. Gorelov, Izv. Akad. Nauk SSSR, Mekh. Zhidk. Gaza, No. 5, 178 (1976).
2. Takeo Soga, Phys. Fluids **29** (4), 976 (1986).
3. H. A. Dwyer, Phys. Fluids **10** (5), 976 (1967).
4. E. G. Mayasov, A. A. Yushkanov, and Yu. I. Yalamov, Pis'ma Zh. Tekh. Fiz. **14** (6), 498 (1988) [Sov. Tech. Phys. Lett. **14**, 220 (1988)].
5. A. V. Latyshev, Prikl. Mat. Mekh. **54** (4), 581 (1990).
6. C. Cercignani, *Mathematical Methods in Kinetic Theory* (Plenum, New York, 1969; Mir, Moscow, 1973).
7. M. N. Gaĭdukov and V. N. Popov, Izv. Akad. Nauk, Mekh. Zhidk. Gaza, No. 2, 165 (1998).
8. S. K. Loyalka, Transp. Theory Stat. Phys. **4**, 55 (1975).

Translated by P. Pozdeev

Crystal Chemistry and Martensite Phase Diagrams of Titanium–Nickel Based Ternary Alloys

A. A. Klopotov, V. É. Gyunter, T. L. Chekalkin, and É. V. Kozlov

Institute of Medical Materials and Shape-Memory Implants, Siberian Physicotechnical Institute,
Tomsk State University, Tomsk, Russia
e-mail: guntsme@elefot.tsu.ru
Received April 11, 2002

Abstract—The laws of variation of the phase diagrams describing martensite transformations in ternary alloys based on the TiNi system are established by analysis of the crystallochemical parameters. © *2002 MAIK "Nauka/Interperiodica".*

One of the main problems encountered in the practical use of titanium–nickel (TiNi) based alloys is the need in correctly predicting variations of their properties. In particular, it is very important to know the initial temperature intervals of manifestation of the shape memory and superelasticity effects [1]. One possible way of solving this problem is via establishing the laws of the influence of doping on the sequence and positions of the temperature intervals of martensite transformations (MTs) in TiNi based alloys.

Below we present the results of investigation of the MTs and measurement of the crystallochemical parameters of ternary alloys based on the TiNi system. Based on these data, we will consider the general laws governing the influence of a third (doping) element on the phase diagrams of a binary TiNi alloy.

An analysis of the positions of doping elements in the Periodic Table and the features of MTs in the doped TiNi alloys reveals the following regularities [1, 2].

For a doping element Me situated on the Periodic Table to the left from nickel, where $e/a = s + d < 10$ and $R_{Me} \sim R_{Ni}$ or $R_{Me} > R_{Ni}$ (e/a being the number of valence-shell electrons per atom and R_{Ni} and R_{Me}, the atomic radii of nickel and dopant, respectively), the phase diagram contains a narrow region of dopant concentration (from 0 to ~10 at. %) featuring martensite transformations $B2 \longrightarrow R \longrightarrow B19'$ (Fig. 1). As the dopant concentration increases, the region of MTs shifts toward lower temperatures.

When the dopant is situated to the right from nickel or occurs in the same column (see the cross-hatched fragment of the Periodic Table in Fig. 1, where $e/a = s + d = 10$ or $s + d > 10$ and $R_{Me} > R_{Ni}$ or $R_{Me} \sim R_{Ni}$), the MTs may take place in various sequences ($B2 \longrightarrow R \longrightarrow B19'$, $B2 \longrightarrow B19'$, $B2 \longrightarrow B19$, $B2 \longrightarrow B19''$) in a broad range of dopant concentrations, up to the complete substitution of nickel.

In both cases, the regions of existence of the R(ω) phase depend on the electronic and dimensional factors of the TiNi–TiMe ternary alloy under consideration. Figure 2 shows the regions of existence of the R(ω) phase in TiNi–TiMe alloys characterized by various dimensional factors $\delta_R = C_{Ti}R_{Ti}/(C_{Ni}R_{Ni} + C_{Me}R_{Me})$, where C_{Ti}, C_{Ni}, and C_{Me} are the concentrations of components (titanium, nickel, and dopant, respectively) in the alloy. As can be seen, the initial binary alloy (TiNi) possesses the most extended region of existence of the R(ω) phase on the δ_R scale. The R(ω) phase region is less extended in the alloys doped with Rh, Co, Pd, Pt, and Au, and it is very narrow in the TiNi(Fe) system. Since the atomic radius of iron is close to that of nickel, the existence of the R(ω) phase in TiNi–TiFe alloys is probably determined by the electronic factor. In ternary alloys of the TiNi–TiPd, TiNi–TiPt, and TiNi–TiAu systems (where nickel atoms are replaced by atoms of the third element possessing a greater atomic radius), the R(ω) phase exists within a limited region of concentrations and temperatures [1]. In alloys of the TiNi–TiRh system, Rh atoms replacing Ni also possess greater dimensions, as reflected by the width of the interval of existence of the R(ω) phase on the δ_R scale (Fig. 2).

An analysis of the phase diagrams of the TiNi–TiFe, TiNi–TiCo, and TiNi–TiRh ternary systems (Fig. 1) shows the presence of $B2 \longrightarrow R(\omega) \longrightarrow B19'$ transitions in the entire concentration range of martensite transformations. Despite close atomic radii of nickel and copper, the TiNi–TiCu system exhibits no R(ω) phase formation (Fig. 1). However, the R(ω) phase was observed when the doping was produced according to the $Ti_{50-x}Ni_{50-x}Cu_{2x}$ scheme [2]. Thus, an analysis of the effect of the dimensional factor of the region of existence of the R(ω) phase in TiNi(Me) ternary alloys does not reveal simple relationships.

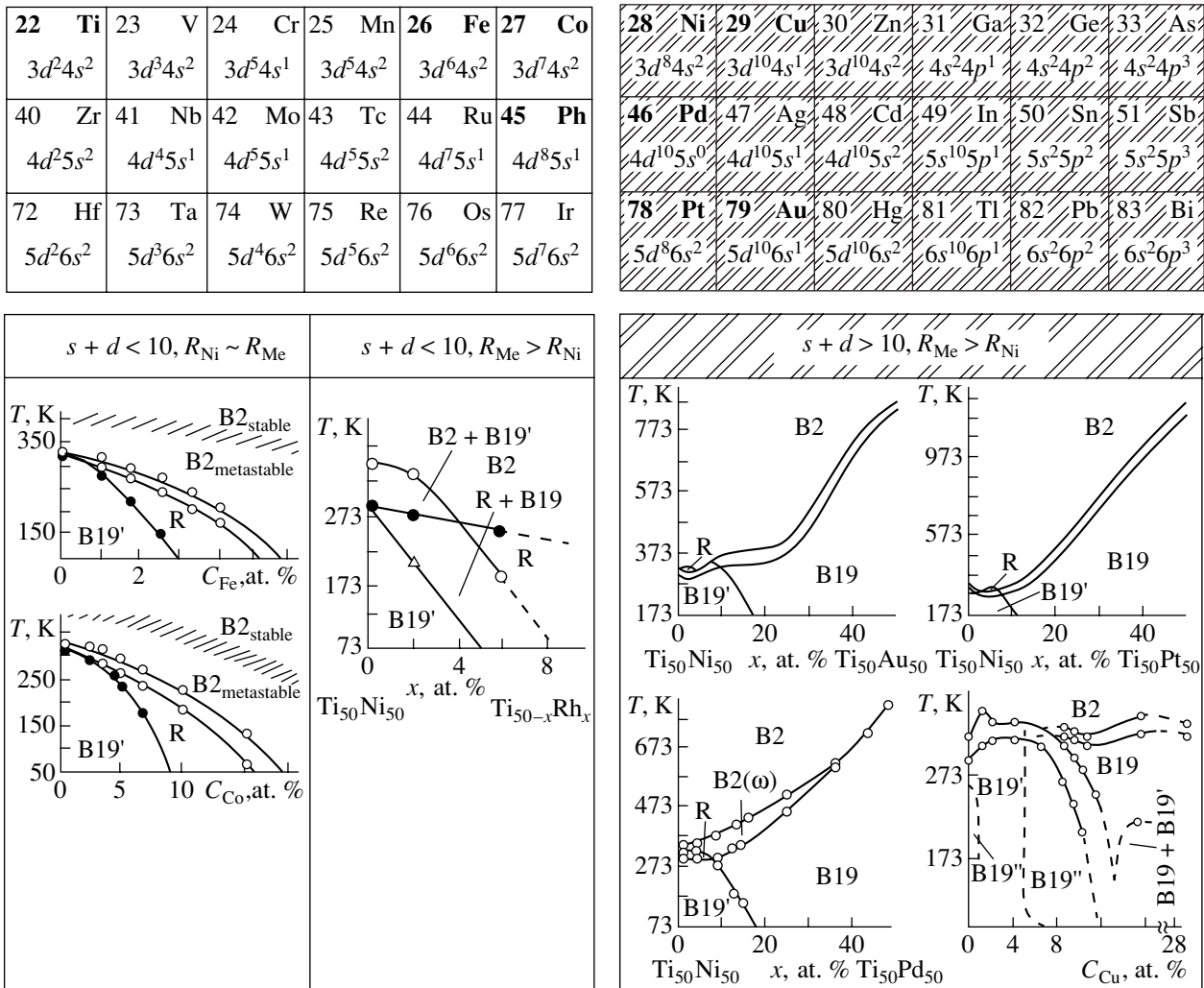Figure 3 shows the regions of existence of the R(ω) phase depending on the electron density e/a (the num-

22 Ti	23 V	24 Cr	25 Mn	26 Fe	27 Co
$3d^24s^2$	$3d^34s^2$	$3d^54s^1$	$3d^54s^2$	$3d^64s^2$	$3d^74s^2$
40 Zr	41 Nb	42 Mo	43 Tc	44 Ru	45 Ph
$4d^25s^2$	$4d^45s^1$	$4d^55s^1$	$4d^55s^2$	$4d^75s^1$	$4d^85s^1$
72 Hf	73 Ta	74 W	75 Re	76 Os	77 Ir
$5d^26s^2$	$5d^36s^2$	$5d^46s^2$	$5d^56s^2$	$5d^66s^2$	$5d^76s^2$

28 Ni	29 Cu	30 Zn	31 Ga	32 Ge	33 As
$3d^84s^2$	$3d^{10}4s^1$	$3d^{10}4s^2$	$4s^24p^1$	$4s^24p^2$	$4s^24p^3$
46 Pd	47 Ag	48 Cd	49 In	50 Sn	51 Sb
$4d^{10}5s^0$	$4d^{10}5s^1$	$4d^{10}5s^2$	$5s^15p^1$	$5s^25p^2$	$5s^25p^3$
78 Pt	79 Au	80 Hg	81 Tl	82 Pb	83 Bi
$5d^86s^2$	$5d^{10}6s^1$	$5d^{10}6s^2$	$6s^16p^1$	$6s^26p^2$	$6s^26p^3$

Fig. 1. A fragment of the Periodic Table and phase diagrams of martensite transformations in TiNi–TiMe systems.

ber of $s + d$ electrons per atom) in TiNi–TiMe alloys. As is seen, the R(ω) phase exists in a broader interval range of the e/a values in the binary TiNi system than in most ternary systems. In TiNi alloys, this phase exists in the region of $e/a > 7$, which coincides with the interval of existence of the R(ω) in TiNi–TiAu system. In contrast,
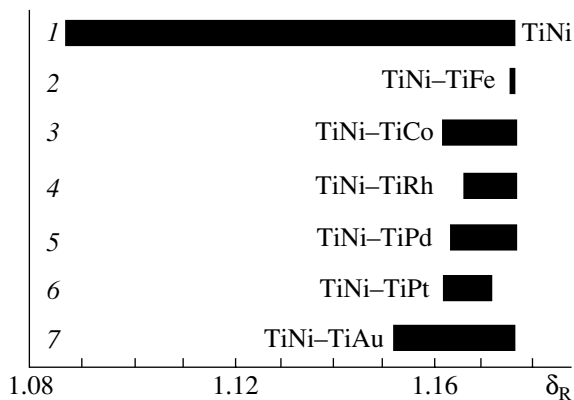
Fig. 2. Dependence of the region of existence of the R(ω) phase in TiNi and TiNi–TiMe alloys on the dimensional factor δ_R.
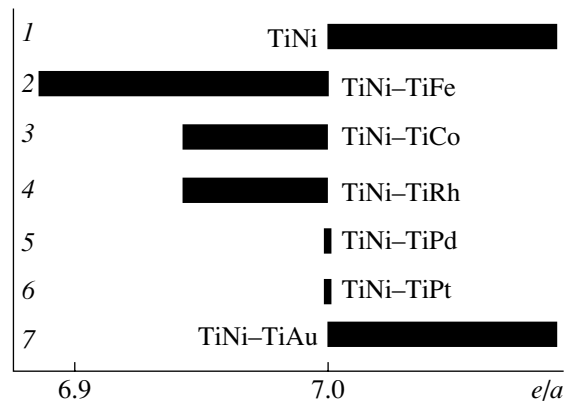

Fig. 3. Dependence of the region of existence of the R(ω) phase in TiNi and TiNi–TiMe alloys on the electron density factor e/a.

The influence of electron and dimensional factors on martensite transformations in TiNi–TiMe ternary alloys

Wide concentration–temperature region of R phase	Narrow concentration–temperature region of R phase	No R phase
$e/a = s + d \sim 6.9\text{–}7.0$ $R_{Ni} \sim R_{Me}$ or $R_{Ni} < R_{Me} < R_{Ti}$	$e/a = s + d \sim 7.0\text{–}7.07$ $R_{Ni} < R_{Me} < R_{Ti}$	$s + d > 7.0$ $R_{Ni} \sim R_{Me}$

the electron density factor of the R(ω) phase in ternary alloys of the TiNi–TiFe, TiNi–TiCo, and TiNi–TiRh systems is $e/a < 7$.

An analysis of the role of dimensional (δ_R) and electronic (e/a) factors on the region of existence of the R(ω) phase led us to the following conclusions. In TiNi–TiPd and TiNi–TiPt alloys, the main effect on the R(ω) phase formation is produced by the dimensional factor; in TiNi–TiFe and TiNi–TiCo systems, the major contribution is due to the electronic factor; while in TiNi–TiRh and TiNi–TiAu alloys, the electronic and dimensional factors are jointly operative.

Based on the above data, it is possible to reveal the main features of influence of the third (doping) element upon the B2 $\longrightarrow$ R(ω) phase transition in TiNi based alloys. In the case when atoms of greater radius substituted for nickel create an electron density e/a in the interval from 7.0 to 7.07, the phase diagram of the ternary alloy features narrow concentration and temperature intervals of the R(ω) phase. This situation is observed in TiNi–TiPd, TiNi– TiPt, and TiNi–TiAu alloys. In TiNi–TiMe alloys (Me = Fe, Co, Rh), where the atomic radius of the dopant is equal to that of nickel or $R_{Ni} < R_{Me} < R_{Ti}$ and the electron density falls within $e/a = 6.9\text{–}7.0$, the region of existence of the R(ω) phase is more extended in both concentration and temperature scales. In TiNi–TiCu alloys, the B2 $\longrightarrow$ R(ω) phase transition is suppressed. Although the atomic radii of copper and nickel are close, the electron configuration of the ternary alloys are such that e/a exceeds 7.0. The results of this analysis are summarized in the table.

Conclusion. We have analyzed the data concerning the role of crystallochemical factors on the stability of B2, R, and B19' phases in TiNi-based alloys doped with iron, cobalt, copper, palladium, platinum, gold, and rhodium. Relationships are established between the dimensional and electronic factors, on the one hand, and the sequence of martensite transformations, on the other hand. The shape of phase diagrams in the region of martensite transformations depends on the position of dopants in the Periodic Table relative to Group VIII (i.e., whether the element occurs to the right or to the left from nickel). The role of electron density and dimensional factor was revealed by calculations of the superstructural compression. A unique correspondence is established between the dimensional and electron factors, on the one hand, and the concentration and temperature intervals of existence of the R(ω) phase, on the other hand.

REFERENCES

1. V. É. Gyunter, G. Ts. Dambaev, P. G. Sysolyatin, *et al.*, *Medical Materials and Implants with Shape Memory* (Tomskiĭ Gos. Univ., Tomsk, 1998).

2. D. B. Chernov, L. A. Monasevich, N. N. Bashanova, and Yu. I. Paskal', Fiz. Met. Metalloved. **59** (6), 1226 (1985).

Translated by P. Pozdeev

High-Power Subnanosecond 38-GHz Microwave Pulses Generated at a Repetition Rate of up to 3.5 kHz

D. M. Grishin, V. P. Gubanov, S. D. Korovin, S. K. Lyubutin,
G. A. Mesyats, A. V. Nikiforov, V. V. Rostov, S. N. Rukin,
B. G. Slovikovskiĭ, M. R. Ul'maskulov, K. A. Sharypov, V. G. Shpak,
S. A. Shunaĭlov, and M. I. Yalandin

Institute of Electrophysics, Ural Division, Russian Academy of Sciences, Yekaterinburg, Russia
e-mail: yalandin@iep.uran.ru
Institute of High-Current Electronics, Siberian Division, Russian Academy of Sciences, Tomsk, Russia
e-mail: rostov@lfe.hcei.tsc.ru
Received April 15, 2002

Abstract—An original relativistic backward tube (BWT) for a 38 GHz range is developed and tested. The BWT is capable of generating stable pulses of ~250 ps duration and a peak power of ~250 MW in trains with a length of up to 1 s at a repetition rate of 1–3.5 kHz. The BWT design implements an inhomogeneous slow-wave structure of increased cross section with a band reflector. A pulsed electron beam (~270 keV, ~ 2 kA, 0.9 ns) was injected by a high-current accelerator based on a high-voltage generator with an inductive energy store, a semiconductor current interrupter, and a pulse-shaping hydrogen-filled discharge gap. A focusing magnetic field of 2 T was generated by a cooled pulsed solenoid power-supplied from a special stabilized current source. © 2002 MAIK "Nauka/Interperiodica".

The results of our previous experiment [1] and earlier investigations (see, e.g., [2, 3]) showed that relativistic backward tubes (BWTs) operating in a significantly nonstationary (superradiance) regime can generate short microwave pulses with a duration on the order of ten periods of the high-frequency field and a power close to that of the injected electron beam. A certain progress in realizing this possibility was provided by the use of a slow-wave structure (SWS) with increased cross section size ($R \sim 0.7 \lambda$), profiled coupling impedance, and resonance reflector instead of a below-cutoff waveguide section [4]. In the first experiments [1], performed with a high-current electron accelerator of the RADAN type capable of producing a pulsed electron beam with a pulse duration of ~1 ns and a power of ~600 MW, we obtained microwave pulses with a duration of ~250 ps and a peak power of up to 280 MW for a magnetic induction of $B \sim 2$ T, and up to 400 MW for $B > 5$ T. Because of a high energy consumption of the pulsed solenoid (at a pulse duration of a few milliseconds), the system was operated in a regime of rare pulses repeated at a pause reaching several tens of seconds. However, reduction of the working magnetic field down to a level of 2 T allowed technical realization of a pulsed-periodic regime of the microwave generator equipped with a cooled dc solenoid. On the other hand, there was gained a certain progress in the generation of high-voltage accelerating pulses, based on a hybrid modulator ensuring a pulse repetition rate of up to 3.5 kHz in a train regime [5].

Below we report the results of investigation of a subnanosecond relativistic BWT for a 38 GHz range, operating in the train regime at a high-frequency repetition rate. The experimental setup comprised the following main parts: (i) hybrid high-voltage modulator; (ii) vacuum diode of the electron accelerator; (iii) BWT electrodynamic system and emitting antenna; (iv) vacuum system; (v) dc solenoid with an induction of 2 T and a power supply pulse duration of 1 s; (vi) stabilized current generator for the solenoid power supply; (vii) liquid cooling system of the solenoid; (viii) diagnostic and monitoring electronic equipment; and (ix) control and synchronization system.

The hybrid high-voltage modulator comprised a nanosecond driver (SM-3NS) [6] and a subnanosecond hydrogen-filled (100 atm) shaping discharge gap. The SM-3NS driver included several steps of energy compression switched by solid-state commutators. The driver output was loaded on the inductive energy store with a high-current high-voltage semiconductor current interrupter. Judging by the oscillogram of a voltage pulse on a 45-Ω output of the hybrid modulator (Fig. 1), the full amplitude scatter of the accelerating pulses did not exceed 3–5% at a repetition frequency of up to 3.5 kHz. The high-voltage pulses (Fig. 1) were transmitted to the accelerator cathode via a stepped-profile coaxial line at a total transformation coefficient of 1.6, so that a voltage amplitude on the cathode reached ~260–270 kV. The tubular graphite cathode with a diameter of 8.6 mm and an edge thickness of 0.1 mm
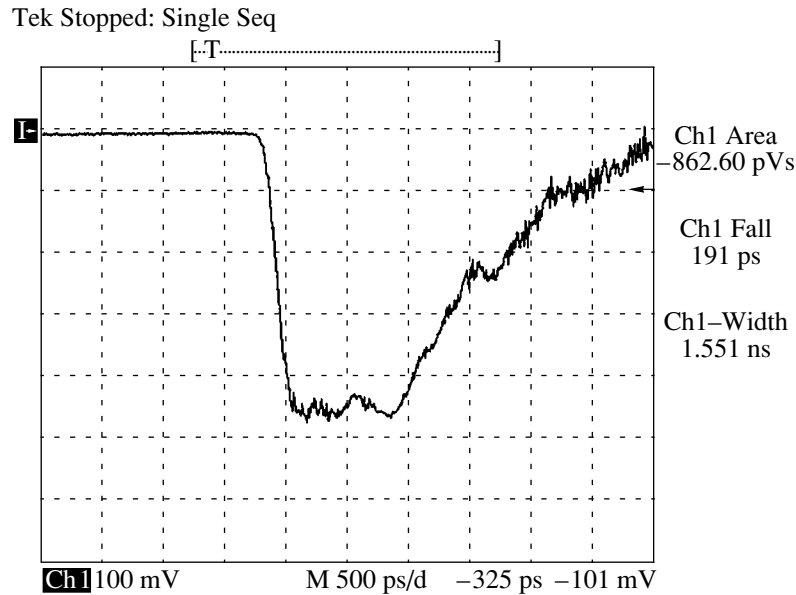
Tek Stopped: Single Seq

Ch1 Area
−862.60 pVs

Ch1 Fall
191 ps

Ch1–Width
1.551 ns

Ch1 100 mV   M 500 ps/d   −325 ps   −101 mV

Fig. 1. A typical voltage pulse (amplitude, ~165 kV; top plateau duration, ~0.9 ns) from a capacitive divider, measured by a digital storage oscillograph on a 45-Ω output of the hybrid modulator at a repetition rate of 1 kHz.

was mounted inside the anode cylinder with a diameter of 19 mm. A solenoid coil with a resistance of 0.7 Ω had the form of sections wound by a 1×5 mm copper ribbon. Each turn of the coil was cooled by transformer oil pumped via radial channels between the sections. A magnetic field induction of 2 T corresponded to a current of 265 A. A bank of molecular capacitors with a total capacity of 4.6 F was switched to solenoid in an incomplete discharge regime by a feedback transistor switch with pulse-width modulation, ensuring a 2% current stabilization for a time period of 1 s. The power dissipated in the solenoid coil was removed by the oil pumped during the pause between pulses (~100 s) required for charging the bank.

The SWS, made of copper by methods of galvano-plastics, accommodated 18 corrugation periods with an average diameter of 11.2 mm (the same as in [1]). The generator operated in a E_{01} working mode. The horn antenna had a vacuum output window with a diameter of 50 mm. The BWT vacuum chamber was evacuated to 10^{-3}–10^{-4} Torr with a turbomolecular pump. The pumping was effected simultaneously from the accelerator vacuum diode side and via a slit at the vacuum output window.

The results of a full-scale numerical modeling of the system operation using the particle-in-cell method (KARAT code [7]) showed that a subnanosecond pulse energy may reach up to 100 mJ (Fig. 2). Operation in the pulse train regime facilitated calorimetric measurements. A specially designed calorimeter with an ethanol microwave absorber and a capillary detector was calibrated so as to measure the total energy of the train containing 500–1000 pulses with a total duration of ≤1 s. The calibration was performed over a 10–100 J

range in two regimes. The first procedure employed the discharge of a capacitor with a time constant of 20 ms via a thin nichrome wire situated inside the absorber cavity. In the second case, the signal was detected from a dc current source relay-switched for 0.5–1.5 s. Calibrations in the two regimes showed coincidence of the results to within 3% and demonstrated linearity of the capillary detector response as a function of the deposited energy.

An output signal from the hot-carrier germanium microwave detector was fed to a Tektronix TDS-820 digital storage oscillograph with a frequency bandwidth of 6 GHz. Each oscillogram was obtained by accumulating not less than 512 pulses (counted at a discretization step of 10 ps). It is important to note that the system involved no additional delay cable line significantly distorting the shape of subnanosecond signals. The length of a calibrated cable between detector and oscillograph was 1.5 m. The detector was calibrated in a 0.1–50 kW range with the aid of a magnetron generator and a thermistor bridge (M3-22A). Because of a high pulse repetition rate, the pulsed bias voltage was set at a minimum amplitude and duration in order to minimize the crystal heating and the temperature drift of the sensitivity within a single measurement cycle. An insignificant drift still took place: the sensitivity at the pulse train end dropped approximately by 2% for $F \leq 1$ kHz and by 7% for $F = 3.5$ kHz. In order to take into account nonlinearity of the detector voltage–power characteristic, the experimental oscillograms were computer processed to calculate the effective duration of the microwave pulses.

In the course of the measurements, the radiation was polarized according to the TM01 mode. The detector

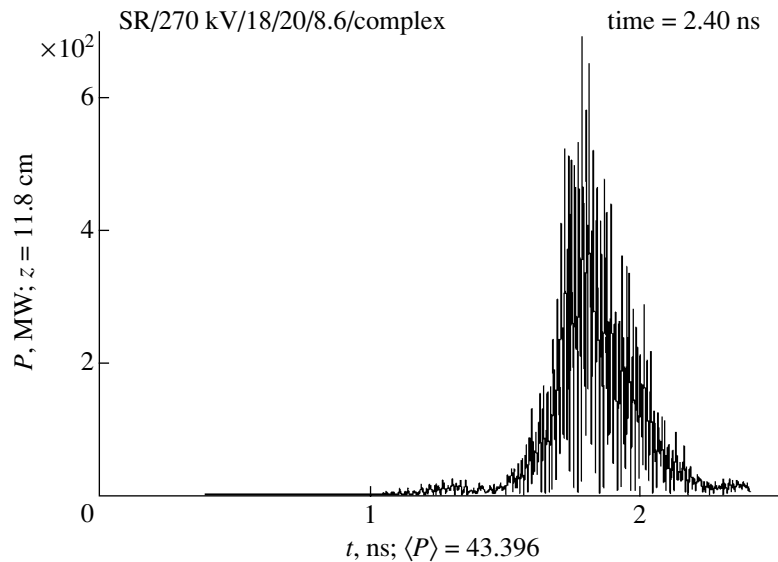SR/270 kV/18/20/8.6/complex   time = 2.40 ns

Fig. 2. Numerically modeled nonaveraged output power of a relativistic 38-GHz BWT with a transport magnetic field of 2 T, generating subnanosecond pulses with a front duration of 200 ps, FWHM ~ 250 ps, and an energy of 104 mJ/pulse.

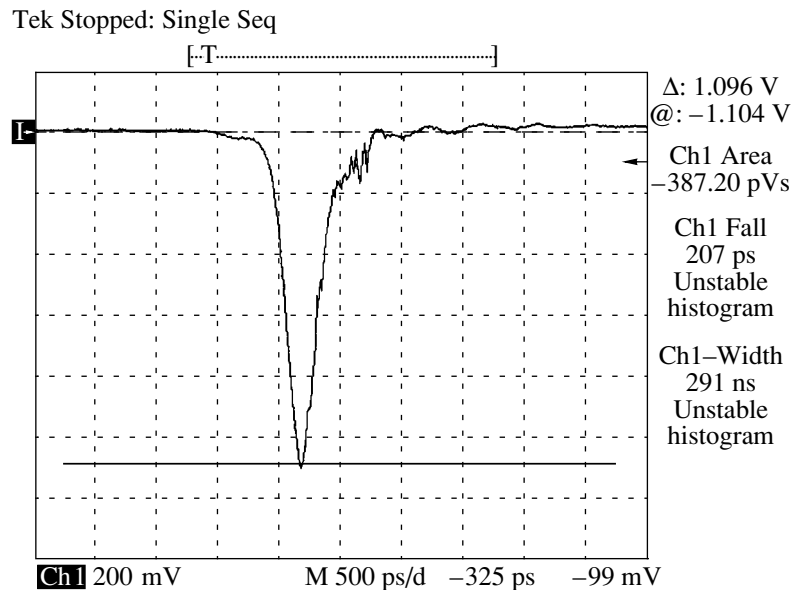Tek Stopped: Single Seq

Δ: 1.096 V
@: −1.104 V

Ch1 Area
−387.20 pVs

Ch1 Fall
207 ps
Unstable
histogram

Ch1–Width
291 ns
Unstable
histogram

Ch1 200 mV   M 500 ps/d   −325 ps   −99 mV

Fig. 3. A typical signal from the microwave detector accumulated by a digital storage oscillograph for 512 pulses (pulse front duration 207 ps; FWHM ~ 291 ps).

was placed at a point with the coordinates $L = 4$ m, $R = 0.9$ m (L is the cross-section distance from the vacuum output window and R is the radius). According to the results of preliminary measurements, the effective cross section of the horn antenna was independent to within 2% of the microwave frequency in a 15% band. The detector signal distortions related to the reflection from a load were eliminated using a time decoupling provided by a long waveguide between the germanium crystal and the absorbing load.

Figure 3 shows a typical oscillogram of the output signal from the microwave detector accumulated by the oscillograph during 512 sequential counts at a repeti-

tion frequency of 1 kHz. The results of processing showed that the actual leading front duration and the microwave pulse width at half maximum (FWHM) are 190 and 250 ps, respectively. The calorimetric measurements performed under the same conditions gave 65 mJ for the energy per pulse, which corresponds to a total microwave energy of 260 MW. The average microwave pulse power in the train was about 200 W at a repetition rate of 3.5 kHz. The output peak power was close to the value obtained in a single pulse regime [1].

It should be noted that there is some tendency to understate the measured peak power. Indeed, there are obvious limitations in the frequency characteristic of

the "detector–transmitting tract–oscillograph" system. The results of numerical calculations of the microwave generator showed that the length of the peak part of the pulse with a power exceeding 250 MW must be equal to only a few periods of the high-frequency oscillations, i.e., to about 50–70 ps (Fig. 2). However, a transient time characteristic of the TDS-820 oscillograph is 67 ps. A similar role was played by a spurious capacitance of the detector crystal relative to the waveguide case, since the reflection measurements showed evidence of a test signal front being extended from 100 to 150 ps. On the other hand, the accuracy of calibration of the beam current and acceleration voltage meters was about 10%, so that the electron beam parameters could also somewhat differ from expected. Nevertheless, there is quite a good coincidence between the experimental data and the results of numerical calculations.

In one series of pulses, we intentionally increased the accelerating voltage by 4–5% (to a limiting possible value provided by the modulator). As a result, the output radiation energy increased up to 80 m/J per pulse, so that the maximum peak power of the generated microwave pulses exceeded 300 MW.

Our experimental results showed evidence of a decrease in the power and duration of microwave pulses, as well in the stability of these characteristics, after generation of 10^4 pulses and above. In the following, we plan to verify a hypothesis concerning an increase in the delay time for the beam generated by a cathode operating in an explosive (blowup) regime. Such a behavior was previously observed in a nanosecond range of the voltage pulse durations, where the effect was also related to deterioration and subsequent stabilization of the cathode emissivity [8]. Should it be the only significant defect influencing the working life of the proposed microwave generator, the problem could be solved, for example, by increasing duration of the accelerating voltage pulse.

Thus, the entire series of experiments (beginning with a single pulse regime [1]) confirmed expectations (based on the model calculations) that the coefficient of conversion in a superradiance peak of a relativistic BWT can be increased by using an inhomogeneous slow-wave structure with increased bandwidth and, accordingly, reduced effect of the wave packet smearing. The possibility of generating high-power subnanosecond microwave pulses at a high repetition rate has been demonstrated.

REFERENCES

1. S. D. Korovin, G. A. Mesyats, V. V. Rostov, *et al.*, Pis'ma Zh. Tekh. Fiz. **28** (2), 81 (2002) [Tech. Phys. Lett. **28**, 76 (2002)].

2. N. S. Ginzburg, S. P. Kuznetsov, and T. N. Fedoseeva, Izv. Vyssh. Uchebn. Zaved., Radiofiz. **21** (7), 1037 (1978).

3. M. I. Yalandin, V. G. Shpak, S. A. Shunaĭlov, *et al.*, IEEE Trans. Plasma Sci. **28** (5), 1615 (2000).

4. I. K. Kurkan, V. V. Rostov, and E. M. Tot'meninov, Pis'ma Zh. Tekh. Fiz. **24** (10), 43 (1998) [Tech. Phys. Lett. **24**, 388 (1998)].

5. S. K. Lyubutin, G. A. Mesyats, S. N. Rukin, *et al.*, Prib. Tekh. Éksp., No. 5, 80 (2001).

6. S. K. Lyubutin, S. N. Rukin, B. G. Slovikovskiĭ, *et al.*, Prib. Tekh. Éksp., No. 3, 52 (2000).

7. V. P. Tarakanov, *User's Manual for Code KARAT* (Berkeley Research Associates, 1992).

8. A. V. Gunin, V. F. Landl, S. D. Korovin, *et al.*, IEEE Trans. Plasma Sci. **28** (3), 537 (2000).

Translated by P. Pozdeev

Selective and Wideband UV Sensors

**V. N. Komashchenko, K. V. Kolezhuk, E. F. Venger, G. I. Sheremetova,
O. A. Mishchuk, and A. V. Komashchenko**

Institute of Semiconductor Physics, National Academy of Sciences of Ukraine, Kiev, Ukraine
Research Institute of Petrochemical Industry, Kiev, Ukraine
e-mail: komag@isp.kiev.ua
Received May 15, 2002

Abstract—It is shown that thin-film photoelectric devices can be constructed on the basis of wide-gap $A^{II}B^{VI}$ semiconductor compounds grown on a narrow-gap quasi-single-crystal substrate. The potential barrier ΔE_v existing at the interface of a multilayer heterostructure blocks the contribution of the narrow-gap component to the total photocurrent. Based on these heterostructures, selective and wideband UV sensors requiring no additional filters are developed for the first time. © *2002 MAIK "Nauka/Interperiodica"*.

A currently important problem of UV technology is developing sensors for the 320–400 nm (UV-A), 280–320 nm (UV-B), and 200–280 nm (UV-C) wavelength intervals [1–3]. Such sensors are required for numerous applications in medicine, biology, environmental control (ecology, ozone monitoring, fire-extinguishing systems, etc.), and other fields. Among the existing methods of manufacturing selective radiation sensors, the most common approach is based on the use of colored glass or interference filters.

Previously [4], we demonstrated that some heterostructural concepts realized in lattice-matched $A^{III}B^{V}$ single crystal systems [5] can be applied to polycrystalline heterostructures of $A^{II}B^{VI}$ semiconductor compounds, among which there are no materials with close crystal lattice parameters.

In this study, some special features of the $A^{II}B^{VI}$ heterostructures are used for creating photoelectric devices of new types, some of which were not available until now. In particular, we propose the design of UV-(A + B + C) wideband and UV-A and UV-B selective sensors capable of operating without additional optical filters.

The samples for this study were prepared by methods described elsewhere [4, 6, 7]. Wide-gap photosensitive components in the heterostructures studied were represented by homogeneous n-ZnS$_{0.7}$Se$_{0.3}$ or n-Zn$_{0.8}$Cd$_{0.2}$S solid solutions with a gap width of $E_g = 3.3$ eV, which corresponds to the long-wavelength boundary of the UV-A interval. The thicknesses d of these nearly stoichiometric high-resistivity films were comparable with the effective absorption length of the exciting radiation ($d \sim 1/k \sim 1$ μm, where k is the absorption coefficient). In order to provide for the lattice matching and ensure the epitaxial growth conditions, thin (several tens of nanometers thick) intermediate layers of multicomponent solid solutions were grown between an orienting low-resistivity narrow-gap substrate (CdSe, $E_g = 1.7$ eV) and the photosensitive component of the heterostructure. The presence of these intermediate layers was confirmed by depth–composition profiles of the samples determined with the aid of the Auger electron spectroscopy [6]. For example, the n-ZnS/n-CdSe heterostructure contained a variband interlayer of the Zn$_x$Cd$_{1-x}$S$_y$Se$_{1-y}$ type with x and y values decreasing with increasing distance from the surface. On approaching the surface of the orienting substrate, the intermediate layer composition corresponded to $x = y = 0$.

Since the exciting radiation is incident onto a wide-gap $A^{II}B^{VI}$ semiconductor surface, heterostructures of this type must, in the general case, exhibit the effect of a wide-gap window. However, an additional potential barrier ΔE_v, existing at the interface of a multilayer heterostructure due to a difference of the electron affinities and gap widths of the contacting materials, can suppress the contribution of the narrow-gap component to the total photocurrent.

An energy band diagram of the resulting p-Cu$_{1.8}$S/i-ZnS$_{0.7}$Se$_{0.3}$/n-CdSe multilayer heterostructure (see the inset in Fig. 1) reveals a high-resistivity i-layer bounded by a low-resistivity substrate possessing a narrower gap value. The main fraction of charge carriers is generated by the incident light beam immediately at the potential barrier, where a strong electric field is operative. The contribution of the narrow-gap component to the total photocurrent is blocked by the barrier which amounts to $\Delta E_v \sim 0.7$ eV.

Figure 1 shows typical spectral characteristics of photosensitivity of the UV-(A + B + C) wideband (curve *1*) and UV-A selective (curve *2*) sensors based on a p-Cu$_{1.8}$S/i-ZnS$_{0.7}$Se$_{0.3}$/n-CdSe heterostructure and the UV-B selective (curve *3*) sensors based on a p-Cu$_{1.8}$S/i-ZnS/n-CdSe heterostructure. As can be seen,
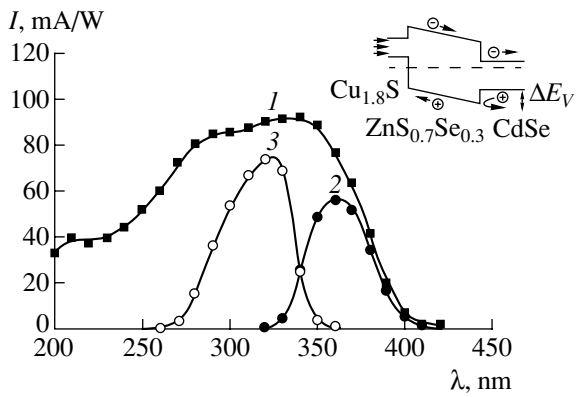
Fig. 1. Absolute spectral sensitivity of the heterostructures: (*1*) UV-(A + B + C); (*2*) UV-A; (*3*) UV-B. The measurements were performed at $T = 300$ K on samples with an effective working surface area of 4.5 mm^2. The inset shows an energy band diagram of a p-Cu$_{1.8}$S/i-ZnS$_{0.7}$Se$_{0.3}$/n-CdSe heterostructure (intermediate lattice-matching interlayers not depicted).
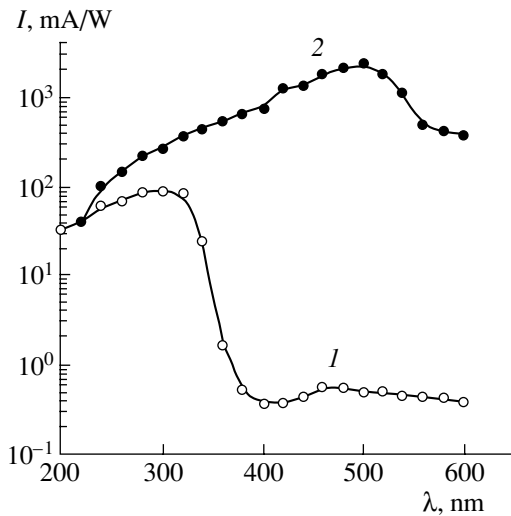
Fig. 2. The spectral sensitivity of a p-Cu$_{1.8}$S/n-ZnS/p-ZnTe/n-CdS heterostructure: (*1*) unbiased; (*2*) with an applied voltage of $U_b = 5$ V (minus on p-Cu$_{1.8}$S).

the additional potential barrier height is sufficient to provide for a significant (about two orders of magnitude) decrease in photosensitivity beyond the fundamental absorption edge of the wide-gap component. It should be emphasized that the proposed sensors are manufactured without using interference or colored glass filters.

A very interesting phenomenon was observed for a more complicated heterostructure of the p-Cu$_{1.8}$S/n-ZnS/p-ZnTe/n-CdS type, in which application of an external bias voltage led to an increase in the photocurrent and to a modification of the spectral sensitivity spectrum. In a photorectifier cell regime, the interval of photosensitivity of this heterostructure was the same as that of a UV sensor "blind" in the visible range (Fig. 2, curve *1*). The spectral characteristic exhibited a dramatic change upon application of the external bias voltage U_b (Fig. 2, curve *2*): the maximum of sensitivity was significantly shifted toward longer wavelengths. The data presented in Fig. 2 were measured at an incident monochromatic radiation power of ~10^{-7} W/cm^2 and $U_b = 5$ V (with minus on the p-Cu$_{1.8}$S side). This result is evidence of a significant contribution of the narrow-gap (ZnTe) component to the total photocurrent. It should be also noted that the multilayer anisotype heterostructure exhibits the effect of photocurrent amplification (cf. curves *1* and *2* in Fig. 2). The observed features can be explained assuming that the heterostructure studied represents a bipolar phototransistor. Elucidating the nature of these phenomena requires additional investigations.

Thus, application of the epitaxial growth technology and use of the potential barriers formed at the interfaces between semiconductors with different gap widths opens new possibilities for the creation of photoelectric devices in heterostructures involving lattice-unmatched A^{II}B^{VI} semiconductor compounds. Based on such systems, UV-A and UV-B selective and UV-(A + B + C) wideband sensors requiring no additional filters have been developed for the first time. A multilayer anisotype A^{II}B^{VI} heterostructure exhibits a field-induced modification of the photosensitivity spectrum and the effect of photocurrent amplification.

REFERENCES

1. A. Ohtomo, M. Kawasaki, T. Koida, *et al.,* Appl. Phys. Lett. **72** (19), 2466 (1998).
2. W. Yang, R. D. Vispute, S. Choopun, *et al.*, Appl. Phys. Lett. **78** (18), 2787 (1998).
3. K. Ando, H. Ishikura, Y. Fukunaga, *et al.*, Phys. Status Solidi B **229** (2), 1065 (2002).
4. A. V. Komashchenko, K. V. Kolezhuk, P. P. Gorbik, *et al.*, Pis'ma Zh. Tekh. Fiz. **26** (5), 1 (2000).
5. Zh. I. Alferov, Fiz. Tekh. Poluprovodn. (St. Petersburg) **32**, 3 (1998) [Semiconductors **32**, 1 (1998)].
6. E. F. Venger, K. V. Kolezhuk, V. N. Komashchenko, *et al.*, Dopov. Nats. Akad. Nauk Ukr., No. 2, 82 (2002).
7. K. V. Kolezhuk, V. N. Komashchenko, G. I. Sheremetova, *et al.*, Optoélektron. Poluprovodn. Tekh. **36**, 212 (2001).

Translated by P. Pozdeev

X-ray Radiation Increases the Magnetic Sensitivity of Planar-Diffusion Triacs

S. I. Vorontsov, S. B. Baklanov, N. T. Gurin, and S. G. Novikov

Ul'yanovsk State University, Ul'yanovsk, Russia
e-mail: svast@sv.ulsu.ru
Received March 26, 2002

Abstract—It is suggested to increase the magnetic sensitivity of planar-diffusion triacs by exposure to X-ray radiation. Additional increase in the magnetic sensitivity can be achieved by mechanically introducing surface defects into the device structure. Processes and mechanisms responsible for increased sensitivity under conditions of various galvanomagnetic effects are considered. © 2002 MAIK "Nauka/Interperiodica".

Galvanomagnetic devices constitute the elemental basis for magnetoelectronics—one of the promising directions of modern electronics. These are devices the operation of which is based on the joint action of electric and magnetic fields upon a semiconductor. The most widely used representatives of this class are the Hall emf probes, magnetoresistors, magnetodiodes, single-junction and bipolar magnetotransistors, magnetothyristors, and devices employing galvanomagnetorecombination effect [1] developed and implemented into practice in the past decades. Of special interest are investigations aimed at the creation of magnetotriacs, representing devices with symmetric S-shaped current–voltage characteristics. These devices can be used as bidirectional elements in many dc and ac instruments, such as contactless switches, electronic compasses, magnetic readout heads, collectorless motors, etc. [1].

Magnetotriacs can be created on the basis of well-known planar-diffusion triacs (PDTs) [2]. The magnetic sensitivity of PDTs can be increased by irradiation [3, 4], which produces the necessary surface defects increasing the surface recombination rate *s*—one of the main parameters determining the magnetic sensitivity.

Previously, we studied modification of PDT-based optocouplers by exposure to α- and β-radiation [4] and to 30-keV electrons [3], which significantly improved the magnetic sensitivity of these devices. Below we present the results of the next step of investigations in this direction, obtained using another factor of defect production in the surface layers of PDT structures. Here, the task of increasing the magnetic sensitivity of PDTs triacs was solved by exposure to X-ray radiation capable of producing structural defects enhancing some galvanomagnetic effects.

The objects for investigation were two galvanically controlled PDT structures (with a control current fed to the *p*-base) manufactured at Ul'yanovsk Radio Tube Plant. The surface of one triac structure (sample 1) was coated with a layer of OP-432 compound with a thickness of about 50 μm, which reliably insulated flexible wire conductors from contacts of the PDT structure (this is one of the basic technological operations involved in the large-scale production of such devices). The second triac structure (sample 2) represented a galvanically controlled PDT without a protective compound coating. In order to increase the magnetic sensitivity of sample 2 and mechanically introduce additional surface defects, a 200-μm-wide, 50-μm-deep groove was cut with a diamond tool along the axis of symmetry (thyristor interface) of the PDT structure. It should be noted that the magnetic sensitivity of commercial multilayer semiconductor structures, such as thyristors and triacs, is usually manifested rather weakly, since the current transfer coefficients of the component transistor weakly depend on the magnetic induction and the on the surface recombination rate [5].

Prior to irradiation, the sample structures were studied for the magnetic sensitivity, in particular, in the control current transfer mode. Exposed to a magnetic field with induction *B*, sample 1 exhibited a very weak magnetic response even at a maximum gate current. Sample 2 (with a mechanically cut channel) showed a relatively high sensitivity with respect to application of the external magnetic field, which was comparable to analogous parameters of commercial galvanomagnetic devices. For example, in the interval of magnetic inductions $-1\ \text{T} < B < 1\ \text{T}$, the maximum sensitivity was 12 V/T at a gate current of $I_g = 2.36$ mA.

Owing to the surface defects introduced into the structure of sample 2, intensity of the carrier production–recombination processes on the surface becomes much higher as compared to that in the volume of the PDT structure. Exposed to an external magnetic field B^+ (the positive direction is selected conditionally), when the Lorentz force drives the charge carriers to deviate toward the surface, the carriers exhibit intense recombination. This results in an increase in the *n*-base
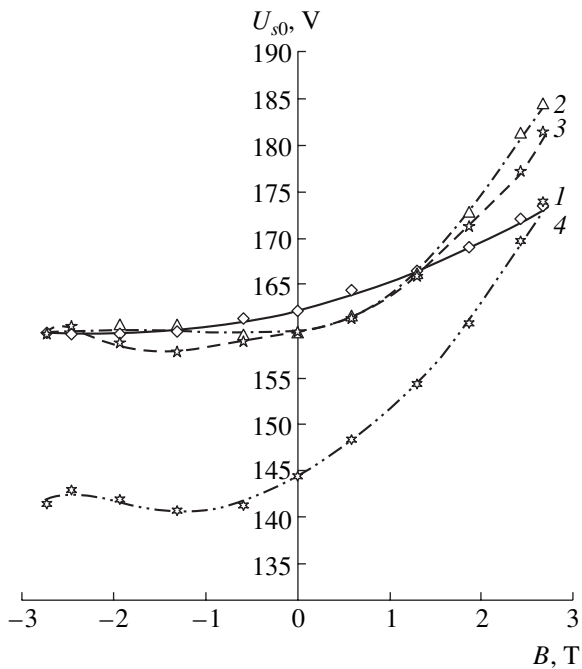
Fig. 1. Plots of the switching voltage versus magnetic field for sample 1 measured at a gate current of $I_g = 2$ mA (*1*) before ($D = 0$) and (*2–4*) after X-ray irradiation to various doses $D = 3 \times 10^{15}$ (*2*), 7×10^{15} (*3*), and 1×10^{16} cm^{-2} (*4*).
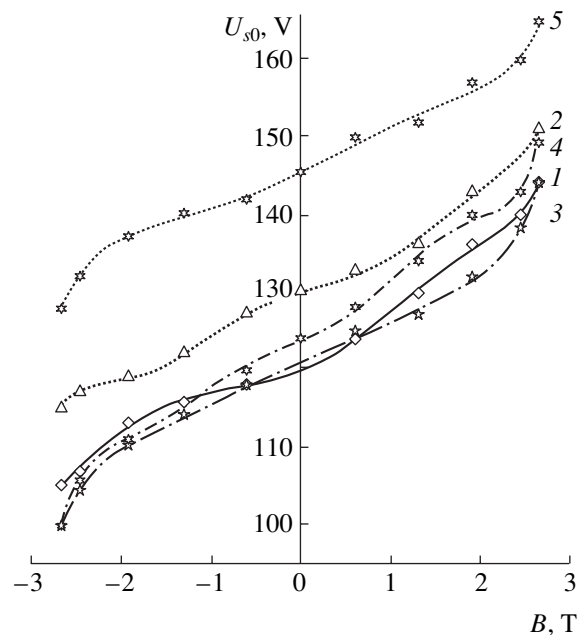

Fig. 2. Plots of the switching voltage versus magnetic field for sample 2 measured at a gate current of $I_g = 2.28$ mA (*1*) before ($D = 0$) and (*2–5*) after X-ray irradiation to various doses $D = 7 \times 10^{15}$ (*2*), 9×10^{15} (*3*), 1×10^{16} (*4*), and 2×10^{16} cm^{-2} (*5*).

resistance and a decrease in the transfer coefficient of a "longitudinal" *pnp*-transistor, leading to growth of the switching voltage U_{s0} depending on the magnetic field determined by the magnetoconcentration effect. When the magnetic field direction changes to opposite (B^-), the charge carriers deviate from the upper surface (where the recombination rate is high) toward the bulk (where the recombination rate is low). This leads to an increase in the concentration of carriers contributing to the gate current of the *pnp*-transistor and, hence, in the corresponding transfer coefficient. As a result, the switching voltage drops.

In the course of the experiment, samples 1 and 2 were exposed at room temperature to the radiation of an X-ray tube operating at an accelerating voltage of 100 kV. The radiation intensity (dose rate) was 9.6×10^{11} s^{-1} cm^{-2}. After the exposure, the main static parameters of the current–voltage characteristic of sample 1 changed rather insignificantly. Figure 1 shows experimental plots of the switching voltage U_{s0} versus magnetic induction B measured before and after irradiation to a total dose of 10^{16} cm^{-2}. A comparison of the curves shows a significant increase in the magnetic sensitivity of PDT upon exposure. A change in the magnetic sensitivity is more pronounced for the positive (B^+) than for the negative (B^-) direction of the magnetic field, which is evidence for a polar character of the magnetic sensitivity.

The irradiation of sample 2 under the same conditions was performed in several steps to a total dose of 2×10^{16} cm^{-2}. The exposure did not lead to significant variation in the main static parameters of the current–voltage characteristic of this sample. Nor did it markedly changed the magnetic sensitivity. Probably, the irradiation of sample 2 did not significantly modify the relation between the carrier production–recombination processes on the surface and in the bulk, so that the magnetoconcentration effect was not operative (Fig. 2). During the irradiation of an unprotected PDT structure, the radiation defects are generated over the entire thickness of *p*-regions of the PDT structure [6]. The fraction of radiation-induced surface defects is relatively small as compared to the fraction of mechanically produced defects and, hence, the transfer coefficient of the *pnp*-transistor changes rather insignificantly. Accordingly, the magnetic sensitivity of the device remains essentially unchanged.

Conclusions. Based on the results of investigations we may conclude the following.

(i) Modification of the PDT structure by exposure to the X-ray radiation allows the magnetic sensitivity of triacs with respect to the external magnetic field; the results confirm the general laws of this approach employing various types of radiation sources.

(ii) The magnetic sensitivity of PDTs can be increased both by the method of radiation modification and by mechanical methods.

(iii) The enhanced magnetic sensitivity of radiation-modified PDT structures is related to a change in the magnetic field dependence of the transfer coefficient of the *pnp*-transistor under the conditions of operation of the magnetoconcentration effect.

(iv) Application of the control action allows the magnetic sensitivity of radiation-modified PDTs to be varied in a preset range.

(v) PDTs possess high radiation stability.

REFERENCES

1. V. I. Stafeev and É. I. Karakushan, *Magnetodiodes. Novel Semiconductor Devices with High Sensitivity to Magnetic Field* (Nauka, Moscow, 1975), p. 216.

2. S. B. Baklanov, V. V. Gaĭtan, and N. T. Gurin, RF Patent No. 2022412, Byull. Izobret., No. 20 (1994).

3. S. I. Vorontsov, S. B. Baklanov, S. G. Novikov, *et al.*, Uch. Zap. Ul'yanovsk. Gos. Univ., Ser. Fiz., No. 2 (9), 86 (2000).

4. S. G. Novikov, S. B. Baklanov, N. T. Gurin, and S. I. Vorontsov, Pis'ma Zh. Tekh. Fiz. **27** (8), 53 (2000) [Tech. Phys. Lett. **27**, 331 (2000)].

5. I. M. Vikulin, L. F. Vikulina, and V. I. Stafeev, *Galvanomagnetic Devices* (Radio i Svyaz', Moscow, 1983), p. 104.

6. V. S. Pershenkov, V. D. Popov, and A. V. Shal'nov, *Surface Radiation Effects in Integrated Circuit Elements* (Énergoatomizdat, Moscow, 1988), p. 256.

Translated by P. Pozdeev

On the Mechanism of Electron Conductivity in Lanthanum Metaniobate

A. P. Pivovarova, V. I. Strakhov, and V. P. Popov

St. Petersburg State Technological Institute (Technical University), St. Petersburg, Russia

Received December 17, 2001

Abstract—The temperature dependence of the conductivity of lanthanum metaniobate was studied on samples heated in air from 100 to 1100°C. The electronic and hole conductivity components were separated by the method of a blocking electrode. The temperature dependence of the electronic conductivity of $LaNb_3O_9$ was calculated using the standard thermochemical data for Nb_2O_5. It is concluded that the thermodynamic approach based on the thermochemical data for oxides is applicable to calculations of the temperature dependence of conductivity in complex oxygen-containing compounds. © 2002 MAIK "Nauka/Interperiodica".

As is known, lanthanum metaniobate $LaNb_3O_9$ possesses a cation-deficient perovskite structure of the oxygen-octahedral type. In this structure, NbO_6 octahedra (representing the main structural motif) share vertices to form a three-dimensional carcass with bulky La^{3+} cations occupying one-third of the cubooctahedral cavities [1], as reflected by the conventional formula $La_{1/3}\square_{2/3}NbO_3$. It was established [2] that annealed (i.e., stoichiometric) lanthanum metaniobate is an ionic conductor at low temperatures (below 800 K), in which the current is transferred by La^{3+} cations migrating via the structural vacancies, and an electronic-type conductor at higher temperatures. However, it is known that niobium-containing oxides synthesized at high temperatures are always partly reduced, the degree of reduction being dependent on the temperature, gaseous medium, and duration of the thermal treatment.

In this content, we have studied the mechanism of conductivity in both reduced samples of $LaNb_3O_{9-x}$ (obtained by quenching from the temperature of synthesis) and the stoichiometric lanthanum metaniobate $LaNb_3O_9$ (prepared by annealing for 100 h at 350°C).

Samples of lanthanum metaniobate for conductivity measurements were prepared, in the form of disks with a diameter of 10–12 mm and thickness of 1–2 mm, proceeding from La_2O_3 and Nb_2O_5 oxides of special purity grade. The synthesis was conducted according to the ceramic technology, involving sintering in air at 900°C for 15 h and 1250°C for 10 h, with intermediate grinding, followed by quenching in air from the final temperature. The completion of synthesis was monitored by X-ray diffraction on a DRON-3.0 diffractometer using CuK_α radiation. The open porosity of the samples was about 1%. The electrodes were formed on the sample surface by fusing a silver paste composition at 780°C.

The conductivity measurements were performed by a two-point probe techniques in air in the temperature range from 100 to 1100°C, in the course of a step-by-step heating (or cooling) of the samples at a 40–50°C step. Each heating step was followed by keeping the sample until establishing equilibrium values of both dc and ac (10^3 Hz) conductivity, as measured with the aid of a U-63 teraohmmeter, a VK-72E digital ohmmeter, and an E-82 ac bridge. The dc conductivity was measured using small (0.5 V) applied electric fields after a prolonged (up to 30 min) period of current decay. The nonporous silver electrodes favored blocking of the mobile oxygen ions, which allowed us to use a polarization technique for separating the ionic and electronic conductivity components as described in [3]. According to this method, the results of ac measurements determine the total conductivity, while the dc measurements give the electronic conductivity component: $\sigma_\Sigma = \sigma_1 = \sigma_2 + \sigma_3$, $\sigma_4 = \sigma_2$ (where $\sigma = \sigma_1$ is the ac conductivity, σ_2 and σ_3 are the electronic and ionic components, respectively, and σ_4 is the dc conductivity).

The curves of $\log\sigma$ versus $1/T$ obtained by ac measurements on the sample annealed at 350°C significantly differ from analogous curves for the unannealed samples (cf. curves *1* and *2* in the figure), the difference being especially pronounced in the low-temperature region. The temperature dependence of the ac conductivity of the annealed samples (curve *1*) is characterized by two linear portions with a smooth transition at 400–600°C. This behavior coincides with the data reported in [2], according to which the low-temperature portion with an activation energy of $E^* = 0.2$ eV corresponds to the ionic conductivity mediated by La^{3+} cations. Measured above 600°C, the curves of dc and ac conductivity coincide with each other (curves *3* and *4* in the figure), which is evidence of the purely electronic character of the conductivity (with an activation energy of 1.6 eV) in this temperature region.
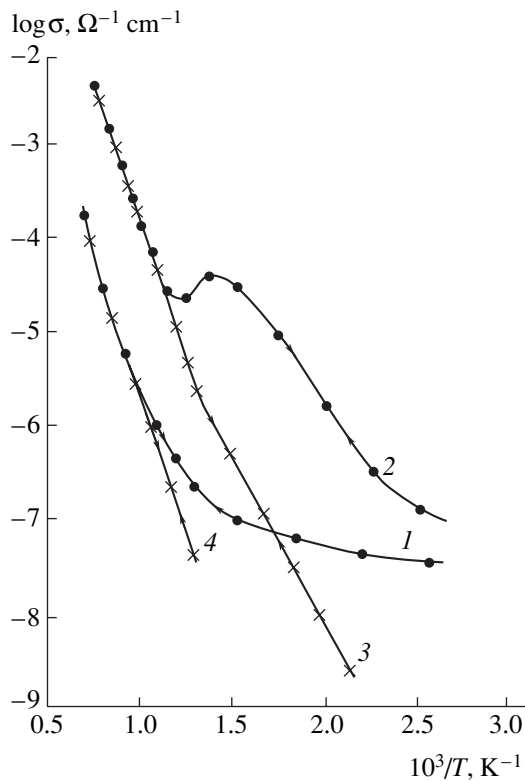
Temperature dependence of the (*1, 2*) ac and (*3, 4*) dc conductivity of lanthanum metaniobate: (*1, 4*) stoichiometric $LaNb_3O_9$ (upon annealing for 100 h at 350°C); (*2, 3*) unannealed $LaNb_3O_{9-x}$.

Let us consider curve *2* representing the temperature dependence of the ac (total) conductivity for the nonstoichiometric (unannealed) lanthanum metaniobate. A significant increase in the conductivity observed on heating the sample is related to the presence of additional current carriers represented by electrons and oxygen vacancies in the reduced compound. The activation energy (0.65 eV) in the low-temperature region (130–400°C) probably corresponds to the anionic conductivity mediated by O^{2-} ions traveling via oxygen vacancies. In this temperature interval, the anionic conductivity obviously dominates over the cationic component. For example, the contribution of the cationic component at 300°C accounts for only about 1% of the total ionic conductivity.

Note that curve *2* exhibits a local maximum at ~470°C, which is probably related to a phase transformation of the crystallographic shear type in $LaNb_3O_{9-x}$. Such phase transformations, taking place in Nb_2O_{5-x}, TiO_{2-x}, and WO_{3-x} [4], lead to vanishing of the anion vacancies and, hence, of the anionic conductivity component. Indeed, the total conductivity exhibits exponential growth ($E^* = 1.4$ eV) above 500°C and coincides with the dc conductivity, which indicates that the sample becomes a purely electronic conductor. The region of the proposed phase transformation is also character-

ized by a change in the slope of curve *4* describing the electronic conductivity, whereby the corresponding activation energy decreases to 1.0 eV. It should be also noted that the temperature dependences measured on heating and on cooling coincide to within the experimental error.

Thus, niobium-containing oxides reduced by heating in air exhibit a partial reversible loss of oxygen and become nonstoichiometric. According to the theory of defects in crystals [5], the removal of one oxygen atom leads to the localization of two electrons at the oxygen vacancy with an effective zero charge: $O_0 \rightleftharpoons V_0 + (1/2)O_2$, where O_0 is oxygen at a lattice site with zero effective charge and V_0 is the oxygen vacancy with zero effective charge.

Because Nb^{5+} is susceptible to reduction (attachment of electrons), the two electrons localized at the oxygen vacancy are drawn toward the two neighboring Nb^{5+} cations (entering into the oxygen octahedra) to reduce their charges to +4. As a result, two oxygen octahedra centered at Nb^{5+} cations are replaced by distorted octahedra containing Nb^{4+} cations and one oxygen vacancy with an effective charge +2: $V_0 \rightleftharpoons V_0^{\cdot\cdot} + 2\bar{e}$, where $V_0^{\cdot\cdot}$ denotes the double ionized oxygen vacancy. Thus, the overall process can be described by the following scheme:

$$2Nb^{5+} + V_0 \rightleftharpoons V_0^{\cdot\cdot} + 2Nb^{4+}, \qquad (1)$$
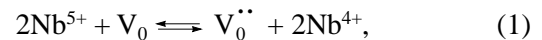
which corresponds to the reduction of Nb^{5+} via the reaction

$$LaNb_3O_9 \rightleftharpoons LaNb_{3-2x}^{5+}Nb_{2x}^{4+}O_{9-x} + (x/2)O_2\uparrow, \quad (2)$$
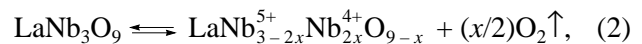
where *x* is the degree of nonstoichiometry. Since an Nb^{4+} ion possesses an excess weakly bound electron, it is probably this ion that participates in the conductivity.

From the standpoint of the band theory, the above process corresponds to the transfer of two electrons from the valence 2*p* band of oxygen to the empty 4*d* band of niobium cations; therefore, the bandgap (ΔE) must be equal to the enthalpy of formation (ΔH) of Nb^{4+} cation.

Since these considerations are valid for all Nb-containing oxide compounds, the process of charge transport in $LaNb_3O_9$ can be described using the thermochemical data for Nb_2O_5 [4]:

$$\Delta H_{298}^0(Nb_2O_5) = 1900 \text{ kJ/mol},$$

$$\Delta H_{298}^0(2NbO_2) = 1600 \text{ kJ/mol},$$

$$\Delta S_{298}^0 = 60 \text{ kJ/mol (for reduction reaction)}.$$

Then, according to [6], the enthalpy of reaction (1) is

$$\Delta H^0_{298} = \Delta H^0_{298}(Nb_2O_5) - \Delta H^0_{298}(2NbO_2)$$
$$= 300 \text{ kJ/mol} = 3.10 \text{ eV}.$$

Thus, the bandgap value (3.10 eV) calculated proceeding from the thermodynamic quantities is in good agreement with the experimental data on the conductivity of $LaNb_3O_9$ annealed at a low temperature, according to which the bandgap is 3.20 eV ($\Delta E = 2E^*$, where $E^* = 1.60$ eV is the activation energy).

The density of free electrons can be evaluated using the law of mass action:

$$n = NP_0^{-1/4}K^{1/2}$$
$$= NP_0^{-1/2}\exp(\Delta S^0/2R)\exp(-\Delta H^0/2RT), \quad (3)$$

where N is the concentration of niobium atoms and P is the partial pressure of oxygen. By approximate estimates, $N = 1.6 \times 10^{22}$ cm^{-3}, $P \cong 1$ atm, and $\exp(\Delta S^0/2R) \approx 19$, from which we obtain $n \sim 30 \times 10^{22}\exp(-\Delta H^0/2RT)$. Therefore,

$$\sigma = n\mu e = 30 \times 10^{22} \times 0.01 \times 10^{-19}\exp(-\Delta H^0/2RT)$$
$$= 3 \times 10^2\exp(-1.55/2RT), \quad (4)$$

where e is the electron charge and μ is the electron mobility. Based on an analysis of the published data for polycrystalline dielectrics and assuming the hopping mechanism of charge transfer, we estimated the latter quantity at ~0.01 cm^2/(V s).

Thus, the theoretical preexponential factor amounts to 3×10^2 Ω^{-1} cm^{-1}. Extrapolation of the experimental curves to $T \longrightarrow \infty$ yields a close value of 10^2 Ω^{-1} cm^{-1}, from which it follows that

$$\sigma = 10^2\exp(1.60/2RT). \quad (5)$$

This coincidence of the experimental relationship (5) and theoretical estimate (4) gives us grounds to ascertain that the thermodynamic approach can be employed to calculate the temperature dependence of conductivity in well-annealed samples (containing negligible small number of vacancies) of some complex oxygen-containing niobates, proceeding from the thermochemical data for oxides. It should be noted that, according to data from [7], the activation energy for Nb_2O_5 is 1.39 eV. The activation energy for the electronic conductivity of a reduced sample is somewhat lower than that of the stoichiometric oxide and amounts to 1.4 eV, which coinciding with the value for Nb_2O_5. Since a decrease in the activation energy is related to an increase in the degree of reduction, it is evident that this degree is higher in Nb_2O_5 than in stoichiometric $LaNb_3O_9$. However, taking into account that the authors of [7] did not perform prolonged annealing of their samples, direct comparison with their data would be inexpedient.

Since the parameters of conductivity—experimental for $LaNb_3O_9$ and theoretical for Nb_2O_5—coincide, we may probably conclude that lanthanum cations are not significantly influencing the electronic conductivity of lanthanum metaniobate at high temperatures (above 500°C) and, hence, the hopping mechanism of charge transfer via $Nb^{4+} \longrightarrow Nb^{5+}$ is inherent in this compound as well. In addition, it is known that La^{3+} is not susceptible to reduction and cannot serve as the donor of electrons. The La^{3+} ions play a significant role only in the low-temperature region (below 500°C), by accounting for the cationic current in annealed samples.

REFERENCES

1. P. N. Iver and A. J. Smith, Acta Crystallogr. **23**, 740 (1967).
2. A. M. George and A. N. Virkar, J. Phys. Chem. Solids, No. 7, 743 (1988).
3. P. A. Tikhonov, A. M. Kuznetsov, and A. V. Kravchinskaya, Zavod. Lab., No. 7, 837 (1978).
4. *Physicochemical Properties of Oxides: A Handbook*, Ed. by G. V. Samsonov (Metallurgiya, Moscow, 1978), pp. 30–225.
5. P. Kofstad, *Nonstoichiometry, Diffusion, and Electrical Conductivity in Binary Metal Oxides* (Wiley, New York, 1972; Mir, Moscow, 1975).
6. V. P. Popov, Zh. Prikl. Khim. **65** (5), 1113 (1992).
7. M. K. Paria and H. S. Marti, J. Mater. Sci. Lett. **3** (12), 1039 (1984).

Translated by P. Pozdeev

The Effect of Pulsed Magnetic Fields on the Real Structure of Indium Arsenide Crystals

M. N. Levin, G. V. Semenova, T. P. Sushkova, É. A. Dolgopolova, and V. V. Postnikov

Voronezh State University, Voronezh, Russia
e-mail: levin@lev.vsu.ru
Received May 6, 2002

Abstract—Experiments on InAs crystals demonstrate that exposure to pulsed magnetic fields can increase the phase homogeneity and structural perfection of the binary phases of $A^{III}B^V$ semiconductor compounds. © *2002 MAIK "Nauka/Interperiodica".*

The unique ability of relatively weak (<1 T) pulsed magnetic fields (PMFs) to modify the real structure and physical properties of diamagnetic crystals was originally reported in [1]. The PMF-induced changes in the microstructure were first observed in alkali halide crystals [1] and, later, in $A^{III}B^V$ semiconductor compounds [2] and in Czochralski-grown silicon (Cs–Si) single crystals [3]. In all cases, the exposure to PMFs lead to decomposition of the defect complexes with the formation of new, mobile defects involved in a long-term multistage transformation of the real crystal structure. Interpretation of the observed effects is based on the notion of a magnetic field influencing the kinetics of spin-dependent reactions involving radical pairs [4]. It is believed that weak magnetic fields can remove prohibition from the electron transitions with a spin change. This leads to weakening of the bonds in defect complexes, while the real crystal structure is modified at the expense of thermal and elastic energy of the crystal lattice [3, 5, 6].

Despite clear macroscopic manifestations of the PMF-induced effects, possessing a quantum nature, the problem of using these effects for a positive controlled modification of semiconductor crystals is still open. In this context, the purpose of this study was to determine the possibility of using PMF treatments to increase the quality of the crystals of binary semiconductor compounds of the $A^{III}B^V$ type.

We selected InAs single crystals as the model object. The sample crystals were grown by a double-temperature technique, followed by directional crystallization of the melt by the Bridgman method. The initial components were In and As of special purity grade (OSCh-11-5 and OSCh-9-5, respectively), the latter being additionally purified from oxides by double sublimation in vacuum. For the synthesis, a ceramic boat with In was placed in one end of a thick-walled quartz ampule and As (volatile component) was placed in the other end. The ampule was sealed, evacuated to a residual pressure of 5×10^{-4} GPa, placed into a furnace, and positioned so as to ensure that the boat with In occurred at a temperature 5–10 K higher than the temperature of liquidus of the target alloy. The required pressure in the system was set by controlling the temperature of the "cold" end with the volatile component in accordance with the temperature dependence of the saturated vapor pressure above solid arsenic. The target alloy ingots possessed a coarse-block structure. The experiments were performed with $5 \times 4 \times 4$ mm samples cut from the central part of the ingots. The sample surface to be studied was prepared by mechanical polishing.

The action of PMFs upon InAs crystals was studied by electron-probe microanalysis (EPMA) and X-ray diffraction. The EPMA data were used to determine the distribution of chemical elements on the sample surface. The measurements were performed in a CamScan S4 scanning electron microscope equipped with an energy-dispersive X-ray analysis system of the Link AN10/55S type. The planar distribution of elements was determined in the surface layer with a thickness of about 1 μm, by measuring the intensity of a characteristic X-ray radiation excited by an electron beam scanning over the sample surface. The X-ray diffraction measurements were performed in a powder diffraction mode on a DRON 4-07 diffractometer using crystal-monochromated CoK_α radiation ($\lambda = 0.154059$ nm). The diffraction patterns were recorded in the course of automated angular scanning with a step of 0.1°, an exposure time of 1 s at each point, and the sample rotated in its own plane.

The PMF treatment consisted in exposure to a series of 1500 symmetric pulses of a triangular shape with an amplitude of $B = 0.3$ T, a duration of $t = 4 \times 10^{-5}$ s, and a repetition rate of $f = 50$ Hz. The field pulses were generated by discharge of a capacitor bank through a low-inductance solenoid coil. The samples were not specially oriented inside the coil during the PMF treatment. After the PMF treatment, the InAs samples were stored at room temperature, together with control samples not exposed to magnetic field.

By the EPMA data, a short-time (for several seconds) PMF treatment of InAs crystals initiates a long-term (lasting over thousands of hours at $T = 300$ K) two-stage phase transformation. The results of the PMF action upon the surface composition of samples studied are illustrated in Fig. 1. In the first stage, the InAs crystal components segregate to form separate phases (Fig. 1b); in the second stage, the samples exhibit the reverse process, whereby the segregated phases are dissolved with recovery of InAs as the chemical compound (Fig. 1c). A comparison of the initial and final states of the crystal shows evidence that the phase composition upon the PMF treatment becomes more homogeneous, at least in a ~1-μm-thick surface layer. Characteristics of the control sample, cut from the same ingot but not exposed to PMFs, remained unchanged.

According to the X-ray diffraction data (Fig. 2), the PMF treatment leads to an irreversible increase in the degree of texturing of the sample crystals. Before the treatment, the X-ray diffractogram displayed four clearly pronounced lines corresponding to the (111), (220), and (311) planes of InAs. Upon exposure to PMFs, the intensity of the (220) reflection increased several times relative to the (111), (311), and background intensities. This is evidence of an increase in the degree of sample texturing in the $\langle 110 \rangle$ direction and of a more perfect structure of the crystal.

The main factor of sensitivity of the InAs crystals with respect to PMFs is the presence of complexes of the intrinsic point defects capable of decomposing under the action of a weak magnetic field. Dominating in the $A^{III}B^{V}$ compounds are the nonstoichiometry defects related to vacancies of the group V element and the antistructural defects, the interaction of which leads to the formation of vacancy–defect complexes [7].

With an allowance for the model notions developed previously, the most probable starting mechanism involved in the PMF action upon the $A^{III}B^{V}$ semiconductor compounds consists in weakening of the stressed chemical bonds of the initial vacancy–defect complexes. This is caused by the PMF-induced intercombination transitions of the electrons involved in these bonds. The hypothesis of the PMF-induced decay of the complexes of intrinsic defects in $A^{III}B^{V}$ crystals, accompanied by the formation of mobile point defects (vacancies and intrinsic atoms), explains the local segregation of binary phases on the surface (which serves as a natural sink for the defects). Formed as a result of decomposition of the initial defect complexes, the phases of individual elements are metastable and tend to decay with the formation of the binary compound, which results in homogenization of the crystal and a decrease in the density of defects. The duration of these processes is determined by the rate of diffusion of the point defects (intrinsic atoms of the crystal) at a given temperature ($T = 300$ K in our experiments).

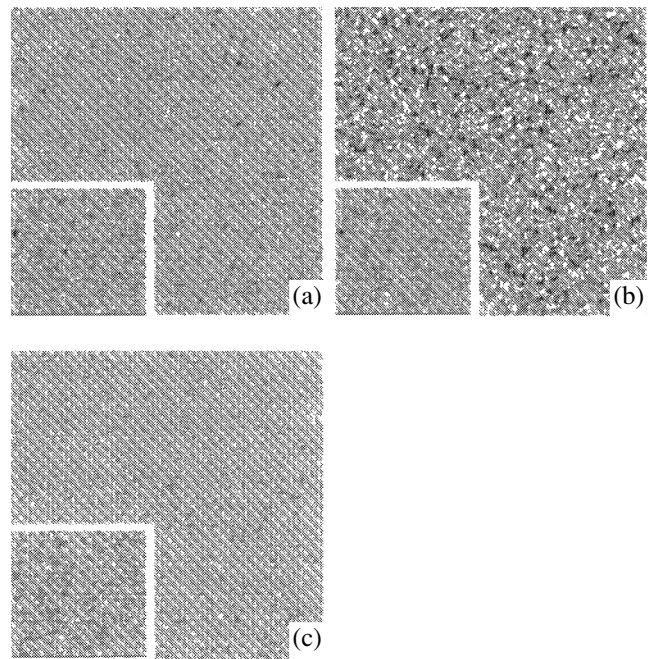The main conclusion from this study is that the short-time PMF treatment of InAs crystals initiates a

Fig. 1. EPMA patterns showing the planar distribution of elements in the surface layer (~1 μm thick) of an InAs crystal (a) before PMF treatment and (b) 5 days and (c) 50 days after PMF treatment (magnification, ×500). The insets show the surface of a control sample not treated in PMFs, otherwise identical to the treated sample.
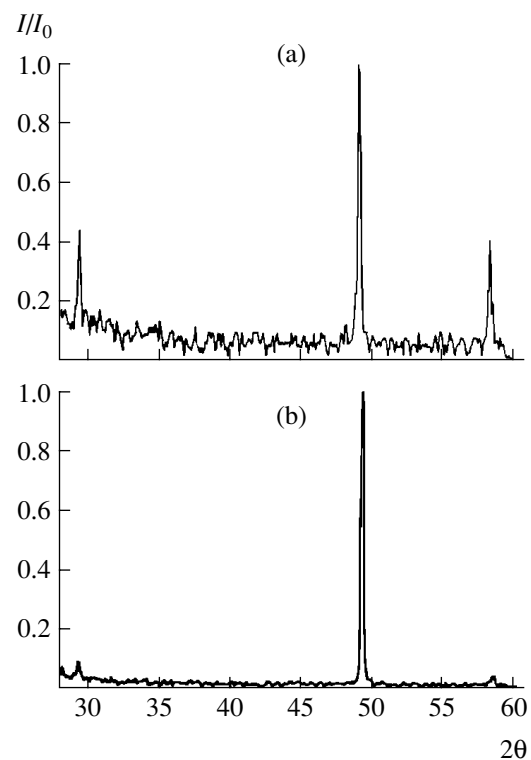

Fig. 2. X-ray diffractograms (relative line intensity I/I_0 versus diffraction angle 2θ) of an InAs crystal measured (a) before PMF treatment and (b) 10 days after PMF treatment.

long-term variation of their phase, structure, and thermodynamic state, leading to an increase in the composition homogeneity and in the structural perfection of the crystals. Thus, the PMF treatment can be effectively used to improve the quality of crystals of binary semiconductor phases of the $A^{III}B^{V}$ type.

REFERENCES

1. G. I. Distler, V. M. Kanevskiĭ, V. V. Moskvin, *et al.*, Dokl. Akad. Nauk SSSR **268**, 591 (1983) [Sov. Phys. Dokl. **28**, 43 (1983)].

2. V. N. Davydov, V. A. Loskutova, and E. P. Naĭden, Fiz. Tekh. Poluprovodn. (Leningrad) **23** (9), 1596 (1989) [Sov. Phys. Semicond. **23**, 989 (1989)].

3. M. N. Levin and B. A. Zon, Zh. Éksp. Teor. Fiz. **111** (4), 1373 (1997) [JETP **84**, 760 (1997)].

4. Ya. B. Zel'dovich, A. L. Buchachenko, and E. L. Frankevich, Usp. Fiz. Nauk **155** (1), 3 (1988) [Sov. Phys. Usp. **31**, 385 (1988)].

5. M. I. Molotskii, Mater. Sci. Eng. A **287**, 248 (2000).

6. Yu. I. Golovin, R. B. Morgunov, V. E. Ivanov, and A. A. Dmitrievskiĭ, Zh. Éksp. Teor. Fiz. **117** (6), 1080 (2000) [JETP **90**, 939 (2000)].

7. S. V. Bulyarskiĭ and V. I. Fistul', *Thermodynamics and Kinetics of Interacting Defects in Semiconductors* (Nauka, Moscow, 1997).

Translated by P. Pozdeev

On a Similarity Criterion for Plasma Accelerators of the Stationary Plasma Thruster Type

A. I. Bugrova, A. S. Lipatov, A. I. Morozov, and D. V. Churbanov

Moscow Institute of Radio Engineering, Electronics, and Automatics (Technical University),
Moscow, Russia
Received March 21, 2002

Abstract—Operation of a stationary plasma accelerator of the ATON type employing various working gases is considered. Using a proposed similarity criterion, an optimum operation regime of the accelerator for krypton is selected. Comparative integral parameters of an accelerator operating on krypton and xenon are presented. © *2002 MAIK "Nauka/Interperiodica".*

As is known, the physical processes in a stationary plasma thruster (SPT) are characterized by three basic dimensionless parameters of the operation regime:

(i) coefficient of the applied voltage loss,

$$1 - \chi \equiv 1 - \frac{\Delta U}{U_d},$$

where ΔU is the energy spent for ionization and various losses (ΔU is comparable with the average potential in the ionization zone) and U_d is the discharge voltage;

(ii) coefficient of the propellant (working gas) usage,

$$\mu = \frac{\dot{m}_t}{\dot{m}} = J_i/J_{\dot{m}},$$

where J_i is the ion current in the output channel (related to the effective degree of ionization), $J_{\dot{m}} = (e/M)\dot{m}$ is the mass current, e is the electron charge, M is the atomic mass of the working gas, and $\dot{m}$ is the propellant consumption rate; and

(iii) exchange parameter characterizing the efficiency of current flowing in the channel,

$$\xi = J_d/J_{\dot{m}},$$

where J_d is the discharge current.

Once the dimensionless quantities χ, μ, and ξ are known, the integral parameters of an accelerator employing a given working gas can be calculated, in particular, the propulsion

$$F = \sqrt{\frac{2e}{M}} \mu \dot{m} \sqrt{U_d(1-\chi)},$$

the consumed power

$$W = J_d U_d = \xi J_{\dot{m}} U_d,$$

and others. Previously [1, 2], these generalized characteristics were expressed in terms of the similarity criterion α depending on the channel width and specific consumption rate of the propellant. It was demonstrated that accelerators consuming the same working gas (xenon) at various rates operate in identical (from the standpoint of parameters χ, μ, and ξ) regimes, provided that

$$\alpha \geq \frac{\dot{m}b}{S} \sim 2 \times 10^{-2} \text{ mg/(s mm)}, \tag{1}$$

where S and b are the channel output cross section area and width, respectively.

In recent years, considerable attention has been devoted to the use of various working gases (Kr, N_2, etc.). This is related to the relatively high cost of xenon and the need in long-term thruster operation during flights to planets and asteroids. The relationship between the α-minimum necessary consumption of the working gas, ensuring optimum thruster operation, and the type of propellant is described by the formula [1, 2]

$$\alpha = \frac{1}{\sqrt{\Lambda_*}} \left(\frac{\varepsilon T_0}{\beta^2}\right)^{1/2}, \tag{2}$$

where $\Lambda_* = \Lambda\delta$, $\Lambda = \lambda_{ion}/L$ is the ionization length, L is the channel length, $\delta = \varepsilon/eU_d$, ε is the ion rate (close to ΔU), T_0 is the temperature of the working gas atoms at the SPT channel input, and $\beta = \langle \sigma v \rangle_{ion}$. Formula (2) is inconvenient in practical applications. This expression can be transformed so as to impart to it a clear physical meaning and render it convenient for use. Indeed, replacing α in formula (2) by the critical value from condition (1), we obtain a relation

$$\left(\frac{\dot{m}b}{S}\right)^2 = \frac{eU_d}{\beta^2} T_0 = \text{const}, \tag{3}$$

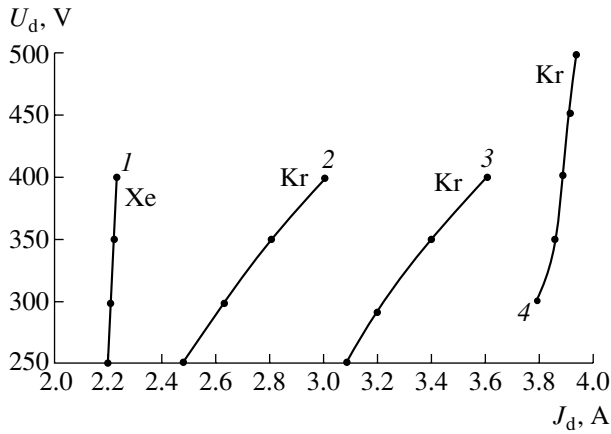according to which SPTs of the same geometry will operate in identical (from the standpoint of parameters

Fig. 1. Experimental current–voltage characteristics of a model SPT operating on (*1*) Xe and (*2*–*4*) Kr at $\dot{m}$ = 2.3 (*1*, *4*), 1.5 (*2*), and 2 mg/s (*3*).
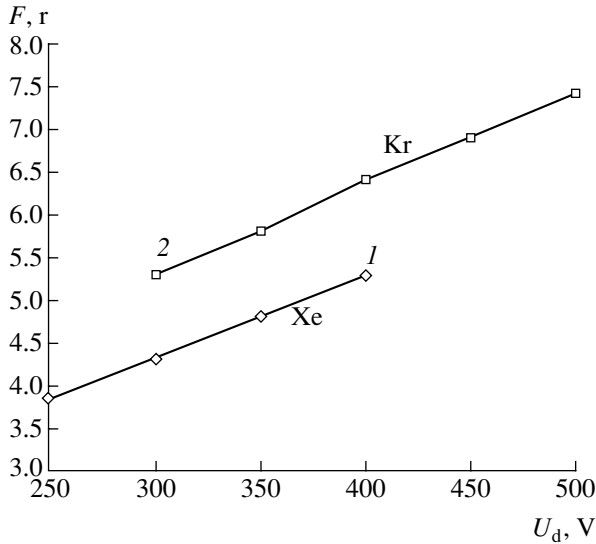

Fig. 2. Experimental plots of the propulsion *F* versus discharge voltage U_d for a model SPT operating on (*1*) Xe and (*2*) Kr at $\dot{m}$ = 2.3 mg/s.
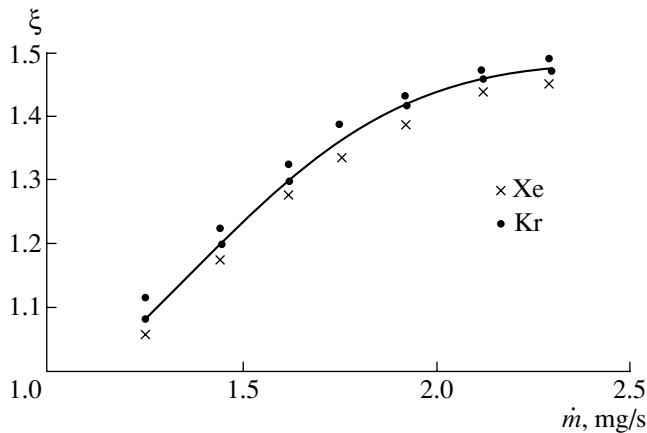

Fig. 3. Experimental plots of the exchange parameter ξ versus gas consumption rate $\dot{m}$ for a model SPT operating on Xe and Kr.

χ, μ, and ξ) regimes for the same consumption rate of the propellants. Obviously, this conclusion is valid to within the factor β. Since this factor weakly depends on the properties of working gases (even with an allowance for uncertainty in our knowledge of the electron energy distribution function and the dynamics of its variation in the thruster channel, the error in determining σ, etc.), the above conclusion concerning a constant propellant consumption rate in SPTs of the same size employing various working gases is valid to within a factor between one and two.

This conclusion was verified for a magnetoplasmadynamic thruster of the ATON type [3]. The experiments were performed on an A-3 thruster model with an inner diameter of the external insulator equal to 60 mm, a channel length of $L = 24$ mm, and an output gap width of $b = 12$ mm. The engine operated in a range of deposited powers $W = 0.5$–1.5 kW, with Xe and Kr as the working gases. The experimental results are briefly presented and analyzed below.

Current–voltage characteristics. Figure 1 shows the static J_d versus U_d curves of the model thruster operating on Xe and Kr in an optimum regime with respect to the magnetic field. As can be seen from these data, the discharge current is almost independent of the applied voltage in the range 250 V $\leq U_d \leq$ 400 V, which is evidence of a high degree of ionization of the working gas. The lower the consumption rate of Kr flowing through the anode, the greater the slope of the J_d–U_d curves and the lower the accelerator operation efficiency. For Xe, the discharge current exceeds the mass current; this is explained by the presence of a "through" electron current and of doubly charged ions (10–12%) [4]. In the thruster operating on Kr, the experimentally determined fraction of doubly charged ions is small. Taking into account that the ionization cross section of Kr is a smaller than that of Xe, a decrease in the $J_{\dot{m}}/J_d$ ratio observed in the former case seems quite reasonable.

Propulsion characteristics. Figure 2 shows the plots of propulsion *F* versus discharge voltage U_d for the two working gases (Xe and Kr) studied. As can be seen, the behavior of *F* in both cases is the same. Approximating the plots by expression (1), we can readily determine the ΔU values, which yields ~40 V for Xe and to ~60 V for Kr. Note that the ΔU values for both gases are about four times the corresponding ionization potentials.

Exchange parameter. Figure 3 presents the value of $\xi = J_d/J_{\dot{m}}$ as a function of the propellant consumption rate for Kr and Xe. As can be seen, the ξ versus $\dot{m}$ curves for the two gases coincide to within the experimental accuracy.

Coefficient of propellant usage. Figure 4 shows the plot of $\mu = J_i/J_{\dot{m}}$ characterizing the ionization effi-
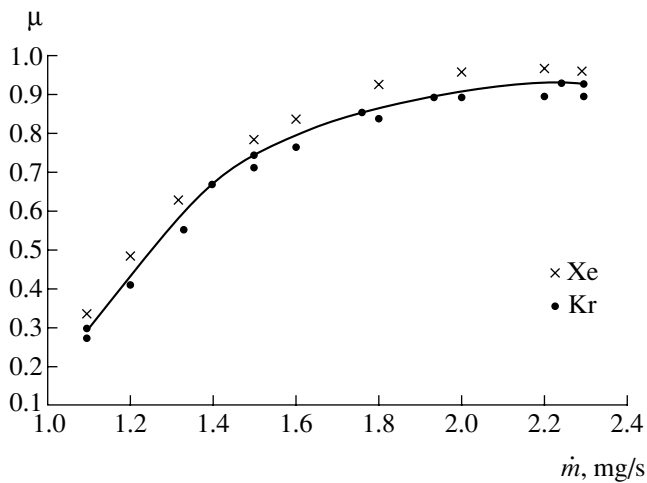
Fig. 4. Experimental plots of the propellant usage coefficient μ versus consumption rate $\dot{m}$ for a model SPT operating on Xe and Kr.

ciency versus the propellant consumption rate $\dot{m}$. As is seen, the μ values exhibit saturation with increasing consumption of the working gas and coincide, to within the experimental accuracy, for the two gases studied.

Conclusions. The results of our experiments showed the following:

(i) The critical relations of SPT operation parameters, previously determined for Xe, are valid for the engine operating on Kr as well.

(ii) SPTs employing various propellants operate in identical (from the standpoint of parameters ξ, μ, and ΔU) regimes for the same similarity criterion $\alpha \equiv \dot{m}\,b/S$ ~ 2×10^{-2} mg/(s mm).

REFERENCES

1. A. I. Morozov and I. V. Melikov, Zh. Tekh. Fiz. **44** (3), 544 (1974) [Sov. Phys. Tech. Phys. **19**, 340 (1974)].
2. A. I. Bugrova, N. A. Maslennikov, and A. I. Morozov, Zh. Tekh. Fiz. **61** (6), 45 (1991) [Sov. Phys. Tech. Phys. **36**, 612 (1991)].
3. A. I. Morozov, A. I. Bugrova, A. V. Desyatskov, *et al.*, Fiz. Plazmy **23** (7), 635 (1997) [Plasma Phys. Rep. **23**, 587 (1997)].
4. Yu. A. Ermakov *et al.*, JEPC-96-68 (1995).

Translated by P. Pozdeev

Modeling an Ensemble of Systems
Coupled by the Lennard-Jones Interaction

O. I. Gorskiĭ and Yu. P. Kuchugurnyĭ

Institute of Transport Systems and Technologies, National Academy of Sciences of Ukraine,
Dnepropetrovsk, Ukraine
Received April 15, 2002

Abstract—A system of oscillators forming a 2D lattice featuring the Lennard-Jones interaction, represented as a mathematically averaged ensemble of almost identical systems, is numerically modeled. The results show that an unstable configuration of oscillators can be retained over a greater time interval as compared to that for a single square lattice. A total energy of the system constructed as a mathematically averaged ensemble of almost identical systems is conserved up to the moment of losing stability and is not conserved after that, whereas the total energy of each system in the ensemble is conserved. © 2002 MAIK "Nauka/Interperiodica".

As is known, many-body systems coupled by the Lennard-Jones interaction can feature complicated two-dimensional (2D) correlated motions [1], which can be revealed using a special procedure with specific initial conditions. However, such initial conditions are usually ignored because it is impossible to realize the situation in practice. The structural unit in such a cluster represents a triangular equilibrium cell. It is also known that a complicated correlated motion in a conservative system can be obtained by numerically modeling a system of interacting oscillators, provided that the initial configuration is a 2D square lattice (rather than an equilibrium triangular lattice) and the interaction is described by the Lennard-Jones potential. A special feature of such a system is that the complicated symmetric and correlated motion can be observed only for a short time of the numerical modeling process (this period will be referred to as t_{sym}). This is explained by the fact that the rounding errors break the initial symmetry of the system (which would be retained in a conservative system).

Figure 1 shows a typical curve of a time-averaged kinetic energy per oscillator. A symmetric system of oscillators forming a square lattice is unstable: calculation allows the initial symmetry to be retained during a period of time not exceeding t_{sym}. It should be emphasized that the symmetry of the system begins to break up even earlier, but a graphically "rough" image of the system of oscillators retains the square pattern up to the time instant t_{sym}. The time of transition to the equilibrium triangular lattice configuration (t_{sym}) only very slightly depends on the integration step, potential constants, square lattice period, and other parameters. For example, in a system of $N = 16$ oscillators with a period of $a = 1.49$, we obtain $t_{sym} \simeq 3800$. Without increasing the accuracy of calculations (or the number of significant digits in the values of variables), the system cannot

be calculated for times greater than t_{sym} at an integration step of 0.065 (6.5×10^{-16} s). This value is almost a multiple of t_{sym} (at an appropriate change in the integration step).

In Fig. 1, curves *1* and *2* correspond to the integration steps of 0.065 and 0.0325, respectively. These curves were constructed as follows. Decreasing the integration step (for example, by half as compared to the conventional basis value), we increase the calcula-
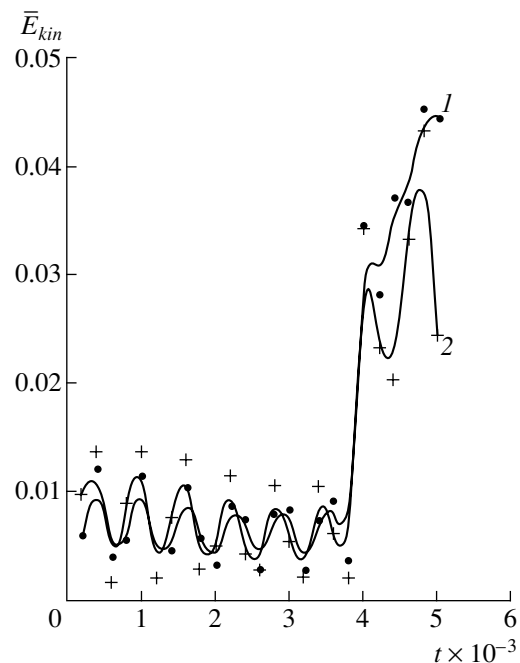

Fig. 1. Variation of the time-averaged kinetic energy per oscillator for a single system calculated at a time step of (*1*) 0.065 and (*2*) 0.0325.

tion time by a factor of 2 and take the data at a twice longer interval as compared to the conventional basis interval. Further reduction in the step does not lead to an increase in t_{sym}; moreover, this time can sometimes even decrease. Based on these facts, we can formulate one of the possible definitions of an unstable system as a system whose calculation would require unlimited complication of the algorithmic procedure. From this, we may conclude that a square lattice of oscillators coupled by the Lennard-Jones interaction can be observed as a dynamic system only for a very short time. However, there are still some doubts as to the complete validity of this conclusion.

First, if the rounding errors break the symmetry, this factor may be not identically manifested in all square lattices with a period close to the calculated one. This implies that, when the calculation is performed for an ensemble of lattices, followed by an appropriate averaging procedure, the rounding errors may compensate one another (at least over a calculation time interval greater than t_{sym}).[1]

Second, upon elapse of t_{sym}, all square lattices must break and transform into a triangular equilibrium configuration. But what happens to a lattice (with a period denoted by a_{ass}) calculated over an ensemble and then averaged? Will a_{ass} convert into the period of a triangular lattice (like the periods of all lattices in the ensemble)? The answers to these questions are not obvious. In order to elucidate the situation, we performed numerical calculations for an ensemble of square lattices coupled by the Lennard-Jones interaction.

The problem can be formulated as follows. The modeling was performed for $N = 16$ oscillators and the number of calculated lattices S in an ensemble was variable. The equations of motion were integrated at a dimensionless step of $\Delta t = 0.05$–0.13, which corresponds to the real time

$$\Delta t_{real} = \Delta t \left(\frac{m\sigma^2}{48\epsilon} \right)^{1/2}, \tag{1}$$

where ϵ and σ are the interaction constants. The dimensionless average kinetic energy per oscillator was determined as

$$\langle \epsilon_{kin} \rangle = \frac{1}{2N} \sum_{i=1}^{N} \langle (v_{xi}^2 + v_{yi}^2) \rangle. \tag{2}$$

---

[1] This conclusion does not contradict one of the possible definitions of an unstable dynamic system as the system in which whatever small external perturbations can drive it arbitrarily far from the phase trajectory. Our calculation (see below) is performed for an ensemble of systems (rather than for a single system) and follows the trajectory of a conditional system (obtained by certain averaging over an ensemble of systems with different but close initial conditions), rather than the trajectory of a single system with the given initial conditions.

The computer simulation was performed without neglect of the interaction of non-nearest neighbors, using the specific initial conditions

$$x_j = AJ, \tag{3}$$

$$y_i = AI \tag{4}$$

and zero initial conditions

$$v_{xi}(t = 0) = v_{yi}(t = 0) = 0. \tag{5}$$

The interaction potential was defined as

$$V(r_{ij}) = 4\epsilon \left[A_1 \left(\frac{\sigma}{r_{ij}} \right)^{12} - A_2 \left(\frac{\sigma}{r_{ij}} \right)^{6} \right] \tag{6}$$

and the Hamiltonian of the interaction

$$H = \sum_i \frac{p_i^2}{2m} + \sum_{i \neq j} W(r_{ij}). \tag{7}$$

The calculation of oscillations for the lattice of oscillators under consideration was performed, with an allowance for all individual motions in the ensemble of oscillators, by the formulas

$$x_i = \sum_j^S r_j (x_i)_j, \tag{8}$$

$$y_i = \sum_j^S r_j (y_i)_j, \tag{9}$$

$$(v_x)_i = \sum_j^S r_j ((v_x)_i)_j, \tag{10}$$

$$(v_y)_i = \sum_j^S r_j ((v_y)_i)_j, \tag{11}$$

where r_j are the weighting characteristics of lattices in the ensemble. It was assumed that $r_j = 1/S$ ($j = 1, 2, …, S$). This formulation can be readily generalized to include the case of unequal r_j values (see below).

For the above formulation, the dynamics of a symmetric square cluster calculated with an allowance for the ensemble can be the same as the dynamics of a single cluster, at least over a time interval in which the symmetry is retained. Moreover, this coincidence of the dynamics is a criterion for verification of the correctness of the program operation. Symmetric square lattices constituting the ensemble were determined as having an almost identical form with a small variation of
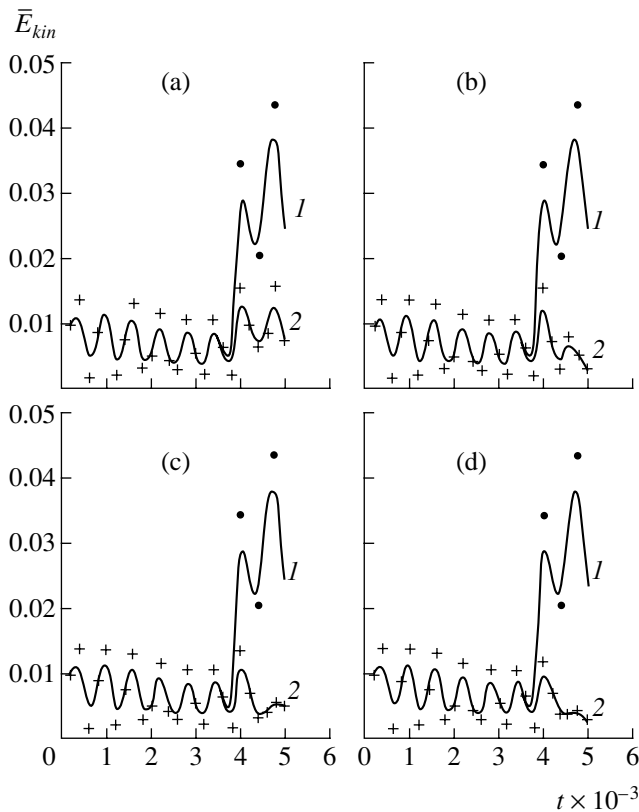
Fig. 2. Variation of the time-averaged kinetic energy per oscillator for (*1*) a single system and (*2*) a system constructed on an ensemble of almost identical systems with different numbers of lattices $S = 10$ (a), 16 (b), 20 (c), and 27 (d).
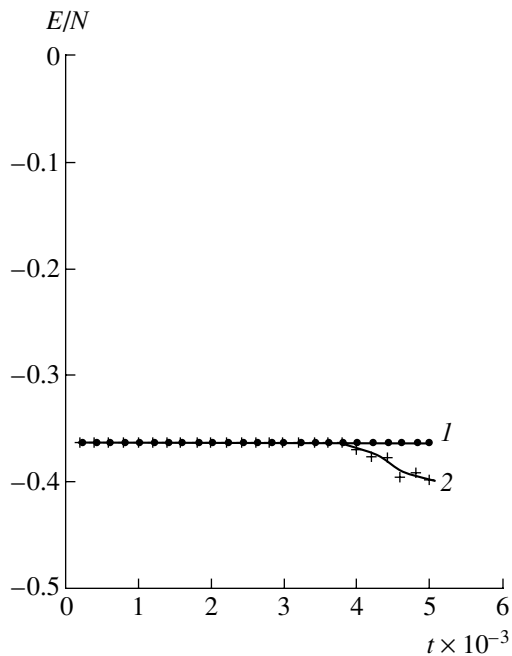

Fig. 3. Variation of the total energy E/N ($N = 16$) for (*1*) a single system and (*2*) a system constructed on an ensemble with $S = 27$.

the period as $a_i = a + 10^{-n}\epsilon$, where ϵ is a random variable in the interval [0, 1] and n varies from 4 to 16. This is explained by the expected symmetry violation in the lower orders of variables. If the lattice periods are slightly different, the weak difference in periods of the individual systems can lead to a small difference in symmetric variables of the system constructed from the ensemble. Of course, this assumption may be either correct or incorrect.

By considering an ensemble, we increase the number of variable independent parameters, such as S (number of lattices in the ensemble), a_i (lattice periods), and r_j (their contribution weights).

The symmetry breakage can be monitored visually, by considering a graphical image of the system of oscillators under consideration. Although the symmetry is traced to within a graphical pixel size, this accuracy is quite sufficient for the purpose of this study.

Figure 2 shows the breakage of symmetry in a system constructed on the ensembles with various numbers of lattices. It should be noted that this system exhibits a moderately pronounced tendency to smoothing oscillations and there is no sharp transition to the point of symmetry breakage. These features are manifested together with a tendency to retain the square lattice constructed as a mathematical average over the ensemble. It is important to note that, up to the transition point, oscillations in the standard system are indistinguishable (to within a coarse-grained plot) from oscillations in the system constructed on the ensemble. As can be seen from Fig. 2, a rather weak tendency to retain the quasi-periodic oscillations (characteristic of a square symmetric lattice of oscillators), as well as to retain the lattice proper, can be used by increasing the number of lattices in the ensemble. This obvious way, even if leading to the expected result, may require an enormously increased computational time. It is important to note that the calculation algorithm would remain the same. Even if we limit the result to increasing the lifetime of the square lattice approximately by quarter (to the knowledge of the authors, this is the only method available at present), this circumstance is very significant because unpredictable, unstable, and algorithmically complicated systems can be related to parameters not existing in the traditional formulation of the problem involving the Lennard-Jones potential.

It should be also noted that the total energy of the system (conserved within the time t_{sym}) exhibits a jump for $S > 1$, whereby the ensemble at $t > t_{sym}$ does not behave as a conservative system (while the total energy in each particular system is conserved and all these systems behave as conservative). It looks as if the loss of conservatism upon elapse of the period t_{sym} allows the time of retaining the unstable square lattice to be increased by at least one-quarter.

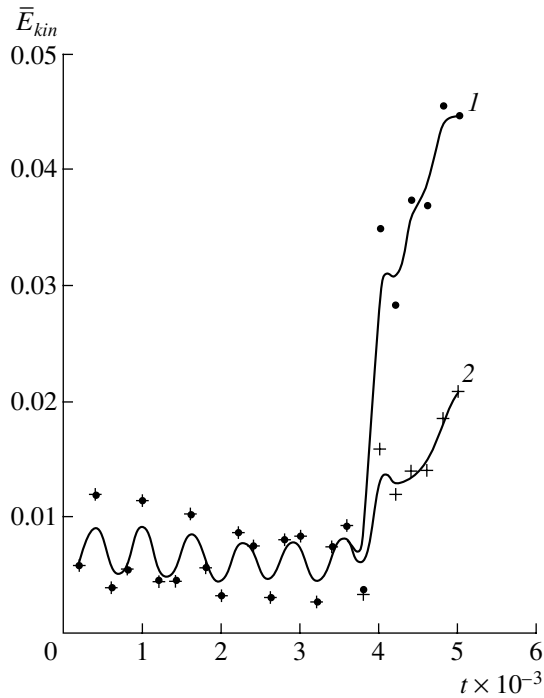Behavior of the total energy E/N is presented in Fig. 3, where curves *1* and *2* correspond to the total

energy for the systems with $S = 1$ and 10, respectively. As can be seen, the total energy of one system is conserved, while that of a system constructed on the ensemble is not conserved. An explanation is found in the superposition of velocities and coordinates of the bodies. Since each system contributes differently to the ensemble upon transition, the total energy should not be conserved. These differences were not manifested before the transition, because the symmetric motion of oscillators with close coordinates leads to almost equal contributions to the total energy E/N.

Figure 4 illustrates the transition for a system with $S = 21$ in the case of $r_1 = 0.5$, $r_j = 0.025$ ($j = 2, 3, \ldots, 21$). As can be seen, the symmetry breaks and the contributions of systems entering into the ensemble with a small weight r_j ($j > 1$) do not lead to the desired result. This problem requires additional investigation.

REFERENCES

1. O. I. Gorskiĭ, V. A. Dzenzerskiĭ, and Yu. P. Kuchugurnyĭ, Pis'ma Zh. Tekh. Fiz. **22** (15), 49 (1996) [Tech. Phys. Lett. **22**, 621 (1996)].

Translated by P. Pozdeev

Fig. 4. Variation of the time-averaged kinetic energy E/N ($N = 16$) for (*1*) a single system and (*2*) a system constructed on an ensemble with $S = 21$ and various r_j ($r_1 = 0.5$, $r_j = 0.025$, $j = 2, \ldots, 21$).

Gas Bubbles in a Hele–Shaw Cell Manipulated by a Light Beam

B. A. Bezuglyĭ and N. A. Ivanova

Tyumen State University, Tyumen, Russia
e-mail: bezuglyi@utmn.ru
Received April 1, 2002

Abstract—The action of a light beam upon a gas bubble in a light-absorbing solution of a tensoactive substance is studied. The light-assisted manipulations, including the partition of large bubbles and the translation of small ones according to the solutocapillary mechanism, are demonstrated for the first time. © *2002 MAIK "Nauka/Interperiodica".*

As is known, a gas bubble occurring in a liquid featuring a temperature gradient ∇T tends to move toward a heated region, even against the buoyancy forces [1]. Called thermocapillary [2], this kind of motion is caused by a difference in the surface tension σ between the opposite poles of the bubble, situated on the axis parallel to the gradient ∇T developed in the liquid. In recent years, the motion of gas bubbles in microscopic channels or cells under the action of a longitudinal gradient ∇T (created by conductive heat supply) has been extensively studied from the standpoint of applications in microfluid devices and microelectromechanical systems [3–5].

The possibility of manipulating gas bubbles with the aid of a light beam was originally demonstrated in [6]. While the light-induced motion of gas bubbles was not the main problem studied in [6], this paper concentrates on detailed investigation of the mechanisms of this effect and develops the methods proposed previously.

The experimental setup represents a modified optical microscope of the MUV-1 type, equipped with a point light source (HBO-100 mercury lamp) and a focusing system. The light beam crossover diameter in the focal plane was $d = 0.60 \pm 0.05$ mm and the total beam power was $P = 200$ mW. The liquid medium with gas bubbles was studied in an assembled optical cell of the Hele–Shaw type mounted on the microscope table.

In order to obtain quantitative data on the gas bubble size, velocity of motion, and the time of partition (for elongated kidney-shaped bubbles) in the digital form, the microscope was equipped with a video camera (25 pictures/s, 560 lines/mm) linked to a computer via a TV tuner (Capture 98 w/VCR).

The Hele–Shaw cell comprised two quartz plates with a 10-μm-thick Teflon spacer, in which a 2×4 cm rectangular channel was cut. With the aid of a pipette, the channel was filled with a liquid medium representing the solution of a light-absorbing, nonvolatile or low-volatile, tensoactive substance (TAS) in a volatile

solvent, for example, a saturated (at 20°C) solution of $CuBr_2$ or I_2 in a 96% ethyl alcohol or acetone. The optical absorption of a 10-μm-thick layer of such solutions is close to 90%. The filled cell was placed between two ring-shaped disks and fastened with screws. As a rule, the solution was distributed in such a way that several gas bubbles of various diameters were retained in the channel. The relative bubble size was characterized by the ratio of its diameter to the light spot diameter, $D/d = D^*$: the bubbles were considered as small for $D^* \leq 1$ and large, for $D^* > 1$.

First, the cell was positioned so that one of the bubbles would fall within the light spot. Subsequently, when the cell was moved in an arbitrary lateral direction,[1] the bubble followed the beam spot so that the front part of its boundary (interface) occurred within the light spot. Exposed to the light beam, the bubble interface features two competitive processes: (i) a decrease in the surface tension due to the light-induced heating and (ii) an increase in the surface tension as a result of solvent evaporation. When the light beam velocity exceeds a certain critical value v^*, for which the evaporation at the interface becomes insignificant, a mechanism of the bubble motion is determined only by the thermocapillary forces. In this case, the interfacial flows entrain the adjacent liquid layers and the negative pressure arising at a stagnation point leads to the development of reverse flows. As a result, two convective vortices appear at the front of the bubble (Fig. 1a). The critical velocity v^* was 0.5–1 mm/s for a $CuBr_2$ solution in ethanol and about 1 cm/s for a I_2 solution in acetone.

Due to the viscous friction, a moving bubble with $D^* \geq 1$ deforms to acquire an oval shape (Fig. 1a). In experiments with the $CuBr_2$ solution in ethanol, such bubbles moving after the light beam at a velocity above

---

[1] In what follows, we will speak of the light beam axis being displaced relative to the cell.
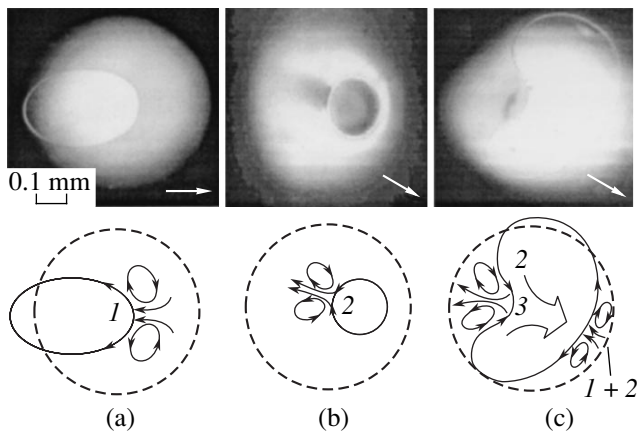
Fig. 1. Thermocapillary (TC) and solutocapillary (SC) mechanisms of gas bubble motion under the action of a light beam (arrows indicate the direction of motion): (a) only TC forces (*1*) are acting upon the bubble in an I_2 solution in acetone; (b) only SC forces (*2*) are acting upon the bubble in a $CuBr_2$ solution in ethanol; (c) both SC and TC forces are acting upon the bubble in an I_2 solution in ethanol (*3* is the vapor flux).
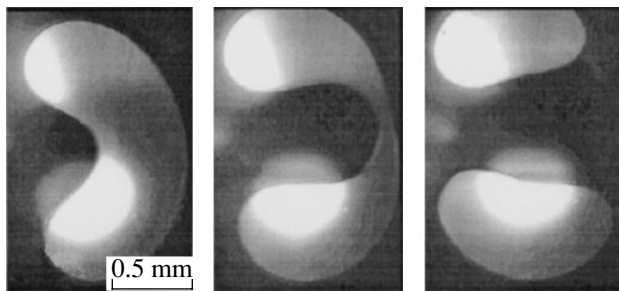

Fig. 2. Sequential photographs illustrating partition of a kidney-shaped gas bubble by the moving light beam in a $CuBr_2$ solution in acetone (time interval between the shots, 0.5 s).

0.7 mm/s were deformed so strongly that the longitudinal to transverse diameter ratio reached up to 5. At the same time, small bubbles remained undeformed.

For $v < v^*$, small bubbles move in front of the light spot. This unusual behavior is explained by the solutocapillary mechanism operative in the exposed zone. This mechanism is related to a growth in the TAS concentration C caused by the solvent evaporation under the condition $\sigma'_C \nabla C > |\sigma'_T| \nabla T$, where σ'_C and σ'_T are the concentration and temperature coefficients of the surface tension σ, respectively. As a result, two correlated capillary vortices are formed near the interface (Fig. 1b), the velocity fields of which are generated by the opposite tangent interfacial stresses directed toward maximum beam intensity. Evidence of the solutocapil-

lary mechanism operation is a clear trace of the increased TAS concentration observed behind the bubble (Fig. 1b). For $D^* = 0.4$, the bubble velocity in the I_2 solution in ethanol reached 0.3 mm/s.

In the case of large bubbles possessing smaller curvature of the surface, the impact pressure $P_i = \rho v_s^2/2$ of the surface solutocapillary flow may exceed the capillary pressure $P_c = \sigma/r$ in the bubble (ρ is the liquid density, v_s is the surface flow velocity at the bubble boundary, and r is the surface curvature). As a result, the interface in the exposed zone bends inward the bubble to form a "cape" and the bubble becomes kidney-shaped (Fig. 1c). The flow at the opposite side of the bubble is caused by condensation of the solvent on a colder part of the interface, which reduces the surface tension in that part both due to dilution of the TAS solution and due to increasing temperature.

As the cape curvature grows, the rate of the solvent evaporation from this surface increases, while convective mixing with the mother solution is hindered by increasing length of the cape. This leads to avalanche growth in the TAS concentration and, hence, in the σ value at the front end of the bubble. Therefore, the growth of the impact pressure of the solutocapillary flow, caused by the TAS concentration gradient, moves the cape forward until it meets the opposite wall, after which the bubble is separated into two parts (Fig. 2).

The above types of the light-assisted manipulation of the gas bubbles can find applications in the development of valveless micropumps [4], microvalves, and thermocapillary optical switches [7].

REFERENCES

1. N. O. Young, J. S. Goldstein, and M. J. Block, J. Fluid Mech. **6** (3), 350 (1959).
2. A. I. Fedosov, Zh. Fiz. Khim. **3** (2), 366 (1956).
3. M. Hasan and R. Balasubramaniam, J. Thermophys. Heat Transfer **3**, 87 (1989).
4. T. K. Jun and C.-J. Kim, J. Appl. Phys. **83** (11), 5658 (1998).
5. A. Mazouchi and G. M. Homsy, Phys. Fluids **12**, 542 (2000).
6. B. A. Bezuglyĭ, Candidate's Dissertation (Mosk. Gos. Univ., Moscow, 1983).
7. M. Sato *et al.*, Hitachi Cable Rev., No. 20, 19 (2001).

Translated by P. Pozdeev

Dynamics of the Electrothermal Instability
of a Polar Dielectric in the Temperature Region
# of Maximum Relaxation Losses

O. A. Emel'yanov

St. Petersburg State Technical University, St. Petersburg, Russia
e-mail: eicc@phtf.stu.neva.ru
Received April 25, 2002

Abstract—Under the action of an electric field, a polar dielectric may occur in several stable temperature states. Transitions between these states can be induced either by temperature perturbations or by changes in the load parameter depending on the frequency and strength of the electric field. A method is proposed for solving the nonlinear electrothermal problem of the temperature transition dynamics. The results of calculations of the temperature dynamics at the center of a dielectric are in good agreement with the data of numerical experiments. © 2002 MAIK "Nauka/Interperiodica".

Previously [1], a model explaining the experimentally observed instability of the thermal state of capacitors based on polar polymer dielectrics was proposed which satisfactorily described this phenomenon in the temperature region of maximum relaxation losses. The exact stationary analytical solutions obtained for the temperature at the capacitor center ϑ_m as a function of the dimensionless load β and the dielectric wall temperature V_0 form a surface of the stationary temperature states with singularities of the "fold" type [1]. However, it is difficult to estimate the dynamics of possible transitions between these states within the framework of the stationary approach. Knowledge of the time variation of temperature at the most heated (usually central) point of a capacitor is very important in the case of devices employed under conditions of large electrothermal loads.

In order to elucidate this question, let us consider in accordance with the model developed previously [1] a cross section of the surface of stationary states $\vartheta_m(\beta, V_0)$ corresponding to $V_0 = -5$ (Fig. 1). For better illustration, the cross section is constructed in the coordinates of $\ln(\vartheta_m - V_0 + 1)$ versus β. The dimensionless parameters are expressed as

$$\beta = \frac{\omega\varepsilon_0\varepsilon''_{max}(Eh)^2}{\lambda}\frac{\beta_d W}{kT_g^2}, \qquad (1)$$

$$V_0 = \frac{T_0 - T_g}{kT_g^2}\beta_d W, \qquad (2)$$

where ω and E are the frequency and strength of the applied electric field; h is the capacitor half-thickness; ε''_{max} is the maximum vale of the loss tangent at $T = T_g$; β_d is the parameter of distribution of the relaxation

times; W is the activation energy; k is the Boltzmann constant, $\varepsilon_0 = 8.85 \times 10^{-12}$ F/m; λ is the thermal conductivity coefficient of the dielectric; and T_0 is the capacitor surface (wall) temperature.

The uncertainty of the $\vartheta_m(\beta)$ value is determined by the wall temperature V_0. For $V_0 \geq 0$, the ambiguity disappears [1]. An analysis of the linearized solutions of the thermal conductivity equation shows that branch 1–2 of the $\vartheta_m(\beta)$ curve is unstable, while branches 2–3 and 0–1 are stable. These conclusions agree with the experimentally observed behavior.

If the capacitor occurs at a dimensionless temperature of the ambient medium (and wall) $V_0 = -5$ prior to switching on load β, application of nominal load β_n will increase the temperature to $\vartheta_n^{(0)}$. Application of load $\beta_1^* > \beta_1$ will induce a transition to the upper stable tem-
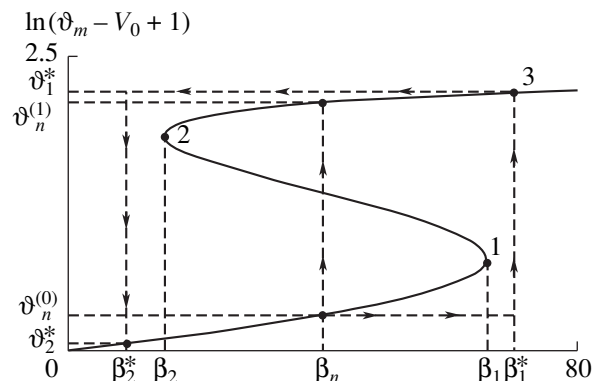

Fig. 1. A stationary temperature state $\vartheta_m = f(\beta)$ at the center of a dielectric. The arrows indicate dynamic transitions induced by changes in the load parameter β.

perature state ϑ_1^*. The transition to the upper branch from point $(\beta_n, \vartheta_n^{(0)})$ can be also induced by a temperature perturbation at the capacitor center (lasting for a sufficiently long time). The perturbation amplitude must be $\Delta\vartheta > \vartheta_n^{(1)} - \vartheta_n^{(0)}$. The reverse transitions $\vartheta_n^{(1)} \longrightarrow \vartheta_n^{(0)}$ and $(\beta_1^*, \vartheta_1^*) \longrightarrow (\beta_2^*, \vartheta_2^*)$ take place at $\Delta\vartheta < -(\vartheta_n^{(1)} - \vartheta_n^{(0)})$ or $\beta_2^* < \beta_2$.

Characteristic times of the above transitions can be estimated from the following considerations. The initial model reduces to a boundary problem of the first kind with a heat source described by the function $q(u)$:

$$\begin{bmatrix} \dfrac{\partial^2 u}{\partial x^2} + \beta q(u) = \dfrac{\partial u}{\partial \tau}, \\ u|_{\pm 1} = V_0, \\ u(0, x) = V_0, \end{bmatrix} \tag{3}$$

where $q(u) = e^{-|u|}(2 - e^{-|u|})$, $\tau = (\lambda/\rho C_p)t$ is the dimensionless time, and ρ and C_p are the dielectric density and heat capacity, respectively.

Let u_0 and λ_0 be the first eigenfunction and eigenvalue of the stationary Sturm–Liouville problem corresponding to Eqs. (3). Introducing the integral transformation of averaging over space Ω (i.e., over dielectric thickness) [2],

$$\overline{U}(\tau) = L(u) = \frac{1}{mes\,\Omega} \int_{mes\,\Omega} V_0(x)u(x, t)dx \tag{4}$$

(where $x \in R^n$ and $u \in C_{t,x}^{1,2}$), we reduce the problem (3) to a differential equation of the first order with respect to a certain average temperature $\overline{U}$,

$$\frac{d\overline{U}(\tau)}{d\tau} = \beta\overline{q(U(\tau))} - \lambda_0(\overline{U}(\tau) - V_0), \tag{5}$$

with the corresponding boundary and initial conditions:

$$\overline{U}(t)|_{\pm 1} = V_0, \quad \overline{U}_0(0) = \overline{U_0(x)}. \tag{6}$$

It can be shown that relation $\overline{q(U)} = q(\overline{U})$ is exactly satisfied for a linear heat source $q(u)$. The more significant the nonlinearity of the source, the greater the error of a solution to Eq. (5) obtained with an allowance for the condition $\overline{q(U)} = q(\overline{U})$. To minimize the error, we may consider a stationary problem for amplitude U_m

of the temperature profile. In this case, the load parameter $\beta = \beta(U_m)$ is

$$\beta(U_m) = \frac{1}{2}\left[\int_{V_0}^{U_m} \frac{d\vartheta}{\sqrt{\int_\vartheta^{U_m} q(y)dy}}\right]^2. \tag{7}$$

Based on the above considerations, we determine $\overline{q(U_m)} = \lambda_0(U_m - V_0)/\beta(U_m)$. Then, the dynamics of $U_m(t)$ can be evaluated using the following integral relationship:

$$\tau \approx \int_{\overline{U}_0}^{U_m(\tau)} \frac{dU_m}{\left[\dfrac{\beta}{\beta(U_m)} - 1\right](U_m - V_0)\lambda_0}. \tag{8}$$

Thus, the nonlinear nonstationary problem with respect to $u(x, \tau)$ is reduced to problem (8) for $U_m(\tau)$.

Now we will consider some results of solving Eq. (8) for estimating the characteristic times of transitions illustrated in Fig. 1. For the transitions along branch 0–1, we obtain an estimate for τ by expanding into series in ϑ_m and restricting the analysis to terms of the second order:

$$\begin{bmatrix} \tau(\vartheta_m) = \tau_1(\vartheta_m) + \tau_2(\vartheta_m) \\ \tau_1(\vartheta_m) = \dfrac{1}{\lambda_0}\ln\dfrac{\vartheta_n^{(0)} - V_0}{\vartheta_n^{(0)} - \vartheta_m(\tau)} \\ \tau_2(\vartheta_m) = \dfrac{1}{2\lambda_0}\ln\dfrac{\vartheta_n^{(0)} - V_0}{(\vartheta_1 - \vartheta_n^{(0)})} \\ \times \ln\left[\dfrac{(\vartheta_n^{(0)} - V_0)}{\vartheta_n^{(0)} - \vartheta_m(\tau)}\dfrac{2(\vartheta_1 - \vartheta_n^{(0)}) + (\vartheta_n^{(0)} - \vartheta_m(\tau))}{2(\vartheta_1 - \vartheta_n^{(0)}) + (\vartheta_n^{(0)} - V_0)}\right] \end{bmatrix}. \tag{9}$$

As can be seen, the characteristic transition time is a nonlinear function of two supercritical parameters, $\vartheta_n^{(0)} - V_0$ and $\vartheta_1 - \vartheta_n^{(0)}$. Assuming that the transition terminates at a temperature ϑ^* such that

$$\gamma \approx \frac{\vartheta_{st} - \vartheta^*}{\vartheta_{st} - V_0} = 0.01 \tag{10}$$

(where ϑ_{st} is the established stationary temperature), we obtain for the limiting transition $0 \longrightarrow 1$, $\beta = \beta_1$, $\vartheta_1 = \vartheta_N^{(0)}$. Eliminating the uncertainty in (9), we arrive at

$$\tau_{0 \rightarrow 1} \approx \frac{1}{\lambda_0}\left[\ln\frac{1}{\gamma} + \frac{1}{\gamma}\right], \quad \gamma \ll 1. \tag{11}$$

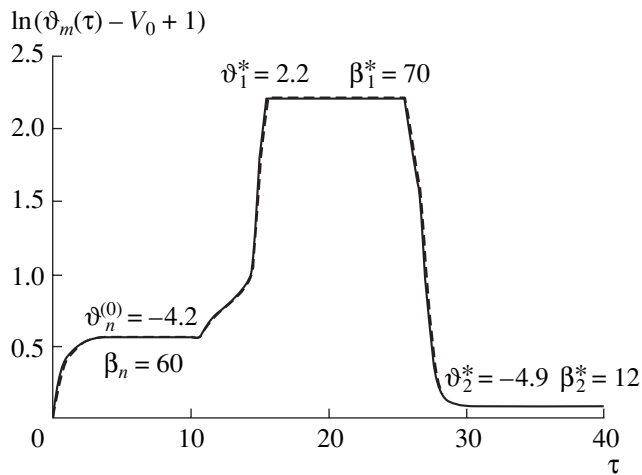$\ln(\vartheta_m(\tau) - V_0 + 1)$

Fig. 2. Dynamics of the temperature transitions in a dielectric. Figures indicate the ϑ and β values of the corresponding stationary states. Solid and dashed curves refer to the proposed theory and the results of numerical experiments, respectively.

The parameters of other transitions are estimated in an analogous manner using the same approach.

Figure 2 shows the plots of solutions $\vartheta_m(\tau)$ for the transitions described according to the proposed averaging method for $u(x, \tau)$ in Eqs. (4)–(8). These data are compared to the results of numerical solution of the nonlinear thermal conductivity equation (3) performed on a computer using an implicit difference scheme [3]. The curves depicted in Fig. 2 show a good agreement between a solution obtained using the proposed method of averaging the nonlinear problem for the maximum temperature (at the center of the capacitor) and the data of numerical experiments.

In concluding, it should be noted that the method proposed for estimating the temperature dynamics is applicable to the capacitors of rectangular and cylindrical shapes.

REFERENCES

1. O. A. Emel'yanov, Pis'ma Zh. Tekh. Fiz. **27** (16), 32 (2001) [Tech. Phys. Lett. **27**, 679 (2001)].
2. A. I. Vol'pert and S. I. Khudyaev, *Analysis in the Classes of Discontinuous Functions and Equations of Mathematical Physics* (Nauka, Moscow, 1975).
3. A. A. Samarskiĭ, V. A. Galaktionov, V. A. Kurdyumov, and A. P. Mikhaĭlov, *Sharpening Regimes in Problems for Quasilinear Parabolic Equations* (Nauka, Moscow, 1987).

Translated by P. Pozdeev

An Anomalous Acoustic Effect during Martensite Transformations in NiTi-Based Alloys

V. A. Plotnikov and D. V. Kokhanenko

Altai State University, Barnaul, Russia
e-mail: plotnikov@phys.dcn-asu.ru
Received March 29, 2002; in final form, May 20, 2002

Abstract—Martensite transformations proceeding in mechanically loaded TiNi-based alloys account for an "anomalous" character of the acoustic emission from the material, whereby cyclic transformations during the growth of mechanical stress in the course of the direct transition is accompanied by an increase, rather than by a decrease, in the acoustic emission energy. This behavior of the acoustic emission is evidence of a significant influence of the external stresses on the martensite transformations and the related energy dissipation process. © 2002 MAIK "Nauka/Interperiodica".

Introduction. As is known, NiTi-based alloys subjected to thermal cycling in a temperature interval containing the temperatures of thermoelastic martensite transformations (MTs) $B2 \longrightarrow B19$, $B2 \longrightarrow B19'$, and $B2 \longrightarrow R \longrightarrow B19'$ exhibit a characteristic acoustic emission. A typical feature of this emission is the significant asymmetry of the acoustic energy produced during the direct and reverse MTs [1]. There are two types of asymmetry: the first, whereby the energy of emission during the direct MT ($B2 \longrightarrow B19'$) is significantly greater than that during the reverse process, and the second, for which the emission energy during the reverse MT ($B19' \longrightarrow B2$) is greater than that during the direct process.

In the course of multiply repeated cyclic MTs, the character of the asymmetry changes from the first to second type (inversion). The inversion is also observed upon increasing the nickel content in the binary alloy. This behavior of the acoustic emission is related to structural features of the B2 phase, which significantly influence the mechanical properties of alloys and the kinetics and order of MTs [1]. Assuming that external mechanical stresses, as well as temperature, is a parameter of state of the system, we have experimentally studied the effect of static loading on the MTs and acoustic emission in NiTi-based alloys.

Experimental. The experiments consisted in inducing cyclic MTs in the samples loaded according to three variants, with simultaneous detection of the acoustic emission. In the first variant, MT cycles were multiply repeated at a zero applied load; in the second variant, the cycles were conducted under symmetric loading (in both direct and reverse MTs) with increasing applied stress; and in the third variant, the loading with increased applied stress was asymmetric (in the direct MT). In all experiments, the samples (plates with a length of 40 mm, a width of 4 mm, and a thickness of about 1 mm) were strained by bending in a cantilever geometry.

Results. Figure 1 shows fragments of the acoustic emission curves (rms response voltage versus time) together with the patterns of the sample temperature variation with the time. The shapes of the acoustic curves are indicative of a significantly asymmetric acoustic energy dissipation during the MT cycle: the energy of emission produced during the direct transition exceeds that observed for the reverse transition. The experiments with symmetric loading show an increase (to a certain saturation level) in the emission energy for the reverse MT; however, this energy is still lower than that for the direct MT.

Figure 2 shows variation of the emission energy with the cycle number. As can be seen from these data, repeating MT cycles lead to a decrease in the acoustic emission energy (to a certain saturation level) in the direct transition, while leaving the emission energy unchanged during the reverse transition. The MT cycling under symmetric static load does not change the character of acoustic emission (Fig. 2b): the energy decreases with increasing MT cycle number in the same manner as it does in the case of cycling under zero load.

Loading in the asymmetric mode (Fig. 2c) leads to an "anomalous" monotonic growth of the emission energy up to a certain level significantly (by several orders of magnitude) exceeding the saturation level observed in the cycles with zero or symmetric loading. In the reverse transitions, the energy remains unchanged.

Discussion of results. If the acoustic emission during the direct MT is caused by the plastic relaxation of microscopic stresses, it can be suggested that a decrease in the energy emitted in the initial cycles of direct MTs is related to degradation of the plastic defor-
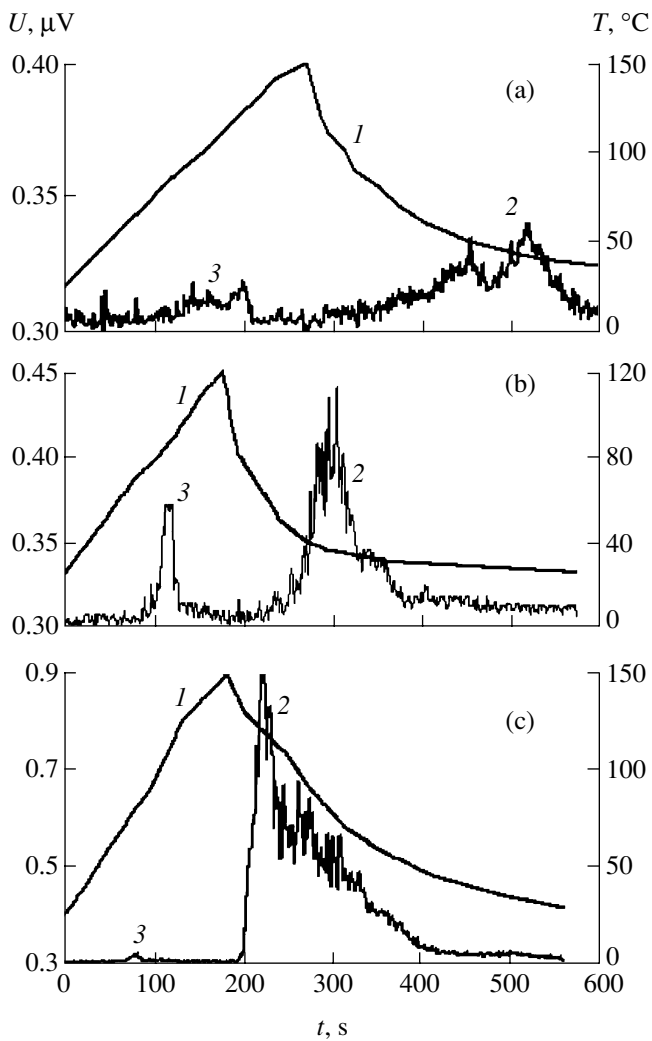
Fig. 1. Kinetics of the acoustic effect in the course of cyclic martensite transformations (B2 ⟶ B19' and B19' ⟶ B2) in a TiNi(Mo) alloy under (a) zero applied stress, (b) symmetric loading, and (c) asymmetric loading (B2 ⟶ B19' under load and B19' ⟶ B2 upon unloading): (*1*) temperature variation; (*2*) acoustic response during the direct transition; (*3*) acoustic response during the reverse transition.

Fig. 2. Variation of the acoustic response of a TiNi-based alloy in the course of repeated B2 ⟶ B19' martensite transformations showing (a) a significant decrease in the energy of emission with increasing number *n* of MT cycles under zero load, (b) a drop in the emission energy with gradually increasing external stress σ under symmetric loading conditions, and (c) "anomalous" growth in the emission energy for the asymmetric loading: (*1*) acoustic response during the direct transition; (*2*) acoustic response during the reverse transition.

mation. The plastic strain relaxation (or local plastic deformation) consists in generating pure dislocations at the interface. These dislocations are inherited during the MT cycle, which results in their accumulation leading to the alloy hardening [2]. However, the susceptibility of an alloy to the plastic relaxation of microstresses depends on a relationship between the martensite shear stress and the yield stress. The higher the martensite shear stress and the lower the yield stress (i.e., the smaller the difference between these stresses), the higher the probability that the microstresses localized at the martensite boundaries would attain the yield stress level and the plastic relaxation would take place.

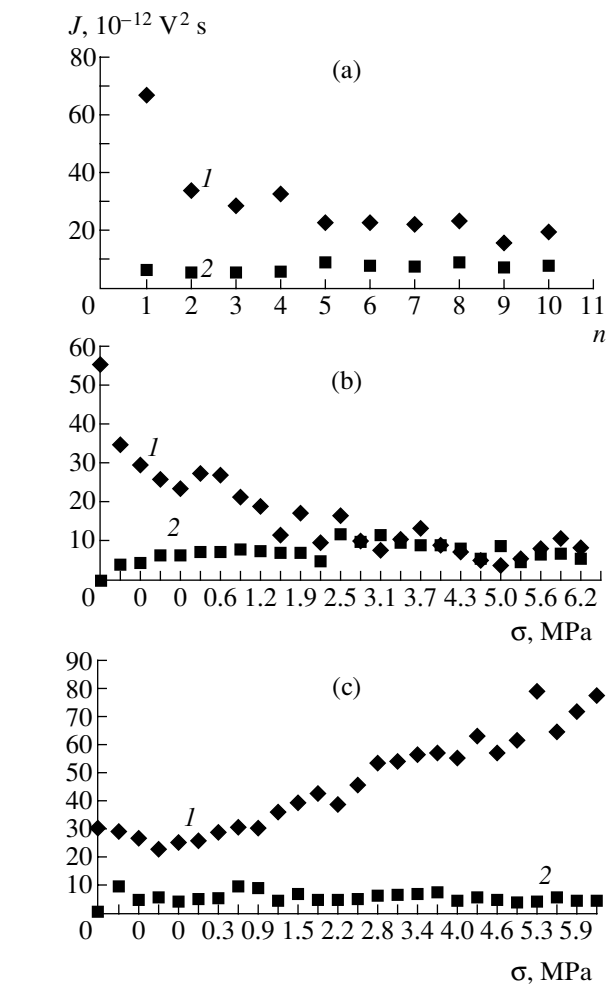According to [3], the martensite shear stress in TiNi(Mo) alloys amounts to 5–20 MPa, while the yield

stress is close to 1000 MPa. Therefore, the difference between these stresses is large and the probability that microstresses would reach the yield stress level is small (close to zero).

When the saturation level is attained, the residual acoustic emission during the direct MT (and the more so, during the reverse MT) can no longer be related to the plastic relaxation of microstresses. Evidently, the "anomalous" growth of the acoustic emission energy observed in the MT cycles under application of the external load possesses a dynamic nature and is indicative of a change in the MT kinetics.

Indeed, some researchers pointed out that accumulation of the martensite deformation and its relaxation upon unloading are spontaneous processes [4, 5]. This

is evidence of the martensite transformation kinetics changing under external stress conditions, acquiring a macroscopic explosion character [6]. Another example is offered by single crystal samples of a Cu–14.2% Al–4.3% Ni alloy [7], where the process of nucleation of the martensite crystals in the course of deformation resembled propagation of the Lüders band; it was even more so for the initial phase nucleation upon unloading.

Conclusion. The above experimental data and their analysis indicate that a dynamic mechanism of the anomalous acoustic effect observed during cyclic MTs under applied static load is related to a significant extent to the correlated formation of martensite crystals over a macroscopic volume. This inference coincides with our previous conclusions drawn from the study [8] of an anomalous acoustic emission during violation of the complete cycle of MTs. The greater the correlation (in a broad sense, coherency) of the events of spontaneous displacement in the system of martensite grains, the higher the energy of acoustic emission accompanying the dynamic relaxation process. When the martensite shear stress is close to the yield stress, the stresses generated at the interphase boundary can, together with the applied load, lead to a local plastic strain relaxation of the elastic energy in the course of the direct MT. In this case, the "anomalous" acoustic effect is caused by the action of two factors: the local plastic strain relaxation and the dynamic energy relaxation.

REFERENCES

1. V. A. Plotnikov, Fiz. Met. Metalloved. **88** (4), 91 (1999).

2. V. A. Plotnikov, L. A. Monasevich, and Yu. I. Paskal', Fiz. Met. Metalloved. **61** (4), 769 (1986).

3. V. É. Gyunter, V. I. Itin, L. A. Monasevich, *et al.*, *Shape Memory Effects and Their Application in Medicine* (Nauka, Novosibirsk, 1992).

4. A. A. Klopotov, V. A. Polyanskiĭ, and V. É. Gyunter, *Evolution of Defect Structures in Condensed Media* (Barnaul, 1996), p. 2.

5. S. L. Kuz'min, V. A. Likhachev, S. R. Shimanskiĭ, and A. I. Chernyshenko, Fiz. Met. Metalloved. **57** (3), 612 (1984).

6. K. Shimizu and K. Otsuka, in *Shape Memory Effect in Alloys: Proceedings of the International Symposium on Shape Memory Effects and Applications, Toronto, 1975,* Ed. by J. Perkins (Plenum, New York, 1975; Metallurgiya, Moscow, 1979).

7. L. A. Shepard, in *Shape Memory Effect in Alloys: Proceedings of the International Symposium on Shape Memory Effects and Applications, Toronto, 1975*, Ed. by J. Perkins (Plenum, New York, 1975; Metallurgiya, Moscow, 1979).

8. V. A. Plotnikov, Pis'ma Zh. Tekh. Fiz. **24** (1), 31 (1998) [Tech. Phys. Lett. **24**, 14 (1998)].

Translated by P. Pozdeev

On the Spectral Resolution of a Focusing Bragg Spectrometer

T. Tchen

Moscow State Academy of Fine Chemical Technology, Moscow, Russia
e-mail: docent65@mtu-net.ru; ttchen@e-mail.ru
Received April 12, 2002

Abstract—The influence of the intensity profile of a wave, focused upon backscattering from a bent crystal, on the spectral resolution of a focusing Bragg spectrometer dynamically reflecting short-wavelength X-ray radiation ($\lambda \sim 1$ Å) is considered in comparison to a nonfocusing flat-crystal spectrometer. Conditions necessary for resolving spectral lines in the spectrometers of both types are formulated. © *2002 MAIK "Nauka/Interperiodica".*

In recent years, bent crystals have been widely used in X-ray spectrometers [1–10]. This paper is devoted to theoretical analysis of the influence of the diffracted wave intensity profile on the spectral resolution of a focusing bent-crystal spectrometer.

Let us consider diffraction of a wave on a bent crystal, with the bending radius R_x in the plane of scattering satisfying the "weak" bending condition (in terms of [11]):

$$R_x \gg \kappa \Lambda^2 \left| (1 - \gamma_0^2)/\gamma_0 - (1 - \gamma_h^2)/\gamma_h \right| /(4\pi^2).$$

Then, the plane wave amplitude reflection coefficient can be approximately described by an expression for the corresponding coefficient of a flat (unbent) crystal. According to [11, 12], the diffracted wave amplitude at a point ξ_p in vacuum is

$$E_h(\xi_p) \sim \int_{-\infty}^{+\infty} dk\, G_h(k + q_0) \tag{1}$$
$$\times \exp[-ik^2(1/\alpha_0 + 1/\alpha_h)/2\kappa + ik\gamma_h\xi_p/\alpha_h L_h],$$

where $G_h(k + q_0)$ is the Fourier component of the Green function for the diffracted wave; $\alpha_0 = \gamma_0^2/L_0 - \gamma_0/R_x$ and $\alpha_h = \gamma_h^2/L_h - \gamma_h/R_x$, $\gamma_{0,h}$ are the direction cosines of the incident and diffracted waves; L_0 and L_h are the distances from the point source of the spherical wave to the crystal and from the crystal to the source image; and $\kappa = 2\pi/\lambda$, λ being the incident radiation wavelength (explicit expression for q_0 can be found in [11]). Equation (1) was obtained for a parabolic expansion of the incident spherical wave phase

$$G_h(k + q_0) = 2i/(k + q_0 + \{(k + q_0)^2 - \pi^2/a^2\Lambda^2\}^{1/2}),$$

where $a = \sin(\varphi_0 - \varphi_h)/(2\gamma_0|\gamma_h|)$; φ_0 is the angle between the incident wave and the normal to the crystal surface;

φ_h is the angle between the diffracted wave and the normal; $\Lambda = \lambda(\gamma_0|\gamma_h|)^{1/2}/C|\chi_h\chi_{-h}|^{1/2}$ is the extinction length; χ_h and χ_{-h} are the Fourier components of the X-ray polarizability; and C is the polarization factor.

As can be readily seen, for $\alpha_h = -\alpha_0$ the integral in expression (1) can be analytically exactly calculated because the wave intensity reduces to the Bessel function of the first kind $J_1(t_\xi)$,

$$I_h(\xi_p) \sim |J_1(t_\xi)/t_\xi|^2 \Theta(t_\xi), \tag{2}$$

where $t_\xi = 2\xi_p\gamma_h\sigma_h/\alpha_h L_h$, $\sigma_h = \kappa\chi_h/4\cos\theta_B$, and $\Theta(t_\xi)$ is the Heaviside function.

Gabrielyan *et al.* [11, 13] showed that the wave from a source situated on the Rowland circle ($L_0 = R_x\gamma_0$) is focused according to the Johann scheme. In this case, the wave intensity near the point source image is distributed by the law

$$I_{h,\text{Johann}}(\xi_p) \sim |\sin(t_\xi)/t_\xi|^2, \quad t_\xi = \kappa x_{\text{eff}}\xi_p/2R_x, \tag{3}$$

where x_{eff} is the effective diffraction length [11, 13].

According to [11, 13], a theoretical limit for the spectral resolution of a Johann spectrometer is $d\lambda/\lambda \sim 10^{-8}$. Evidently, the spectral resolution is determined by the linear dispersion $D_\xi = d\xi_p/d\lambda$ and by the wave intensity profile.

The estimate of the spectral resolution obtained in [11, 13] corresponds to the spatial resolution equal to the diffraction broadening $\Delta\xi_p$ of the point source image. The value of $\Delta\xi_p$ is obtained from relation (3) by putting $t_\xi = \pi$, so that the main intensity maximum for the spectral line $\lambda + d\lambda$ would correspond to the first intensity zero for the line λ. The total intensity from the two spectral lines exhibits a 19% dip at $t_\xi = \pi/2$. By analogy with the well-known Rayleigh criterion in optics, we may consider the condition $t_\xi = \pi$ as a crite-

rion for the resolution of spectral lines in the Johann spectrometer.

In the case when the source is not situated on the Rowland circle, let us also adopt that the lines λ and $\lambda + d\lambda$ are considered as resolved if the main intensity maximum for the spectral line $\lambda + d\lambda$ coincides with the first zero ($t_0 \cong 3.85$) of the Bessel function $J_1(t_\xi)$ (Fig. 1). An analysis shows that the intensity dip between the two lines amounts to 28%, so that the lines are actually resolved. Note that, for $L_0 \neq R_x\gamma_0$, the condition $t_\xi = \pi$ is no longer sufficient for reliably resolving the lines: the total intensity at $t_\xi = \pi/2$ is virtually equal to the maximum intensity of both lines. It should be also noted that the expansion into the spectrum takes place due to the effect of focusing in the observation plane at a distance L_h from the crystal.

Now let us consider a defocusing spectrometer based on a flat crystal. In this case, $\alpha_h \neq \alpha_0$ and expression (1) will be analyzed by the stationary phase method. Consider a stationary point $k_{stat} = -\kappa\xi_p/\{\gamma_h(1/\alpha_0 + 1/\alpha_h)\}$. The spatial distribution of intensity is determined by the square modulus of the corresponding Green function, $|G_h(k_{stat} + q_0)|^2$. By reducing the argument of this function to a usual angular variable y, we can represent the function in a form convenient for practical calculations, $|y - (y^2 - 1)^{1/2}|^2$. For a symmetric geometry of the diffraction of a σ-polarized wave, we employ $y = (\Delta\theta\sin\theta_B + \chi_0)/(\chi_h\chi_{-h})^{1/2}$, where $\Delta\theta = \theta - \theta_B$ is the deviation from the exact Bragg angle θ_B. In the absence of focusing, only one partial ray reflected from the flat crystal reaches each point ξ_p and the coordinate ξ_p is uniquely determined by $\Delta\theta$. In contrast to the case of a bent-crystal (focusing) spectrometer, the spectrum in a flat-crystal spectrometer is usually observed near the crystal. It is evident that the presence of the region of total reflection (represented by a "flat" portion of the profile in Fig. 2) deteriorates the spectral characteristics of a flat-crystal spectrometer as compared to those of a focusing instrument.

Let the distance between the right-hand edge of the reflection curve for the line λ ($y = 1$) and the left-hand edge of the analogous curve for the line $\lambda + d\lambda$ be δy. We require that the intensity dip between the lines would be not less than 20%. Then, assuming $\delta y \ll 1$, we arrive at the inequality

$$1 + \delta y/2 - (\delta y)^{1/2} \leq (0.4)^{1/2}. \quad (4)$$

Solving this inequality with an allowance for $\delta y \ll 1$, we obtain

$$\delta y \geq [1 - \{1 - 2(1 - (0.4)^{1/2})\}] \approx 0.735, \quad (5)$$

from which it follows that $\delta(\Delta\theta) \geq |\chi_{hr}|(2 + \delta y)/\sin 2\theta_B$.

Using the Bragg law, we obtain an estimate for the spectral resolution for the flat-crystal spectrometer:

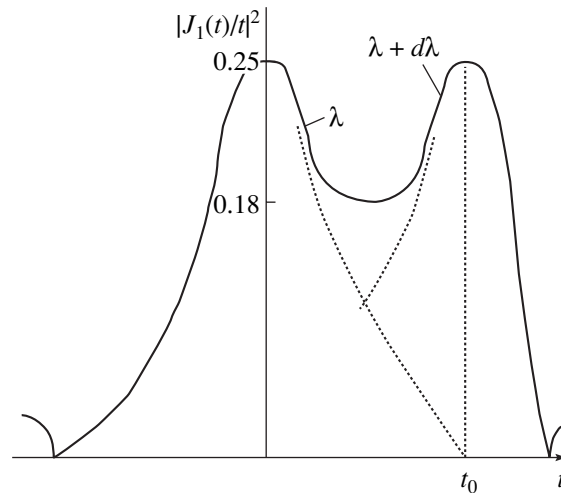$$d\lambda/\lambda \geq \cot\theta_B\delta(\Delta\theta). \quad (6)$$

Fig. 1. Diffracted wave intensity distribution near the point source image for two spectral lines, $\lambda + d\lambda$ and λ, for a cylindrically bent crystal ($L_0 \neq R_x\gamma_0$).
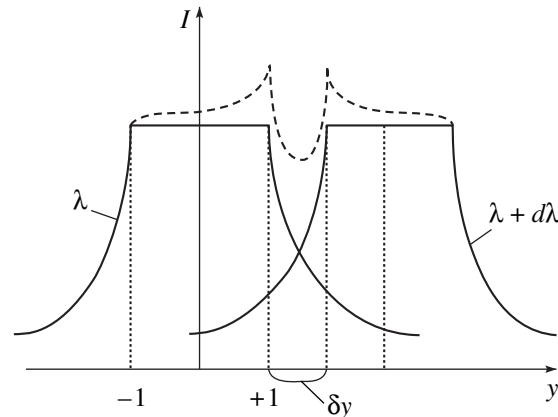

Fig. 2. Angular profile $I(y)$ of the diffracted wave intensity distribution for two spectral lines, $\lambda + d\lambda$ and λ, for a spherical wave incident on a flat crystal.

For the (220) reflection of CuK_α radiation from a silicon crystal, this yields $d\lambda/\lambda \geq 7.7 \times 10^{-5}$. This resolution is 2–3 orders of magnitude lower as compared to that of a focusing bent-crystal spectrometer.

It should be noted that the modern level of development of measuring instrumentation allows distinguishing of line intensities differing by less than 20%, which somewhat improves theoretical estimates of the spectral resolution obtained in this study.

REFERENCES

1. G. Hölzer, O. Wehrhan, J. Heinish, *et al.*, Phys. Scr. **57**, 301 (1998).

2. G. Hölzer, O. Wehrhan, and E. Förster, Cryst. Res. Technol. **33**, 555 (1998).

3. O. Renner, T. Mivalla, P. Sondhauß, *et al.*, Rev. Sci. Instrum. **68**, 2393 (1997).

4. K. Hamalainen, M. Krish, C. C. Kao, *et al.*, Rev. Sci. Instrum. **66**, 1525 (1995).

5. U. Lehnert and G. Zschornack, J. X-ray Sci. Technol. **6**, 83 (1996).

6. B. S. Fraenkel, M. Bitter, S. von Goeler, and K. Hill, J. X-ray Sci. Technol. **8**, 171 (1998).

7. G. Hölzer, E. Förster, M. Grätz, *et al.*, J. X-ray Sci. Technol. **8**, 50 (1998).

8. V. A. Bryzgunov, Zh. Tekh. Fiz. **70** (1), 49 (2000) [Tech. Phys. **45**, 46 (2000)].

9. E. M. Latush and M. I. Mazuritskiĭ, Pis'ma Zh. Tekh. Fiz. **28** (1), 49 (2002) [Tech. Phys. Lett. **28**, 21 (2002)].

10. E. M. Latush and M. I. Mazuritskiĭ, Pis'ma Zh. Tekh. Fiz. **28** (4), 35 (2002) [Tech. Phys. Lett. **28**, 142 (2002)].

11. K. T. Gabrielyan, F. N. Chukhovskiĭ, and D. I. Piskunov, Zh. Éksp. Teor. Fiz. **96** (3), 834 (1989) [Sov. Phys. JETP **69**, 474 (1989)].

12. T. Tchen, Zh. Tekh. Fiz. **72** (7), 92 (2002) [Tech. Phys. **47**, 886 (2002)].

13. K. T. Gabrielyan, F. N. Chukhovskiĭ, and Z. G. Pinsker, Zh. Tekh. Fiz. **50** (8), 1641 (1980) [Sov. Phys. Tech. Phys. **25**, 956 (1980)].

Translated by P. Pozdeev

Reflex Triode with Virtual Cathode and Controlled Internal TEM-Waveguide Feedback

A. E. Dubinov, I. V. Konovalov, I. V. Rozhnov, V. D. Selemir, A. V. Tikhonov, and K. V. Shibalko

Institute of Experimental Physics, Russian Federal Nuclear Center, Sarov, Russia
e-mail: dubinov@ntc.vniief.ru
Received April 12, 2002

Abstract—A reflex triode with virtual cathode (VC) was studied in which a controlled-length TEM-waveguide feedback was introduced between the region of generation (VC localization) and a diode region. At a certain feedback length, the microwave output power of the reflex triode increases by a factor of 1.6 as compared to the same system without feedback. © *2002 MAIK "Nauka/Interperiodica".*

Microwave oscillators with virtual cathodes (VCs) constitute one of the main classes of oscillators for high-power relativistic electronics. This class includes vircators and reflex triodes, the latter providing for the maximum microwave generation efficiency achieved in practice. Advances in the development and investigation of reflex triodes with VCs were reviewed in [1, 2].

In recent years, there has been a definite trend in the development of microwave generators with VCs, whereby maximum efficiency in the generation of stimulated radiation is achieved by creating a positive feedback between the region of generation (where the VC is localized) and a diode region. There are various methods for creating a waveguide feedback in vircators (see, e.g., [3, 4]) which significantly increase both the efficiency and controllability of these oscillators. In the context of this study, it is necessary to mention a vircator [5, 6] in which the feedback is mediated by a dispersionless TEM wave.

To our knowledge, no investigations of the effect of feedback in the reflex triodes with VCs have been reported until now. Below, we consider the results of experimental investigation of a reflex triode with VC into which a positive TEM-waveguide feedback was introduced as proposed in [7].

The experiments were performed on a setup representing a power supply system loaded on a reflex triode. The power supply system consisted of a pulsed current generator (PCG), an electric-explosion converter (EEC), and a gas-filled uncontrolled discharge gap (DG) with the following characteristics. For PCG: stored energy, 42 kJ; voltage, up to 100 kV; short-circuit current, up to 500 kA; intrinsic inductance, 150 nH; and electric capacitance (in a pulse), 8 μF. For EEC: initial resistance 18 mΩ; break current, 220–240 kA; and open-circuit voltage, 550 kV. For DG: working gas

mixture, 60% N_2 + 40% SF_6; pressure, up to 5 atm; and breakdown voltage, 350–450 kV. The power supply system delivered pulses of 450–500 kV voltage and 20–300 kA current with a leading front duration of 30 ns and a total pulse width of 100–150 ns.

Figure 1 shows a schematic diagram of the reflex triode. This comprised an all-metal vacuum cylindrical chamber with a diameter of 720 mm and a length of 420 mm. One end of the cylinder represented an insulating window through which microwave radiation was extracted, while the opposite edge was closed with a high-voltage insulator. An explosion-emission graphite cathode with a diameter of 90 mm and a variable length of 335–360 mm was mounted inside the chamber perpendicularly to its axis. A metal grid anode with a geometric transparency of 70% was fastened in an anode holder with a feedthrough mounted on the edge insulator. The anode holder also bore a hollow cylinder with
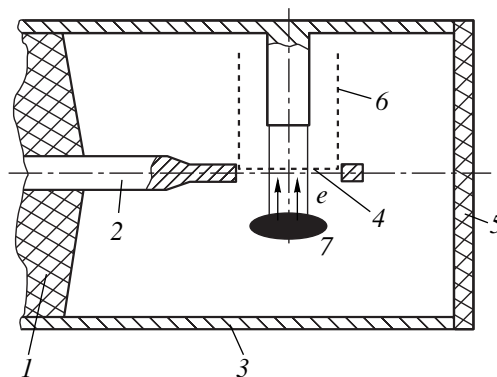

Fig. 1. Schematic diagram of a reflex triode with controlled-length TEM-waveguide feedback: (*1*) insulator; (*2*) anode holder; (*3*) vacuum chamber; (*4*) anode grid; (*5*) microwave radiation output window; (*6*) TEM-waveguide feedback channel; (*7*) virtual cathode.
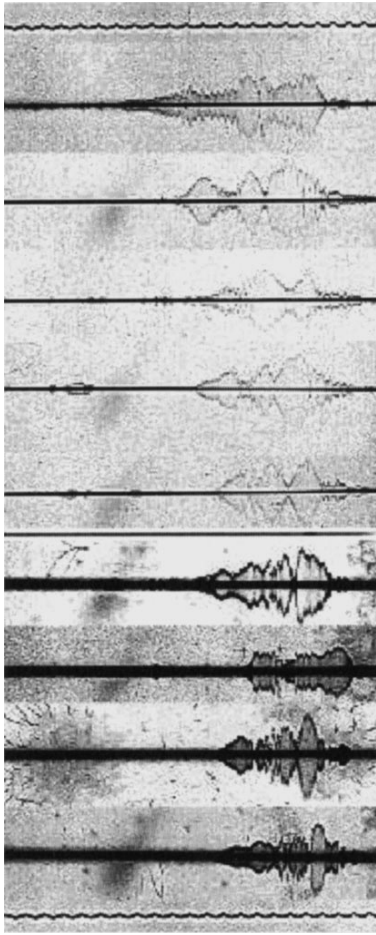
Fig. 2. Typical oscillograms of the detector signals measured for the reflex triode without feedback (uppermost curve) and with the feedback varied by increasing the anode cylinder length starting from 90 mm in 10-mm steps.
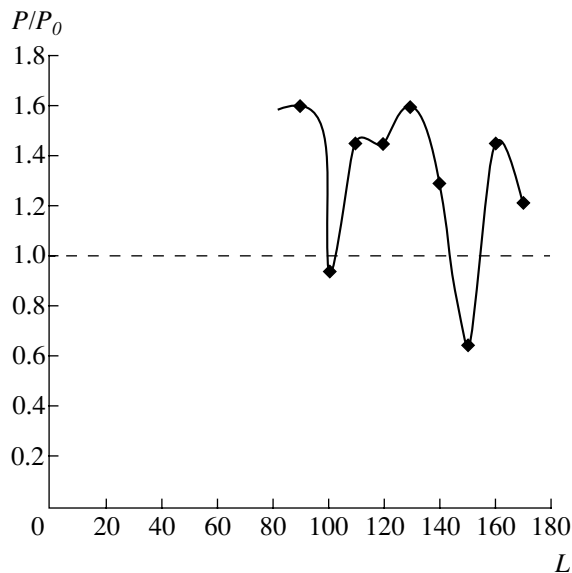

Fig. 3. A plot of the microwave power versus anode cylinder length for a reflex triode with VC. The power is normalized to that of a triode without feedback (corresponding to the unity level indicated by the dashed line).

a diameter of 150 mm, surrounding the cathode to form a coaxial feedback line with a wave impedance of 30.6 Ω. The cylinder had a telescopic design which allowed its length to be mechanically varied from 90 to 156 mm, thus controlling the feedback.

The output microwave radiation power was measured with 6D13D type detectors positioned at a distance of 5.5 m from the radiation extraction window of the reflex triode. The microwave spectrum was measured using a wideband antenna of the P6-23A type coupled, via a feeder tract, to an SRG-7 digital registrator possessing a transmission band with a boundary at 5 GHz. The antenna was mounted at a distance of 1.5 m from the output window of the reflex triode.

Here, we present the data obtained for the reflex triode with a cathode–anode spacing of 21 mm, in microwave radiation spectrum falls within the 2–3.5 GHz range. In the absence of an anode cylinder forming the feedback, the microwave radiation power was estimated at 100 MW. Figure 2 shows the oscillograms of signals measured without and with the feedback for an anode cylinder length varied in 10-mm steps under otherwise equal conditions of operation of the high-voltage reflex triode.

Figure 3 shows a plot of the normalized microwave power versus length of the coaxial (feedback) line, constructed by processing the above oscillograms at the signal maximum and taking into account that the radiation power is proportional to the square of the wave amplitude. As can be seen from Fig. 3, a certain feedback length allows the output power of the reflex triode to be increased by a factor of 1.6 as compared to the same triode without feedback.

REFERENCES

1. A. N. Didenko, V. P. Grigor'ev, and A. G. Zherlitsyn, *Plasma Electronics* (Naukova Dumka, Kiev, 1989), p. 112.

2. A. E. Dubinov and V. D. Selemir, Zarubezhn. Radioélektron., No. 4, 54 (1995).

3. N. P. Gadetskiĭ, I. I. Magda, S. I. Naĭsteter, *et al.*, Fiz. Plazmy **19** (4), 530 (1993) [Plasma Phys. Rep. **19**, 273 (1993)].

4. S. A. Kitsanov, A. I. Klimov, S. D. Korovin, *et al.*, in *Proceedings of the 1st International Congress on Radiation Physics, High Current Electronics, and Modification of Materials, Tomsk, 2000*, Vol. 2, p. 423.

5. V. D. Selemir, A. E. Dubinov, I. V. Konovalov, and N. N. Makarova, RF Patent No. 2123740, MKI: H 01 J 25/68, Byull. Izobret., No. 35 (1998).

6. A. E. Dubinov and V. D. Selemir, Pis'ma Zh. Tekh. Fiz. **25** (20), 89 (1999) [Tech. Phys. Lett. **25**, 841 (1999)].

7. V. D. Selemir, A. E. Dubinov, I. V. Konovalov, and N. N. Makarova, RF Patent No. 2134920, MKI: H 01 J 25/68, Byull. Izobret., No. 23 (1999).

Translated by P. Pozdeev

Approximate Description of the Nonmaxwellian Electron Distribution in a Global Model

A. A. Kudryavtsev[a] and L. D. Tsendin[b]

[a] St. Petersburg State University, St. Petersburg, Russia
e-mail: akud@ak2138.spb.edu
[b] St. Petersburg State Technical University, St. Petersburg, Russia
e-mail: tsendin@phtf.stu.neva.ru
Received May 24, 2002

Abstract—Within the framework of a global model, the nonmaxwellian behavior of electrons is taken into account in terms of a two-temperature approximation. Using the condition of stationary discharge, it is possible to determine the temperature of high-energy electrons T_{eh} as an eigenvalue. For a given gas, this temperature is a function of the parameter $p\Lambda$ and weakly (logarithmically) depends on the conditions, being virtually the same for various types of gas discharge at $p\Lambda$ = const. Using the energy balance for the electron gas, it is possible to determine the electron density n_e from the absorbed power. © 2002 MAIK "Nauka/Interperiodica".

Fast evaluation of the parameters of a low-pressure gas discharge, in which the charged particles are lost predominantly on the walls and the plasma is characterized by smooth profiles, is most widely performed within the framework of a global model [1–4]. This approach is based on the balance equations for average concentrations of particles and employs the reaction (in particular, ionization) constants obeying the Arrhenius relations with the ratios of the activation energy to the electron temperature ($\sim \exp(-E_j/T_e)$). For this description to be adequate for real situations, it is necessary that the effective electron temperature only slowly vary in the cross section. This implies that the characteristic diffusion length Λ is small compared to λ_T ($\lambda_T \gg \lambda, \Lambda$), which is the distance for which the thermal conductivity (leveling T_e over the volume) dominates in the energy balance of the electron gas [8]. In the global model, the electron temperature T_e (or the average energy $\bar{\varepsilon} = 3T_e/2$) entering into the exponential expression for the frequencies (v_j) of processes involving electrons is determined from the energy balance equation for the whole electron gas.

However, it was established long ago (see, e.g. [5, 6]) that the electron energy distribution function (EDF) significantly differs from the Maxwell distribution (except for the so-called Langmuir paradox observed in the collisionless regime, when the EDF is well approximated by the Maxwell function [7]). For a not very large degree of ionization ($n_e/n < 10^{-3}$) in the inelastic energy range ($\varepsilon > \varepsilon_1$), the EDF is essentially nonequilibrium and depleted of high-energy electrons. The EDF formation is nonlocal [8]; i.e., the distribution

depends on the physical quantities (primarily field strengths) in a region determined by the electron relaxation length λ_T, rather than at a given point. This approach is usually valid for $p\Lambda < 1$ Torr cm. In order to determine the EDF, which depends in this case only on the total energy $\varepsilon = w + e\phi(r)$ (kinetic plus potential), it is necessary to average the Boltzmann equation over the entire discharge volume [8].

For a real (nonequilibrium and nonlocal) EDF, the calculations of v_j based on the Maxwell distribution are physically senseless and the errors of data obtained using this approach are difficult to estimate even qualitatively. For this reason, it was recently suggested (see, e.g., [9, 10]) to use a global model with the EDF representing a distribution of the Druvestein–Davydov type,

$$f_0(\varepsilon) = c_1 \exp(-c_2 \varepsilon^x). \qquad (1)$$

At $x > 1$, this EDF decays with increasing energy more rapidly than does the Maxwell function, thus being closer to real situations.

We believe that using an EDF of type (1) is inexpedient because, strictly speaking, this distribution is valid only for an elastic energy balance of electrons (see, e.g. [5, 6]). However, it is the inelastic losses that dominate in the energy balance of electrons of a low-pressure gas discharge and, hence, the distribution of type (1) with the parameters (c_1, c_2, x) determined from the atomic quantities is never realized. Moreover, considering the distribution (1) merely as an approximation with the fitting parameters c_1, c_2, x is also unfavorable, since these values cannot be determined from reason-

able physical considerations related to special features of the EDF formation.

The purpose of this paper is to suggest the simplest, physically justified approximation of this type for description of the nonmaxwellian EDF within the framework of a global model.

An analysis of the kinetic equation and a comparison of the results of calculations and experiments reported by various researchers shows that the real EDF in a gas discharge plasma is usually satisfactorily approximated in terms of two groups of electrons with the temperatures T_{eb} and T_{eh}:

$$f_0(\varepsilon) = c_n e^{-\frac{\varepsilon}{T_{eb}}} - c_n e^{-\frac{\varepsilon_1}{T_{eb}}} \frac{(T_{eh} - T_{eb})}{T_{eb}}, \quad \varepsilon \le \varepsilon_1,$$

$$f_0(\varepsilon) = c_n \frac{T_{eh}}{T_{eb}} e^{-\frac{\varepsilon}{T_{eh}}}, \quad \varepsilon \ge \varepsilon_1, \quad c_n = 2/\sqrt{\pi T_{eb}^2}. \tag{2}$$

For $\varepsilon \le \varepsilon_1$, expression (2) introduces an additional constant which provides (unlike the two-exponent EDF approximations used in [11–13]) for correct matching of both the function and its derivative at $\varepsilon = \varepsilon_1$.

Using the distribution function (2), it is possible to calculate all the required electron characteristics. In particular, for a linear energy dependence $\sigma_j(\varepsilon) = \sigma_{0j}(\varepsilon/\varepsilon_j - 1)$ of the cross sections of inelastic processes (direct ionization, excitation of lower states, etc.), the rate constants can be determined as

$$v_j = \int_{\varepsilon_j}^{\infty} v_j(\varepsilon) f_0(\varepsilon) \sqrt{\varepsilon} d\varepsilon \approx \frac{T_{eh}}{T_{eb}} N \sigma_{0j} \sqrt{\frac{8T_{eh}}{\pi m}} e^{-\frac{\varepsilon_j}{T_{eh}}}. \tag{3}$$

In order to establish the main relationships between the parameters, let us turn to the scaling law for gas discharges, which follows from an analysis of the balance of particles and energies [5]. Here, the main parameters of the problem are $p\Lambda$, the gas pressure multiplied by the characteristic diffusion length, and W, the power absorbed per unit volume. In dc discharges, a combination of these parameters leads to the well-known similarity parameters $p\Lambda$ and i/Λ (where i is the discharge current) [5]. The calculation of Λ for various discharge geometries was described in [1]. For example, in a plane-parallel geometry $(x = 0, L)$, $\Lambda = L/\pi$; for a cylinder of radius R, $\Lambda = R/2.405$.

The condition of stationary discharge implies equality of the rates of ionization and diffusion loss on the walls:

$$v_i \tau_s = 1. \tag{4}$$

A kinetic description of the ionization process shows that v_i can be represented as a sum $v_i = v_{di} + v_{st}$ of the rates of direct (v_{di}) and stepwise (v_{st}) ionization (for more detail, see, e.g., [14]). When the stepwise ionization dominates, it is a common practice to use an esti-

mate of $v_i \approx c_i v_{ex}$, where c_i is a coefficient on the order of unity and v_{ex} is the rate of excitation of the lower states (immediate ionization approximation [14]). The characteristic time τ_s of the loss of electrons and ions on the walls can be estimated using the interpolation formula [1]

$$\tau_s = \tau_a + \tau_b, \tag{5}$$

where $\tau_a = \Lambda^2/D_a$ is the characteristic time of ambipolar diffusion, $\tau_b = a\Lambda/V_b$, $V_b = \sqrt{T_e/M}$ is the Bohm velocity, and a is a coefficient on the order of unity. Since τ_s in formula (5) is determined by the discharge volume geometry, we may calculate the ionization rate from relation (4) using the corresponding diffusion loss, even without knowledge of the high-energy part of the EDF. In turn, once v_i is known, it is possible to reliably estimate the temperature of the high-energy electrons (T_{eh}). Indeed, since this part weakly (logarithmically) depends on T_{eb}, we can calculate T_{eh} by formulas (2) and (4), where T_{eb} under logarithm is replaced by T_{eh} without significant loss of accuracy.

Eventually, it follows from Eqs. (2)–(5) that the T_{eh} value for a given gas depends only on the parameter $p\Lambda$. Arbitrarily selecting any EDF that sharply (exponentially) depends on the energy, including the Druvestein function (1) or the Maxwell distribution, yields more or less close values of T_{eh} via formula (4) which logarithmically depend on the discharge parameters. Apparently, this low sensitivity of the calculations with respect to details of the high-energy part of the EDF is exactly what accounts for the successful use of global models in calculations.

The kinetic equation leads to the following estimate of the temperature of the high-energy part of the EDF [8]:

$$T_{eh} = \sqrt{\sum_j v_j/D_E}, \tag{6}$$

where $D_E = 2\langle (eE_{eff}\lambda)^2 v \rangle/3$ is the coefficient of energy diffusion in an effective (spatially averaged) electric field (for detail, see [8]). As can be seen from (6) and is evident from the physical considerations, T_{eh} (and, hence, the ionization rate v_i) is determined by the "heating" electric field, which is longitudinal in the positive plasma column and high-frequency in the RF and microwave discharges.

Since it is the field that supplies the energy to electrons, a question naturally arises as to why the calculations using Eqs. (2)–(5) determine the ionization rate v_i and the temperature T_{eh} as functions of only the parameter $p\Lambda$. The main reason for this is that, in all problems of plasma physics, neither the motion of particles nor the fields can be considered as preset: the fields are determined both by the external conditions and by the motion of charged particles, while the motion of parti-

cles is determined by the fields. Therefore, all problems should be treated as self-consistent: the plasma admits penetration into the discharge volume of only those fields "required" for a stationary regime. The ionization rate is determined by the form of the EDF (i.e., by T_{eh}), which is determined by fields in the plasma. On the other hand, it is necessary that the production of charged particles compensate for their loss, which depends primarily on the discharge geometry and the pressure ($p\Lambda$). As a result, the effective average heating field $\langle E_{eff} \rangle$, which can be calculated from relation (6) using the T_{eh} value determined by Eqs. (2)–(4), is also determined by the parameter $p\Lambda$. This possibility was also pointed out in [21]. The spatial distribution of the self-consistent fields in the volume is *a priori* unknown. Determining the field profiles in the plasma of various discharges (ECR, ICP, SW, etc.) is an independent, complicated problem. Attempts at finding T_{eh} as a function of the field strength via relations of the type of (6) usually lead to cumbersome and vague expressions (see, e.g., [13, Eq. (17)]).

Since the absorbed power $W = \langle e^2 E_{eff}^2 n_e/(m\nu)\rangle$ depends on E_{eff} and n_e, determining the quantity $\langle E_{eff}\rangle(T_{eh})$ requires recourse to the energy balance of the electron gas:

$$W = \sum_j \varepsilon_j \nu_j n_e + \delta(\nu_a + \nu_{ei})(T_e - T)n_e + e\varphi_w n_e/\tau_s, \quad (7)$$

where the energy losses correspond to various inelastic processes (ε_j are the electron energy losses due to a *j*th elementary event at a rate of ν_j), elastic losses (ν_a and ν_{ei} are the frequencies of elastic electron–atom and electron–ion collisions), and diffusion cooling (φ_w is the potential difference between the axis and wall). When the ionization rate is close to the excitation rate and the wall potential in a nonlocal regime is close to the ionization potential [8], we obtain

$$W/n_e \approx 2\varepsilon_{ex}\nu_{ex} \approx 2\varepsilon_{ex}/\tau_s. \quad (8)$$

This relation is indicative of the linearity of $n_e(W)$. Once the right-hand part of relation (8) is known, it is possible to determine the electron density from the absorbed power deposited in the discharge (or from the discharge current for a dc discharge).

Knowledge of the temperature of slow electrons (T_{eb}) is necessary for determining the rates of low-threshold processes (such as stepwise), the coefficient of ambipolar diffusion, the potential jump in the near-wall layer, etc. When the role of electron–electron collisions is small ($\nu_e \ll W/(n_e T_{eb})$), the EDF of electrons with $\varepsilon \le \varepsilon_1$ for the inelastic energy balance is independent of the field: $f_0(\varepsilon) \sim \int_\varepsilon^{\varepsilon_1} d\varepsilon/(\varepsilon\lambda(\varepsilon))$ [8]. Accordingly, the average energy determined with this EDF for a power dependence of the frequency of elastic collisions $\nu(\varepsilon) \sim \varepsilon^n$ is also independent of the field: $\bar{\varepsilon}/\varepsilon_1 \approx 3(n +$

$\log[f(\varepsilon)/f(15\ \text{eV})]$
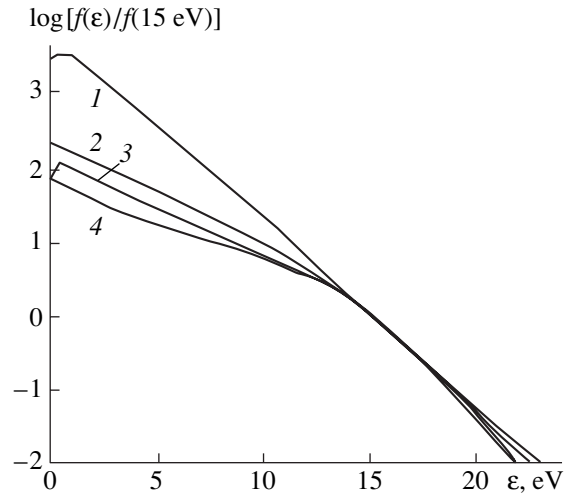
EDFs for induction discharges in argon (cylindrical geometry): (*1*) $R = 22.5$ cm, $h = 2$ cm, $p = 9$ Pa [15]; (*2*) $R = 7.5$ cm, $h = 10$ cm, $p = 1.33$ Pa [16]; (*3*) $R = 10$ cm, $h = 10.5$ cm, $p = 1.33$ Pa [17]; (*4*) $R = 7.5$ cm, $h = 6$ cm, $p = 3$ Pa [18].

1)/5($n + 2$) [8]. A growth in the degree of ionization (increase in W) leads to "maxwellization" of the EDF as a result of the electron–electron collisions. For the given external conditions and known mechanisms of ionization and losses, the temperature of the high-energy part T_{eh} according to (4) remains virtually unchanged. Therefore, an increase in the frequency of electron–electron collisions leads to a change in the EDF of slow electrons; i.e., the "distribution body" temperature T_{eb} approaches the unchanged "tail" temperature T_{eh}. This process is accompanied by a decrease in D_E (and, hence, in the field strength). In the literature (see, e.g., [5, 6, 14]), changes in the EDF with increasing electron density are frequently considered for a fixed field strength. In such cases, variations of the degree of ionization modify both the "body" and the "tail" of the distribution. The figure presents the EDFs for various discharges in argon experimentally measured by different researchers for approximately the same parameter $p\Lambda \approx 30$ mTorr cm (curve *1*, [15, Fig. 5d]; curve *2*, [16, Fig. 5]; curve *3* [17, Fig. 1]; and curve *4* [18, Fig. 10c]). As can be seen, the high-energy parts of the EDFs exhibit a striking coincidence, which confirms the above estimates.

It should also be noted that with high-frequency discharges (CCP, ICP, ECR, SW, etc.), regimes with a large role being played by an "external" (relative to the plasma region) energy supply that are analogous to the negative glow region for a hollow cathode can be realized. These conditions may lead to the formation of a characteristic low-energy peak of maxwellian electrons [19] closed by the self-consistent field in the central region where the deposited energy is small. Then, the EDF of the plasma will exhibit three characteristic regions playing different roles: ensuring quasineutrality, carrying current, and producing ionization. In such

more general cases, one should use a three-temperature approximation distinguishing slow (bulk), intermediate, and fast electrons [8] such that $T_{ei} > T_{eh}, T_{eb}$. Since the ambipolar field and lifetime τ_a are determined by the slow electrons, τ_a will increase, which may lead to a decrease in the electron temperature in the fast part of the EDF [20].

REFERENCES

1. M. Lieberman and A. Lichtenberg, *Principles of Plasma Discharges and Materials Processing* (Wiley, New York, 1994).

2. A. V. Rozhansky and L. D. Tsendin, *Transport Phenomena in Partially Ionized Plasma* (Taylor & Francis, London, 2001).

3. C. Lee and M. A. Lieberman, J. Vac. Sci. Technol. A **13** (2), 368 (1995).

4. A. J. Lichtenberg, V. Vahedi, M. A. Lieberman, *et al.*, J. Appl. Phys. **75**, 2339 (1994).

5. G. Francis, *Ionization Phenomena in Gases* (Butterworths, London, 1960).

6. V. L. Ginsburg and A. V. Gurevich, Usp. Fiz. Nauk **70**, 201 (1960) [Sov. Phys. Usp. **3**, 115 (1960)].

7. A. A. Kudryavtsev and L. D. Tsendin, Zh. Tekh. Fiz. **69** (11), 34 (1999) [Tech. Phys. **44**, 1290 (1999)].

8. L. D. Tsendin, Plasma Sources Sci. Technol. **4**, 200 (1995).

9. J. T. Gudmundsson, Plasma Sources Sci. Technol. **10**, 76 (2001).

10. M. W. Kiehlbauch and D. B. Graves, J. Appl. Phys. **91** (6), 3539 (2002).

11. W. L. Morgan and L. Vriens, J. Appl. Phys. **51** (10), 5300 (1980).

12. A. Hartgers and J. A. M. van der Mullen, J. Phys. D **34**, 1907 (2001).

13. T. Kimura and K. Ohe, J. Appl. Phys. **89** (8), 4240 (2001).

14. L. M. Biberman, V. S. Vorob'ev, and I. T. Yakubov, Usp. Fiz. Nauk **107**, 353 (1972) [Sov. Phys. Usp. **15**, 375 (1973)].

15. G. Mumken, J. Phys. D **32**, 804 (1999).

16. H. Sigh and D. B. Graves, J. Appl. Phys. **87**, 4098 (2000).

17. V. A. Godyak, R. V. Piejak, and B. M. Alexandrovich, J. Appl. Phys. **85**, 3081 (1999).

18. U. Kortshagen, I. Pukropski, and M. Zethoff, J. Appl. Phys. **76**, 2048 (1994).

19. V. A. Godyak, in *Electron Kinetics and Applications of Glow Discharges*, Ed. by U. Kortshagen and L. D. Tsendin (Plenum, New York, 1997), pp. 241–256.

20. S. V. Berezhnoj, I. D. Kaganovich, and L. D. Tsendin, Fiz. Plazmy **24** (7), 603 (1998) [Plasma Phys. Rep. **24**, 556 (1998)].

21. A. S. Smirnov and K. E. Orlov, Plasma Sources Sci. Technol. **8**, 37 (1999).

Translated by P. Pozdeev

The Effect of Adsorption on the Conductivity of Self-Organized Metal–Poly(*para*-xylene) Nanocomposites

E. I. Grigor'ev, P. S. Vorontsov, S. A. Zav'yalov, and S. N. Chvalun

Karpov Institute of Physical Chemistry, State Scientific Center of the Russian Federation,
Moscow, 103064 Russia
e-mail: evg@cc.nifhi.ac.ru
Received April 29, 2002

Abstract—The effect of adsorbed electron donor (ammonia, alcohols, water) and electron acceptor (molecular hydrogen, dichlorobutene, chloroform) molecules on the conductivity of polymeric nanocomposites, representing poly(*p*-xylene) containing metal (lead, copper, or palladium) nanoparticles (~10 nm in size), was studied as dependent on the metal content and the gas or vapor pressure at room temperature. It was found that the conductivity significantly (up to eight orders of magnitude) increases due to the adsorption of electron donor molecules and decreases upon the adsorption of electron acceptors. A mechanism of the sensor response is proposed according to which the adsorption simultaneously changes the fractal characteristics of the nanocomposites and the electron work function of metal nanoparticles. © 2002 MAIK "Nauka/Interperiodica".

Development of analytical instruments of a new type referred to as "electronic nose" requires the creation of "smart" materials capable of exhibiting a large and reversible response to various chemicals present in the surrounding gaseous or liquid phase. In recent years, considerable research interest has been drawn to the so-called polymeric nanocomposites—materials comprising an insulating polymer matrix with dispersed metal or semiconductor nanoparticles [1–3].

The polymeric nanocomposites are characterized by a fractal structure [2]. When the concentration (volume fraction V) of nanoparticles reaches a threshold (critical) value V_c, an infinite conducting cluster is formed and the nanocomposite exhibits a sharp growth in conductivity. For nanoparticle concentrations below this percolation threshold, the conductivity of nanocomposites is determined by the tunneling of charge carriers through thin polymer spacers between nanoparticles and depends on the distance between these particles, the dielectric permittivity of the polymer matrix, and the electron work function of the nanoparticles. The electrical response of nanocomposite sensors is related to a change in these characteristics caused by the molecules of gases and/or vapors adsorbed on the surface of nanoparticles or absorbed by the polymer matrix.

For example, swelling of the polymer matrix of a polymer–soot nanocomposite with a filler content above the percolation threshold in vapors of various solvents leads to breakage of the conducting path, with a resulting increase in the resistance of the composite [4]. The conductivity of a composite, in which the polymer is grafted on the surface of soot particles, is determined by the tunneling of carriers between the carbon nanoparticles. Swelling of the polymer leads to an increase

in the distance between these nanoparticles. Accordingly, the resistance of the nanocomposite exhibits exponential growth with the solvent vapor pressure [5]. In the case of a CuS–poly(vinyl acetate) nanocomposite, the variation of conductivity was attributed in [6] to a change in the dielectric permittivity of the polymer matrix as a result of water absorption, which also influences the tunneling between nanoparticles.

A large sensor response was observed for nanocomposites comprising a poly(*p*-xylene) matrix containing metal or semiconductor nanoparticles in [7, 8]. It is believed that the conductivity of such systems changes as a result of adsorption-induced variation of the electron work function of the nanoparticles. Therefore, by varying the chemical types of a polymer matrix and a filler and by modifying the nanocomposite structure, it is possible to synthesize nanocomposites that exhibit a significant response as sensors at a sufficiently high selectivity.

The aim of our experiments was to study the effect of adsorption on the conductivity of poly(*p*-xylene) films containing metal (Pd, Pb, Cu) nanoparticles in relation to the metal content and the strength of interaction between adsorbed molecules and the particle surface.

The samples were synthesized by codepositing metal vapor and *p*-xylene monomer onto a substrate with platinum contacts cooled to a liquid nitrogen temperature. Subsequent heating of the condensate up to room temperature led to polymerization of the monomer molecules and to aggregation of the metal atoms with the formation of nanoparticles. The procedure was described in detail elsewhere [9]. Mutual influence of the simultaneous polymerization and aggregation pro-
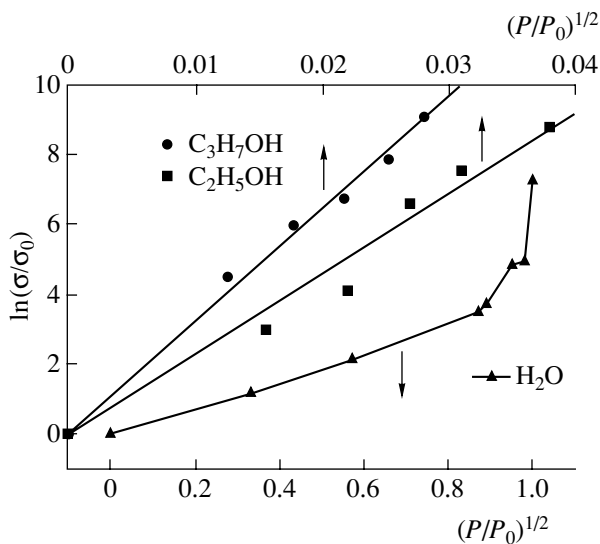
Fig. 1. Plots of the conductivity versus relative pressure (P_0 is the room-temperature saturated vapor pressure) for the adsorption of water, ethanol, and propanol on a Pb-containing nanocomposite sensor.
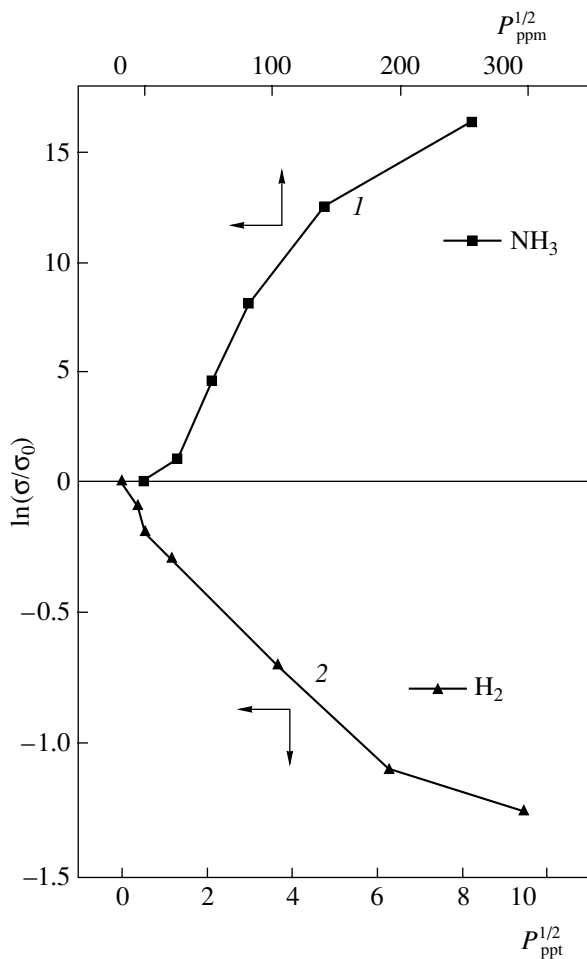

Fig. 2. Plots of the conductivity versus pressure for the adsorption of (*1*) ammonia on a Pb-containing sensor and (*2*) molecular hydrogen on a Pd-containing sensor.

cesses leads to self-organization of the nanoparticles. According to data from atomic force microscopy [10], small (5–10 nm in size) metal nanoparticles are stabilized in the amorphous region and decorate the greater (200–300 nm) poly(*p*-xylene) nanocrystals. The dependence of the conductivity of samples on the volume metal fraction exhibits a percolation character [11] with a threshold of about 5 vol %, which is characteristic of chain structures [12].

In the presence of electron donor (ammonia, alcohols, water) molecules, the conductivity of samples significantly (up to eight orders of magnitude) increased, while the adsorption of electron acceptors (molecular hydrogen, dichlorobutene, chloroform) led to a decrease in the conductivity. Upon evacuation of the gas phase, the room-temperature conductivity restored on the initial level. For the samples containing Cu nanoparticles, the exposure to chloroform at room temperature resulted in irreversible changes in the conductivity. The time of the sensor response varied from several seconds to several minutes, depending on the sensor type and gas pressure.

In our case, the main mechanism by which adsorption influences the conductivity of nanocomposites consists in changing the electron work function of nanoparticles. The adsorption of electron donor molecules (e.g., ammonia) on a metal decreases the electron work function [13]; as a result, the potential barrier also decreases and the conductivity increases. Upon the adsorption of an electron acceptor (e.g., molecular hydrogen on Pd), the electron work function increases [14], the potential barrier grows, the tunneling current drops, and the conductivity decreases.

In the dielectric (insulator) state, the conductivity of composites is determined by the tunneling mechanism of charge carrier transport and obeys the following relation [15]:

$$\sigma \propto \exp(-A\varphi^{1/2}V_c|\Delta V|^n), \qquad (1)$$

where A is a constant factor, φ is the electron work function of nanoparticles, V_c is the percolation threshold, $\Delta V = V_c - V$, V is the volume fraction of a metal, and $n = 1.6$ in a three-dimensional case. In the region of validity of the Henry law, the electron function is proportional to the adsorbate pressure P in the gas phase ($\varphi \sim P$) and, hence,

$$\ln\sigma \sim P^{1/2}. \qquad (2)$$

Figures 1 and 2 show the plots of $\ln(\sigma/\sigma_0)$, where σ_0 is the initial conductivity, versus pressure P for the adsorption of ammonia, ethanol, propanol, and water on a Pb-containing nanocomposite and for the adsorption of molecular hydrogen on Pd-containing samples. As can be seen, the relation (2) is valid for the conductivity of Pb-containing samples exposed to ammonia, ethanol, and propanol vapor and for the Pd-containing sample in hydrogen. For the adsorption of ammonia and hydrogen, deviation of the plots from the linear

Effect of the metal (Pb) content in a poly(p-xylene) based nanocomposite sensor on the sensitivity s with respect to ammonia

s, ppm^{-1}	1.1×10^4	8.4×10^3	5.1×10^2	2.1	5
ΔV	2.5×10^{-2}	2×10^{-2}	1.5×10^{-2}	1×10^{-2}	5×10^{-3}

law (2) at high pressures is related to violation of the Henry law. For Pb-containing samples exposed to water vapor, the conductivity varies according to Eq. (2) only at low vapor pressures and then exhibits a sharp growth.

The values of sensitivity $s = \sigma/(\sigma_0 p)|p \longrightarrow 0$ to ammonium for the nanocomposites with various volume fractions of a metal (Pb) in the nanocomposite are presented in the table. As can be seen, the sensitivity decreases when the metal content approaches the percolation threshold. This is at variance with Eq. (1), according to which the sensitivity must grow. The character of variation of the sensor conductivity as a function of the water vapor pressure and of the sensitivity as a function of the metal concentration is indicative of an adsorption-induced change in the fractal characteristics of nanocomposites.

According to the model of the dynamic network of random resistances [16], we may suggest that a decrease (increase) in the electron work function of a nanoparticle as a result of adsorption leads to the formation (breakage) of conducting bonds between nanoparticles and to an increase (decrease) in the effective conducting volume in the nanocomposite. For adsorbate molecules (e.g., ammonia) strongly interacting with the surface, a change in the sensor conductivity due to variations in the effective conducting volume dominating at low adsorbate pressures. In contrast, for molecules (e.g., water) weakly interacting with the surface of nanoparticles, the influence of this factor is more pronounced at high pressures.

The proposed mechanism of the adsorption-induced changes in the conductivity of nanocomposites is also confirmed by variations in the current–voltage characteristics of samples observed in the presence of gases. Indeed, the characteristics change from linear, observed in vacuum, to nonlinear in the presence of ammonia. At a certain metal concentration in the nanocomposite, the dielectric breakdown takes place even at small applied voltages, after which the parameters of samples do not return to the initial level. The initially nonlinear current–voltage characteristics become linear in the presence of electron acceptor molecules such as dichlorobutene. Especially pronounced was the change in the initially linear current–voltage characteristics of the copper-containing nanocomposites with a metal content above the percolation threshold: upon adsorption of chloroform, the characteristics acquired a nonlinear shape typical of samples with under-threshold metal concentrations.

The above data are indicative of adsorption-induced variations in the magnitude of local electric fields and, hence, in the effective structural characteristics of the nanocomposites studied. Analogous changes in the structural characteristics of nanocomposites have been observed under the action of other external parameters such as temperature [17] and field frequency [18].

Thus, it was demonstrated that high sensitivity to the adsorption of gases and vapors observed for metal-containing nanocomposites based on poly(p-xylene) is related to simultaneous changes in the fractal characteristics of the composite and in the electron work function of metal nanoparticles as a result of adsorption.

REFERENCES

1. D. J. Strike, M. G. H. Meijerink, and M. Koudelka-Hep, Fresenius J. Anal. Chem. **364**, 499 (1999).
2. V. V. Visotskij and V. I. Roldugin, Colloids Surf. A **160** (2), 171 (1999).
3. S. Kirkpatrick, Rev. Mod. Phys. **45** (4), 574 (1973).
4. M. C. Lonergan, E. J. Severin, B. T. Doleman, *et al.*, Chem. Mater. **8**, 2298 (1996).
5. N. Tsubokawa, Y. Shirai, M. Okazaki, and K. Marayama, Polym. Bull. **42**, 425 (1999).
6. D. Godovsky, A. Volkov, V. Sukharev, and M. Moskvina, Analyst **118**, 997 (1994).
7. G. B. Sergeev, V. A. Zagorsky, M. P. Petrukhina, *et al.*, Anal. Commun. **34**, 113 (1997).
8. G. N. Gerasimov, E. I. Grigor'ev, A. E. Grigor'ev, *et al.*, Khim. Fiz. **17** (6), 180 (1998).
9. E. N. Nikolaeva, S. A. Ozerin, E. I. Grigoriev, *et al.*, Mater. Sci. Eng. C **8–9** (1–2), 217 (1999).
10. S. A. Zavyalov, M. Yu. Yablokov, F. N. Pivkina, *et al.*, J. Nanopart. Res. (in press).
11. P. S. Vorontsov, E. I. Grigor'ev, S. A. Zav'yalov, *et al.*, Khim. Fiz. (in press).
12. A. N. Lagarkov and A. K. Sarychev, Phys. Rev. B **53** (10), 6318 (1996).
13. M. Asscher and Z. Rosenzweig, J. Vac. Sci. Technol. A **9** (3), 1913 (1991).
14. S. Wilker, D. Henning, and R. Lober, Phys. Rev. B **50** (4), 2548 (1994).
15. A. K. Sarychev and F. Brouers, Phys. Rev. Lett. **73** (21), 2895 (1994).
16. Y. Gefen, W.-H. Shin, R. L. Leibowitz, *et al.*, Phys. Rev. Lett. **57** (24), 3097 (1986).
17. B. Raquet, M. Goiran, N. Negre, *et al.*, Phys. Rev. B **62** (24), 17 144 (2000).
18. A. B. Pakhomov, S. K. Wong, X. Yan, *et al.*, Phys. Rev. B **58** (20), R13375 (1998).

Translated by P. Pozdeev

Variation of the Structure of Amorphous Lead Titanate in the Course of Crystallization

L. N. Korotkov, S. A. Konstantinov, Yu. V. Barmin, I. V. Babkina,
A. V. Bondarev, V. V. Posmet'ev, and S. N. Kozhukhar'

Voronezh State Technical University, Voronezh, Russia
e-mail: 1_korotkov@mail.ru
Received May 6, 2002

Abstract—The laws of formation of an equilibrium crystalline structure of lead titanate during crystallization from an amorphous state were studied. The initial thermal treatment leads to structural relaxation of the amorphous state. Subsequently, an intermediate state is formed whereby cubic phases with perovskite and pyrochlore structures coexist in the amorphous matrix. Finally, an equilibrium tetragonal phase is established at room temperature. © *2002 MAIK "Nauka/Interperiodica".*

Lead titanate ($PbTiO_3$) is one of the main components of ferroelectric materials employed in various electronic devices. In cases when the compound is synthesized by spraying in vacuum [1–3] or by chemical vapor deposition from organometallic compounds [3–6], the initial material usually possesses an amorphous structure and acquires ferroelectric properties upon thermal treatment. The properties of the final material significantly depend on the conditions of annealing, which is naturally related to changes in the real structure.

Amorphous and semicrystalline compounds prepared from ferroelectric crystals offer the possibility of controlled variation of the structure and the crystal grain size of samples. This makes such materials convenient objects for investigating the effects of violations in the translation symmetry of a crystal lattice on the cooperative phenomena taking place in samples on both meso- and microscopic levels. Original investigations of this kind, undertaken more than two decades ago, were connected to a considerable extent with the study of amorphous and semicrystalline lead titanate [7–9]. However, despite the number of publications devoted to this object, no detailed investigations of the process of structural variations in the course of crystallization in a broad temperature range have been performed. In this context, the aim of our experiments was to study features of the formation of an equilibrium crystal structure of lead titanate.

The samples for investigation were prepared in the form of thin plates cut to ~$3 \times 3 \times 0.01$ mm from a melt-spun material. To this end, a powder of synthesized lead titanate was melted in a quartz ampule at a temperature of 1300°C and quenched by pouring onto a rapidly rotating copper disk. An analysis of the chemical composition of the as-quenched samples using an electron-probe microanalyzer of the JXA-840 type showed the following composition (at. %): Pb, 15.59; Ti, 14.07; O, 63.49; and Si (impurity), 6.85.

During experiments, the samples of the initial amorphous material were heated to a certain temperature (T_{an}) and annealed at this temperature for ~20 min. After each annealing step, the X-ray diffraction curves $I(2\theta)$ were measured in a Bragg–Brentano scheme on a DRON-3 diffractometer using MoK_α radiation filtered by an MGP-RD50 graphite monochromator in a diffracted beam. The measurements were performed in the point-by-point mode with a 40-s data accumulation at each step.

Figure 1a shows the $I(2\theta)$ curve of a sample measured before the thermal treatment. The shape of this diffraction pattern is typical of an amorphous material. Thermal annealing at temperatures below 600°C did not led to the formation of a crystalline phase (Fig. 1b), although the first peak in the $I(2\theta)$ curve slightly shifted toward greater angles and somewhat increased in height.

Taking into account that the maximum contribution to the scattering intensity is due to lead atoms [10], we can estimate the radius R_1 (i.e., the Pb–Pb distance) of the first coordination sphere using the expression for a monoatomic amorphous body [10]:

$$R_1 = \frac{7.73\lambda}{4\pi(\sin\theta)}. \qquad (1)$$

The values of R_1 (see table) approximately correspond to the parameter $a = 3.899$ Å [11] of the unit cell of a crystalline $PbTiO_3$. From this we conclude that the short-range order structures of the amorphous and crystalline $PbTiO_3$ are not significantly different, although the atoms in the amorphous state are packed somewhat more closely. This conclusion agrees with the EXAFS data [9], according to which the Pb–Ti and Pb–O dis-

tances in lead titanate exhibit a slight (~5%) growth upon crystallization of the samples. A decrease in R_1 as a result of the thermal treatment is evidence of structural relaxation in the amorphous material, which is apparently related to a decrease in the free volume [12].

After annealing at $T_{an} \sim 600°C$, sharp peaks appear on the background characteristic of the amorphous state (Fig. 2a). This is evidence of the formation of crystalline regions in the amorphous matrix. An analysis of the positions of the Bragg peaks observed at room temperature indicated the presence of a cubic $PbTiO_3$ phase with perovskite structure and a cubic $Pb_2Ti_2O_7$ phase with pyrochlore structure. According to the published data [3, 9, 13], the latter phase is not characteristic of lead titanate and can be related to the presence of a silicon impurity in the material studied [13].

The cubic $PbTiO_3$ phase, existing in the usual crystalline lead titanate at temperatures above the ferroelectric phase transition ($T_c \cong 490°C$), remains stable up to room temperature. This is unambiguously confirmed by the absence of reflections characteristic of the tetragonal phase (cf. diffractograms in Figs. 2a–2c). By taking into account the nanocrystalline character of the structure formed in the initial stage of crystallization, we may suggest that the dimensional effect is among the factors leading to stabilization of the paraelectric phase [14, 15].

At the same time (see table), the parameters of the unit cells of both crystalline phase present in the samples significantly (by ~10%) exceed the values reported in the literature [11]. This is probably related to a violation of the local stoichiometry in the compound stud-
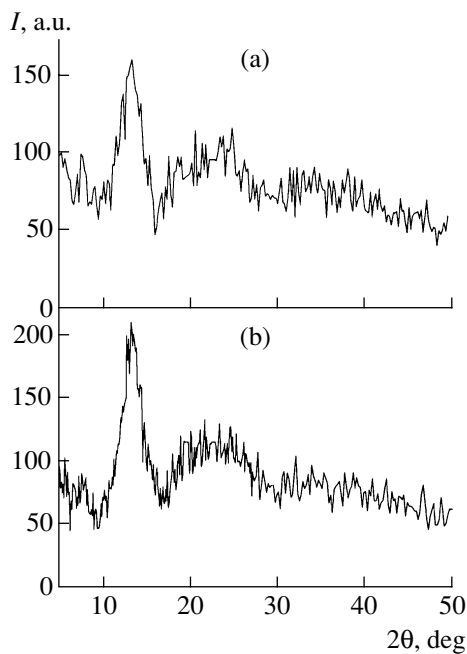
ied. We may suggest that an increase in the unit cell parameters is caused by a partial substitution of Pb^{4+} and Pb^{2+} ions for Ti^{4+}, which was observed in crystalline lead titanate annealed under appropriate conditions [16].

Subsequent thermal treatments ($T_{an} \sim 620$ and $670°C$) led to an increase in the intensity of X-ray diffraction reflections (Figs. 2b, 2c), which is indicative of a growth in the total fraction of crystalline phases (see table). This was accompanied by the transformation of lead titanate from the cubic into tetragonal modification. It should be noted that the regime of thermal annealing after which the tetragonal lattice distortions become noticeable approximately corresponds to the conditions of treatment leading to the formation of an anomaly (at ~490°C) in the temperature dependence of the dielectric permittivity [17]. This anomaly is a sign of the ferroelectric phase transition.

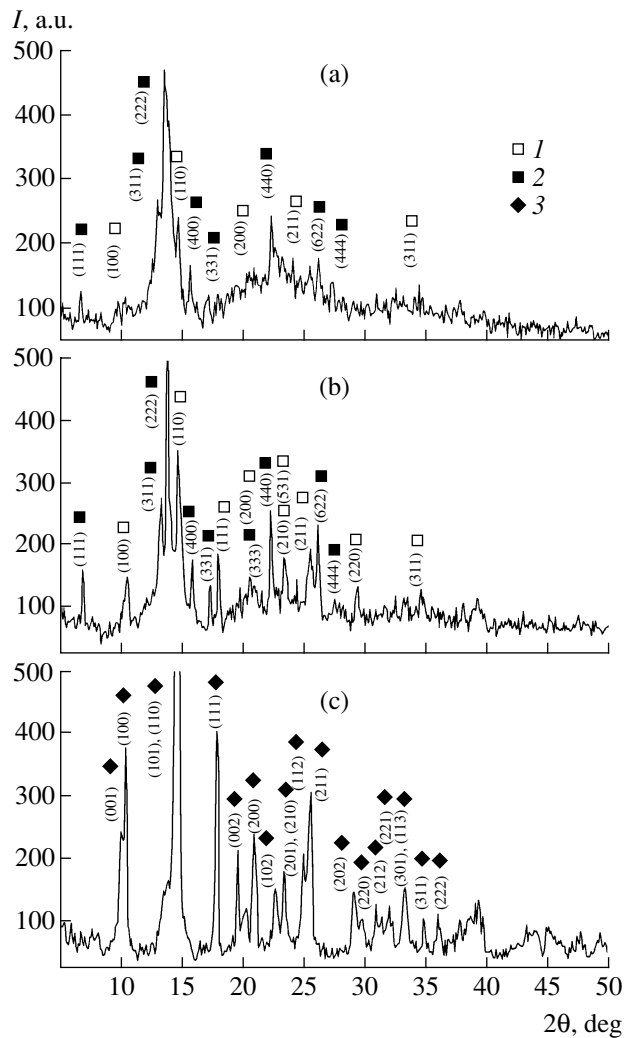After the final annealing stage, the X-ray diffraction lines related to the cubic $Pb_2Ti_2O_7$ phase disappear and

Fig. 2. X-ray diffraction patterns of a lead titanate sample annealed at (a) 600, (b) 620, and (c) 670°C showing reflections corresponding to the (1) cubic $Pb_2Ti_2O_7$, (2) cubic $PbTiO_3$, and (3) tetragonal $PbTiO_3$ phases.

Fig. 1. X-ray diffraction patterns of a $PbTiO_3$ sample in (a) the initial state and (b) after the anneal at 570°C.

Data on the structure of lead titanate after sequential anneals at various temperatures

Step no.	T_{an}, °C	Structure	Amorphous phase fraction, %	R_1, Å	Unit cell parameters, Å		
					a	c	a, c (Ref.)
1	470	Amorphous	100	3.785			
2	500	Amorphous	100	3.784			
3	540	Amorphous	100	3.764			
4	570	Amorphous	100	3.746			
5	600	Amorphous	81				
		$PbTiO_3$ (cub., perovskite)			4.39		3.96 [14]
		$Pb_2Ti_2O_7$ (cub., pyrochlore)			11.58		10.4 [11]
6	620	Amorphous	69				
		$PbTiO_3$ (cub., perovskite)			4.39		
		$Pb_2Ti_2O_7$ (cub., pyrochlore)			11.62		
7	670	Amorphous	0				
		$PbTiO_3$ (tetr., perovskite)			3.917	4.177	3.899
							4.153 [11]

the diffractogram exhibits only peaks corresponding to the tetragonal modification of lead titanate (Fig. 2c). The resulting lattice is characterized by parameters a and c close to the published values [11].

Thus, the experimental results reported above showed that the short-range order structures of lead titanate in the crystalline and amorphous states are apparently do differ not significantly; however, the latter structure is somewhat more closely packed. Thermal anneals in the crystallization temperature region lead to an initial structural relaxation in the amorphous state. Subsequent thermal treatment leads to the formation of a state characterized by the coexistence of a cubic $PbTiO_3$ phase with perovskite structure and a cubic $Pb_2Ti_2O_7$ phase with pyrochlore structure in the amorphous matrix at room temperature. Final anneals lead to the formation of an equilibrium tetragonal phase of lead titanate.

REFERENCES

1. N. S. Multani, P. Ayyub, V. R. Palkar, *et al.*, Bull. Mater. Sci. **6** (2), 327 (1984).

2. M. Kitabatake, T. Mitsuyu, and K. Wasa, J. Appl. Phys. **56**, 1780 (1984).

3. T. Shiosaki and T. Shimizu, Ferroelectrics **170**, 47 (1995).

4. Yu. Xu and J. D. Mackenzie, Integr. Ferroelectr. **1**, 17 (1992).

5. Y. Masuda, Ferroelectrics **170**, 65 (1995).

6. D. Bersani, P. Lottici, A. Montenero, *et al.*, J. Non-Cryst. Solids **192–193**, 490 (1995).

7. M. Takashige and T. Nakamura, J. Phys. Soc. Jpn., Suppl. B **49**, 143 (1980).

8. T. Nakamura and M. Takashige, J. Phys. Soc. Jpn., Suppl. B **49**, 38 (1980).

9. T. Nakamura, M. Takashige, H. Terauchi, *et al.*, Jpn. J. Appl. Phys. **23** (10), 1265 (1984).

10. A. F. Skryshevskiĭ, *Structural Analysis of Liquids and Amorphous Bodies* (Vysshaya Shkola, Moscow, 1980).

11. *Power Diffraction File. Alphabetical Index Inorganic Compounds* (International Centre for Diffraction Data, Pennsylvania, 1977).

12. K. Suzuki, H. Fujimori, and K. Hashimoto, *Amorphous Metals* (Tokyo, 1982; Metallurgiya, Moscow, 1987), translated from Japanese.

13. B. Jaffe, W. R. Cook, and H. Jaffe, *Piezoelectric Ceramics* (Academic, New York, 1971; Mir, Moscow, 1974).

14. S. Chattopadhyay, P. Ayyub, V. R. Palker, *et al.*, Phys. Rev. B **52**, 13177 (1995).

15. W. L. Zhong, J. Korean Phys. Soc. **32**, S265 (1998).

16. S. V. Titov, Author's Abstract of Candidate's Dissertation in Physics and Mathematics (Rostov-on-Don, 2001).

17. L. N. Korotkov, S. A. Gridnev, S. A. Konstantinov, *et al.*, Izv. Akad. Nauk, Ser. Fiz. **65**, 1124 (2001).

Translated by P. Pozdeev

Variation of the Amorphous Carbon Density under the Action of 10–500 eV Carbon Atoms

V. I. Ivanov-Omskiĭ[a], S. G. Yastrebov[a], and A. Richter[b]

[a] *Ioffe Physicotechnical Institute, Russian Academy of Sciences, St. Petersburg, 194021 Russia*
[b] *University of Applied Research, Wildau, Banchofstrasse, 15745 Wildau, Berlin, Germany*
Received April 17, 2002

Abstract—The process of variation of the density of an amorphous carbon sample under the action of carbon atoms with energies in the range from 10 to 500 eV was numerically modeled using the methods of molecular dynamics. It is shown that a maximum densification of the substrate takes place for energies of bombarding carbon atoms in the interval of 30–40 eV. The results of calculations are compared to experimental data. © *2002 MAIK "Nauka/Interperiodica".*

The model of shallow implantation (subplantation) leading to an increase in density of the subsurface layer of a substrate under the action of implanted homoatoms was originally proposed by Lifshitz *et al.* [1]. This model was theoretically confirmed [2] by a method taking into account the Coulomb interaction between colliding particles [3].

In order to study this model in the energy range from 10 to 100 eV, Uhlmann *et al.* [4] performed a molecular dynamics (MD) calculation proceeding from first principles. The calculation referred to a disordered lattice containing 130 carbon atoms to which no more than 20 new atoms were added in the course of modeling. The results generally confirmed the validity of the subplantation model for incident particle energies exceeding 30 eV. However, it was possible to add only a relatively small number of atoms to the initial system within the framework of the approach employed, since MD methods based on *ab initio* calculations require much computation time and are relatively expensive. On the other hand, restricted statistics significantly decreases the reliability of the results.

In this study, dependences of the absolute values of the sample density (amorphous carbon) on the distance from a surface bombarded by atoms added to the system were determined using the classical MD techniques. A semiempirical formulation of the many body problem reduced to the use of a pair interatomic interaction potential in the form suggested by Brenner [5, 6] allowed the number of particles added to the system to be significantly increased in comparison to the case of the *ab initio* MD calculations.

The results of our numerical experiments showed evidence of a densification of the substrate material in the subsurface region observed for energies of incident atoms in the interval from 3 to 40 eV. The data presented below are in a good agreement with our data reported previously (in relative units) [7]. It should be noted that the statistical averaging of the number of nearest neighbors performed in [7] was probably insufficiently correct; it masked the local character of the subplantation effect. This circumstance is also confirmed by the data obtained in [8], where an increase in the number of nearest neighbors averaged over the total number of atoms required modification of the shape of the Brenner potential. We present the absolute values of the density distribution; this allows the original calculated values to be compared to the experimental data from [8] without introducing changes to the empirical potential.

The semiempirical pair potential of the C–C interaction employed in this study was originally introduced by Brenner [5, 6]. This potential refines the shape of the potential function suggested by Tersoff [9] and (in contrast to the latter potential) allows us to describe both the lattices of diamond and graphite and the conjugated bonds in hydrocarbons. The proposed potential ensures a better agreement with experiment for modeling carbon clusters containing small numbers of atoms. The classical MD approach [10] is based on numerical integration of the equations of motion, whereby forces acting upon every atom of the system are determined using the dependence of the potential function on the distance.

We employed two models of the substrate as composed of amorphous carbon. The mutual arrangement of atoms modeling the substrate material was taken from [11], where it was determined proceeding from first principles. The first model corresponded to amorphous carbon with a density on the order of 2 g/cm^3 (low-density substrate), while the second model had a density on the order of 3 g/cm^3 (high-density substrate). Both substrates consisted of cells composed of 128 carbon atoms. For energies of atoms added to the system not exceeding 30 eV, the substrate comprised eight such cells (1024 atoms), while the substrate bombarded by
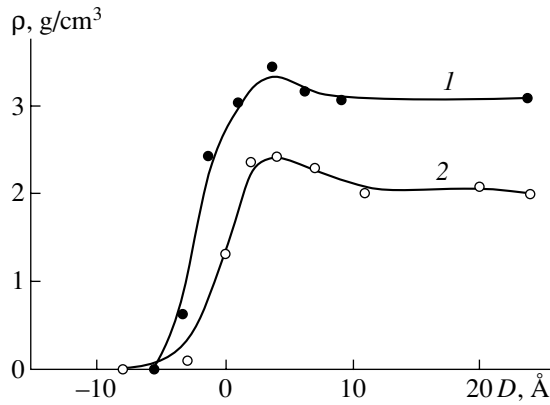
ρ, g/cm³

Fig. 1. Material density profiles obtained after adding 400 carbon atoms to an initial amorphous carbon substrate of (*1*) high and (*2*) low density. Zero coordinate *D* corresponds to the initial substrate surface.
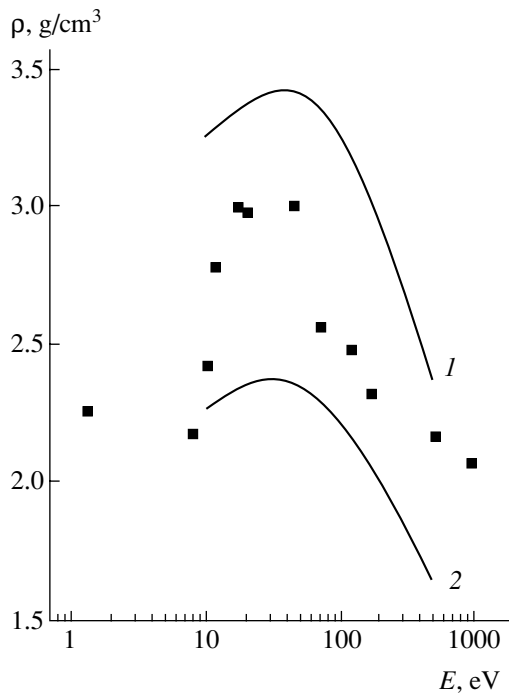

Fig. 2. A plot of the density of amorphous carbon versus the energy of atoms bombarding the substrate surface. Black squares represent the experimental EELS data [12]; curves show the results of our numerical experiments for the (*1*) high-density and (*2*) low-density substrates.

carbon atoms with energies exceeding 100 eV contained 16 cells (2048 atoms).

The periodic boundary conditions fixed atoms on the boundaries and on the bottom of the cell, while the upper surface of the cell remained free. Since atoms at the cell surface are not fixed and contain a large number of dangling bonds, the substrate surface in the model employed is far from equilibrium. For this reason, before adding new carbon atoms to the substrate, the surface was allowed to relax for 2 ps. During the subse-

quent 2 ps, excess energy was removed from the system by introducing damping with a time constant on the order of 2 ps into the equations of motion. The same procedure was employed in the course of adding new atoms to the system, whereby a carbon atom possessing a certain energy was normally incident onto the substrate surface and struck a randomly selected point on this surface. Prior to adding each subsequent atom, the substrate was allowed to evolve for 4 ps according to the algorithm described for the free surface. The computation process was terminated upon adding 400 atoms to the system.

Figure 1 presents the results of numerical modeling for carbon atoms incident with an energy of 30 eV. As is seen, the depth profile of the material density exhibits a maximum at a certain distance from the initial surface. The absolute value in the maximum significantly depends on the initial material density, the maximum density (~3.5 g/cm³) being observed for the high-density substrate.

A comparison of the numerical and real experiments at various energies was performed for the results of calculations at a depth of 4 Å from the initial surface. The experimental profiles were restored from the values of plasma frequencies [12] determined from electron energy loss spectroscopy (EELS). This method is sensitive to the state of the sample surface, which justifies the comparison of real and numerical experiments.

Figure 2 shows a plot of the densities versus the energy of incident atoms. As can be seen from this plot, the substrate material reaches a maximum density for incident energies of 30–40 eV. The numerical results for the substrates of both types repeat the shape of the experimental plot but differ from the latter in absolute value. This discrepancy is probably related to the fact that the experiments reported in [12] were performed on silicon, while our substrate was made of amorphous carbon.

Thus, we have constructed a realistic model and used it to study the effect of densification of an amorphous carbon substrate in the course of bombardment with carbon atoms at various energies. A comparison of the results of numerical and physical experiments shows that selection of the initial substrate material and the energy range of bombarding particles is of practical importance for realization of diamond synthesis by the method of low-energy ion (atom) bombardment.

REFERENCES

1. Y. Lifshitz, S. R. Kasi, J. W. Rabalais, and W. Eckstein, Phys. Rev. B **41**, 10468 (1990).

2. Y. Lifshitz, S. R. Kasi, and J. W. Rabalais, Phys. Rev. Lett. **62**, 1290 (1989).

3. J. F. Ziegler, J. P. Biersack, and U. Littmark, *The Stopping and Ranges of Ions in Matter* (Pergamon, Oxford, 1985).

4. S. Uhlmann, T. Frauenheim, and Y. Lifshitz, Phys. Rev. Lett. **81**, 641 (1998).

5. D. W. Brenner, Phys. Rev. B **42**, 9458 (1990).

6. D. W. Brenner, Phys. Rev. B **46**, 1948 (1992).

7. S. Yastrebov and R. Smith, Nucl. Instrum. Methods Phys. Res. B **180** (1–4), 145 (2001).

8. H. U. Jaeger and K. Albe, J. Appl. Phys. **88**, 1129 (2000).

9. J. Tersoff, Phys. Rev. Lett. **61**, 2879 (1988).

10. R. Smith, *Atomic & Ion Collisions in Solids and at Surfaces* (Cambridge Univ. Press, Cambridge, 1997).

11. Th. Frauenheim, G. Jungnickel, Th. Koehler, *et al.*, J. Non-Cryst. Solids **182**, 1861 (1995).

12. D. R. McKenzie, D. Muller, and B. A. Pailthorpe, Phys. Rev. Lett. **67**, 773 (1991).

Translated by P. Pozdeev

Modification of the Electrical and Optical Properties of Hydrated Vanadium Pentoxide as a Result of Proton Electromigration

E. L. Kazakova, A. L. Pergament, and G. B. Stefanovich
Petrozavodsk State University, Petrozavodsk, Karelia, Russia
e-mail: gstef@mainpgu.karelia.ru
Received April 22, 2002

Abstract—Variation of the optical and electrical properties of films of hydrated vanadium pentoxide under the action of an applied electric field was studied. The samples exhibited an "internal" electrochromic effect caused by a redistribution of hydrogen ions in the film, rather than by their penetration from outside (electrolyte). The process of cathodic polarization at a current of $I \sim 10^{-5}$ A for $t \sim 10$ min is accompanied by a local increase in the hydrogen concentration (confirmed by direct measurements of the ionic conductivity), leading to a change in the optical properties. This is manifested by an increase in the transmission coefficient in the longwave spectral region and by a shift of the absorption edge (at $h\nu = 2.3$ eV) toward greater wavelengths. According to the IR spectroscopy data, this is also accompanied by some increase in the water content in colored regions of the $V_2O_5 \cdot nH_2O$ film. © 2002 MAIK "Nauka/Interperiodica".

The process of electromigration is of considerable interest in various fields of solid state physics and are important from the standpoint of electronic technology and operation of solid state electronic devices. For example, the electromigration of metal atoms (Cu, Al) from conductors in integrated circuits is one of the reasons for failures in electronic equipment. On the other hand, the electromigration of gold can be used as an effective technology for the formation of contacts in nanoelectronic devices [1].

The class of materials and phenomena in which a high ionic conductivity plays the determining role includes superionic conductors and solid electrolytes, the electrochromic effect in transition metal oxides, and electroforming in amorphous semiconductors. In the latter case, chemical and structural transformations in a strong electric field result in the formation of channels possessing special electrical properties (negative differential conductivity) [2]. The electrochromic effect is related to the injection of cations—usually hydrogen or alkali metals—from outside (electrolyte) under the action of an applied field [3].

At present, hydrated vanadium pentoxide $V_2O_5 \cdot nH_2O$ obtained by sol–gel technology draws the attention of researchers owing to a number of promising applications [4–6]. From the standpoint of electrical properties, vanadium pentoxide is a semiconductor featuring mixed electronic and ionic (proton) conductivity. While the intrinsic ionic conductivity of hydrated vanadium pentoxide has been studied in sufficient detail, changes in the material properties related to the process of electromigration have remained practically unstudied.

The aim of our experiments was to study modification of the optical and electrical properties of a $V_2O_5 \cdot nH_2O$ ($n = 1.6$–1.8) xerogel under the action of an applied dc voltage. The samples were prepared as described elsewhere [7]. The optical properties in the visible range ($\lambda = 400$–900 nm) were studied with an SF-46 spectrophotometer using films on glass substrates, while the IR spectra ($\nu = 400$–4000 cm^{-1}) were recorded on a Specord M80 spectrophotometer using films on silicon substrates. The ac conductivity of $Au/V_2O_5 \cdot nH_2O/Al$ sandwich structures was measured using a VM-507 instrument in the frequency range from 5 Hz to 0.5 MHz.

The sample films with a thickness of $d \approx 10$ μm on glass substrates were treated by passing a constant current of 10–20 μA for a time period of 10–30 min in a two-electrode planar system with an interelectrode distance of ~1 mm. The passage of current through a sample was accompanied by the appearance and gradual increase of a red spot at the cathode. The effect was fully reversible. In the sandwich structures studied, a deposited Al electrode (1 mm in diameter) served as the cathode. In these samples, the currents and the coloration times were approximately the same as those in the planar structures. However, the voltage drop across such structures was significantly smaller (not exceeding several volts) than that in the planar scheme. The observed effect of coloration is qualitatively similar to the electrochromic effect, but it takes place in a "dry" system not involving an electrolyte. For this reason, we termed the observed phenomenon the "internal" electrochromic effect. The usual electrochromic effect in

V_2O_5 was originally reported in [8]. In addition, V_2O_5 exhibits photo- and thermochromic effects [6, 9]. In [6], the photochromic behavior was studied for V_2O_5 films prepared using sol–gel technology.

Figure 1a shows the transmission coefficient as a function of the light wavelength. As can be seen, coloration of the sample is accompanied by a shift of the absorption edge toward longer wavelengths. As a result, the optical bandgap width decreases from 2.28 to 2.22 eV (Fig. 1b). The bandgap $E_g \approx 2.3$ eV agrees well with the corresponding value $E_g = 2.35$ eV reported for V_2O_5 films [10]. This coincidence indicates that the intrinsic absorption in $V_2O_5 \cdot nH_2O$, as well as that in a pure (anhydrous) vanadium pentoxide, is due to the $O2p \longrightarrow V3d$ electronic transitions. A small variation of E_g is probably related to some distortion of the V–O polyhedra in the structure of $V_2O_5 \cdot nH_2O$ (the bandgap in V_2O_5 is known to be extremely sensitive to such distortions, for example, to symmetrization of the oxygen octahedron [9]).

It should be noted that, despite the change in E_g being insignificant (not exceeding 0.1 eV), the observed visual contrast is rather pronounced. The film color changed from yellow-green or yellow-brown (depending on the film thickness d) to red or dark purple, respectively. This is related to the fact that coloration leads not only to a shift of the absorption edge but also to a significant decrease in the level of absorption in the red spectral region (increase in transmission, see Fig. 1a). A comparison of the IR absorption spectra of the initial and colored films shows evidence of an increase in the concentration of water molecules in the colored spot (probably due to interaction of H^+ ions with V−OH defects). In addition, colored samples exhibit more intense absorption in the range from 2800 to 3600 cm^{-1} (corresponding to the stretching vibrations of water molecules) and in the region of 1600 cm^{-1} (H_2O bending vibrations) [5]. At the same time, the intensities of the absorption bands in the region of 500–700 cm^{-1} corresponding to vibrations of the V–O bonds remain virtually unchanged.

In order to elucidate the mechanism responsible for modification of the optical properties of a V_2O_5 gel, we also studied the electrophysical properties of initial and modified films. Measurements of the impedance Z and phaseshift angle φ showed that Z decreases with increasing frequency, while the frequency dependence of $\tan\delta = -\cot\varphi$ exhibits a characteristic minimum at ~500 Hz. The analysis of changes in the $Z(f)$ and $\tan\delta(f)$ values was performed based on an equivalent scheme, depicted in Fig. 2. As is known, the choice of one or another substitution scheme to describe the properties of a given structure is determined by the frequency characteristics. For example, the scheme in the inset to Fig. 2 describes the behavior of a system with a minimum in the dielectric loss tangent [11]. In select-
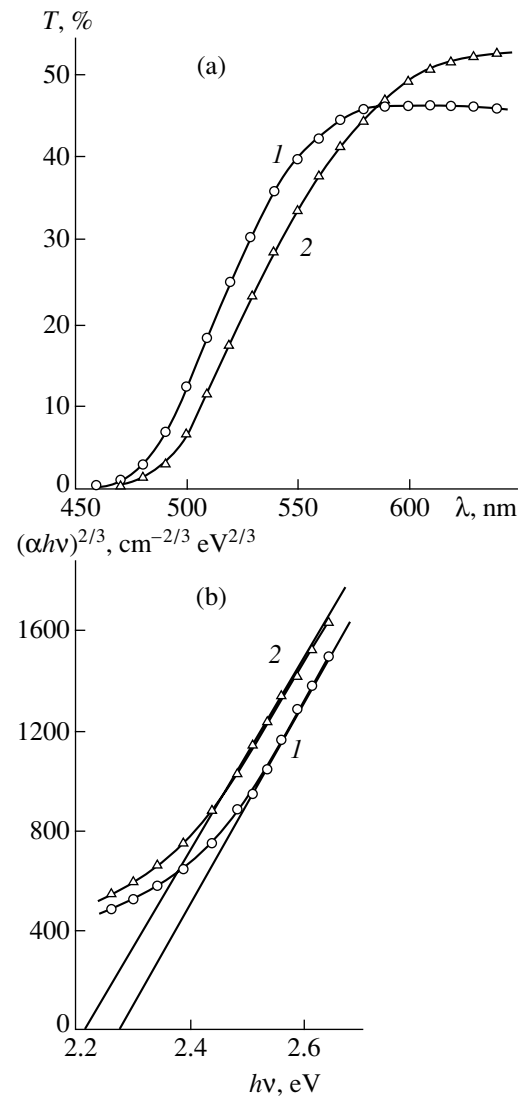

Fig. 1. Modification of the optical properties of a V_2O_5 gel as a result of the internal electrochromic effect, illustrated by (a) the experimental transmission spectrum and (b) absorption coefficient (calculated as described in [10]) in the coordinates corresponding to direct forbidden transitions: (*1*) initial film; (*2*) the same film after application of an electric field ($I = 8$ μA, $t = 10$ min).

ing the equivalent scheme, we took into account that the system studied possesses electronic conductivity (R), ionic conductivity (r), and a capacitance (C). In this scheme, resistance r describes losses caused by the migration polarization of protons [11]. Using the experimental data for $Z(f)$ and $\tan\delta(f)$ and taking into account the condition of minimum for $\tan\delta(f)$, we calculated the frequency dependences of the ionic component of the resistance for the initial and colored films (Fig. 2). In order to determine three unknowns (R, r, C) from two equations (for Z and $\tan\delta$), the function $R(f)$ was considered to be preset, $R = Af^{-s}$ (where $A = $ const). The dependence of the conductivity of disordered mate-
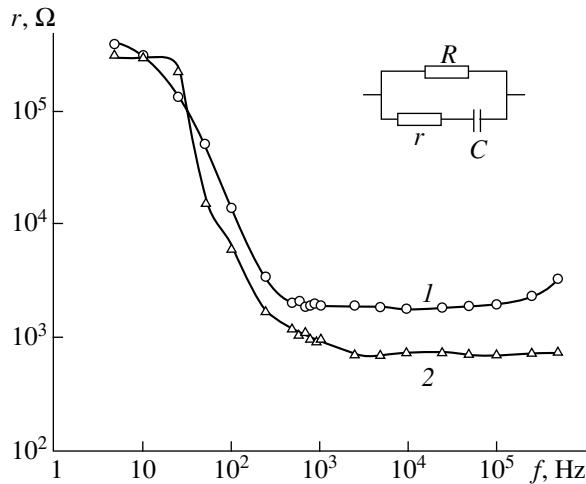
r, Ω

Fig. 2. Frequency dependences of the resistance modeling the ionic component of the conductivity of a V_2O_5 gel: (*1*) initial film; (*2*) the same film after coloration in a sandwich structure exposed to an electric field ($I = 20$ μA, $t = 30$ min). The inset shows an equivalent scheme used in the calculations.

their optical and electrical properties caused by the redistribution of protons as a result of electromigration under the action of an applied electric field. In concluding, it should be noted that electrochromic materials are promising for use in small-size displays, current-controlled optical filters, etc. [3, 4, 6, 8]. In this respect, the observed "internal" electrochromic effect, showing the possibility of eliminating electrolyte, is of special interest for technical applications.

rials behaving as $\sigma \sim f^s$ ($s = 0.7$–0.9) is well known [2]. We have experimentally verified this law upon removal of water from one of the samples by annealing at $T = 300°C$, which eliminates the ionic conductivity component [4]. It was found that the dispersion of $R(f)$ is actually described by a power function in a broad frequency range with $s = 0.71 \pm 0.07$.

As can be seen from Fig. 2, cathodic polarization leads to a local increase in the ionic conductivity and, hence, results in an increasing proton concentration in the colored region. This accounts for the electrochromic coloration, that is, for modification of the optical properties (Fig. 1). It should be noted that, in contrast to the standard electro- and photochromic effects in V_2O_5, we observed an opposite color contrast: from yellow to red, rather than from yellow to green [4, 6, 8, 9]. This behavior can be explained by the presence of water, the concentration of which (according to the IR data) also increases in the course of coloration. However, this question (concerning the contrast inversion) is not quite clear and requires additional investigation.

Thus, the results presented above indicate that the films of a $V_2O_5 \cdot nH_2O$ xerogel exhibit modification of

REFERENCES

1. A. P. Alivisatos, J. Park, and P. L. Mc Euen, Appl. Phys. Lett. **75**, 301 (1999).
2. N. F. Mott and E. A. Davis, *Electronic Processes in Non-Crystalline Materials* (Clarendon, Oxford, 1979; Mir, Moscow, 1982).
3. B. W. Faughnen and R. S. Crandall, in *Display Devices,* Ed. by J. I. Pankov (Springer-Verlag, New York, 1980; Mir, Moscow, 1982).
4. J. Livage, Chem. Mater. **3** (4), 578 (1991); J. Livage, J. Sol-Gel Sci. Technol. **19**, 275 (2000).
5. R. N. Pletnev, A. A. Ivakin, D. G. Kleshchev, T. A. Denisova, and V. A. Burmistrov, *Hydrated Oxides of Group IV and V Elements* (Nauka, Moscow, 1986).
6. A. I. Gavrilyuk and T. G. Lanskaya, Pis'ma Zh. Tekh. Fiz. **20** (6), 12 (1994) [Tech. Phys. Lett. **20**, 219 (1994)].
7. G. B. Stefanovich, A. L. Pergament, and E. L. Kazakova, Pis'ma Zh. Tekh. Fiz. **26** (12), 62 (2000) [Tech. Phys. Lett. **26**, 478 (2000)].
8. A. I. Gavrilyuk and F. A. Chudnovskiĭ, Pis'ma Zh. Tekh. Fiz. **3** (4), 174 (1977) [Sov. Tech. Phys. Lett. **3**, 69 (1977)].
9. A. I. Gavrilyuk, N. M. Reĭnov, and F. A. Chudnovskiĭ, Pis'ma Zh. Tekh. Fiz. **5** (20), 1227 (1979) [Sov. Tech. Phys. Lett. **5**, 514 (1979)].
10. C. V. Ramana, B. S. Naidu, O. M. Hussain, *et al.*, J. Phys. D **34**, L35 (2001).
11. I. S. Rez and Yu. M. Poplavko, *Dielectrics: Basic Properties and Applications in Electronics* (Radio i Svyaz', Moscow, 1989).

Translated by P. Pozdeev

Cutoff Regimes
in Amplifying (Absorbing) Planar Waveguides

D. G. Sannikov and D. I. Sementsov

Ul'yanovsk State University, Ul'yanovsk, Russia
e-mail: sements@sv.uven.ru
Received April 11, 2002

Abstract—The cutoff conditions are determined for a planar waveguide containing an amplifying (or absorbing) waveguide layer. The dependence of the waveguide layer thickness and propagation constant on the level of gain (damping) in the waveguide under the cutoff conditions is numerically analyzed. © *2002 MAIK "Nauka/Interperiodica".*

Introduction. The behavior of guided optical modes in planar waveguide structures with absorption has been extensively studied [1–5]. In recent years, considerable research attention has been devoted to the active waveguide structures possessing amplification properties [6, 7]. In particular, active waveguide structures based on erbium-doped silicon are of interest due to the peak in gain at 1.54 μm, which makes compensation of the intrinsic and dispersive losses possible [8–10].

The presence of an imaginary component in the dielectric permittivity of one layer of a waveguide structure renders the waveguide mode propagation constant a complex quantity [2, 11] and leads to the appearance of surface modes of the polariton type [12]. Another important characteristic of a waveguide structure is the cutoff thickness L_c for which a mode converts from waveguide to radiative [1]. In a traditional three-layer waveguide structure with real permittivities of layers, the cutoff thickness L_c corresponds to a minimum propagation constant $\beta_C = 2\pi/\lambda_1$, which is the same for all waveguide modes (λ_1 is the light wavelength in the substrate).

The presence of gain (damping) in a waveguide leads to violation of this correspondence. No detailed analysis of the cutoff conditions for various modes in such structures has been reported in the literature. We used numerical methods to study the cutoff conditions and the corresponding characteristics of a planar three-layer waveguide with an active guiding layer.

Description of the model. Consider a planar three-layer waveguide structure comprising the substrate, the main waveguide layer, and the coating material. Let the permittivities of the substrate (ε_1) and the coating material (ε_3) in the frequency range studied be real and the waveguide layer possess a complex permittivity $\varepsilon_2 = \varepsilon_2' + i\varepsilon_2''$. Arrange the structure such that the x axis is perpendicular to the boundaries between layers of the structure. The interface of the substrate and waveguide layer coincides with the plane $x = -L$, while the interface of the waveguide layer and coating material coincides with the plane $x = 0$.

The electromagnetic field components of the waveguide mode propagating in the z axis direction can be presented in the following form:

$$F_\alpha(x, z, t) = \Phi_\alpha(x)\exp[i(\omega t - \beta z)], \qquad (1)$$

where $\alpha = x, y, z$; $\beta = \beta_1 + i\beta_2$ is the complex propagation constant, the imaginary part of which characterizes the mode damping ($\beta_2 < 0$) or gain ($\beta_2 > 0$) and the real part, the phase velocity; and $\Phi_\alpha(x)$ are the components of the vector profile function determining the distribution of the mode field across the waveguide. The β_1 value is usually called the propagation constant of the absorbing (amplifying) waveguide. The component F_y denotes the electric field component E_y for a TE mode and the magnetic field component H_y for a TM mode. In the waveguide geometry chosen, this component is transverse with respect to the propagation direction and tangential with respect to the layer boundaries. The corresponding component of the profile function is as follows:

$$\Phi_y(x)$$

$$= A\begin{cases} \exp(-qx), & x \geq 0, \\ \left[\cos hx - \dfrac{\zeta q}{h}\sin hx\right], & -L \leq x \leq 0, \\ \left(\cos hL + \dfrac{\zeta q}{h}\sin hL\right)\exp[p(x+L)], & x \leq -L, \end{cases} \qquad (2)$$

where A is the normalization constant, $\zeta = 1$ for TE modes, and $\zeta = \varepsilon_2/\varepsilon_3$ for TM modes. In the case under
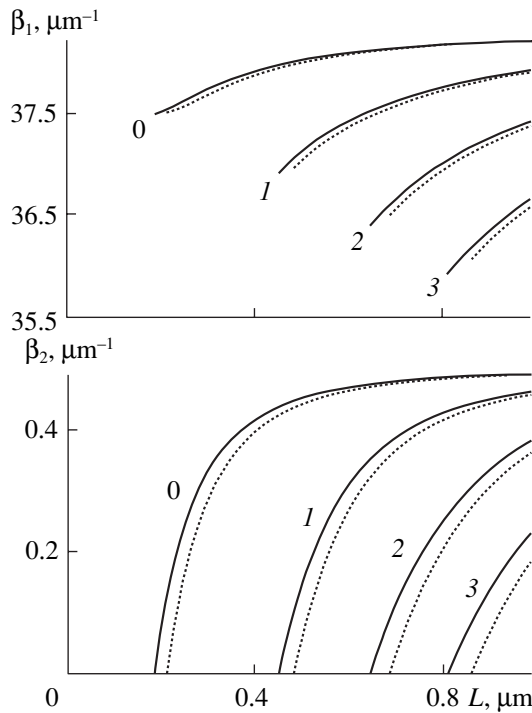
Fig. 1. Plots of the propagation constant β_1 and the mode gain β_2 versus the waveguide layer thickness for the first four TE (solid curves) and TM (dashed curves) modes at $n_2'' = 0.05$.

consideration, the transverse components of the wave vector (p, q, and h) in each layer of the structure are complex quantities whose real and imaginary parts are defined as

$$(p', h', q') = \frac{1}{\sqrt{2}}[(u_j^2 + v_j^2)^{1/2} + u_j]^{1/2},$$

$$(p'', h'', q'') = \pm\frac{1}{\sqrt{2}}[(u_j^2 + v_j^2)^{1/2} - u_j]^{1/2}. \tag{3}$$

Here, the parameters p, q, h correspond to $j = 1$–3, respectively, and

$$u_j = (-1)^j(k_0^2\varepsilon_j' - \beta_1^2 + \beta_2^2), \quad v_j = (-1)^j(k_0^2\varepsilon_j'' - 2\beta_1\beta_2),$$

where $k_0 = \omega/c$ and c is the speed of light in vacuum. For z components of the waveguide mode field, the Maxwell equations yield the following relations: $F_z(x) = \pm i(\gamma(x)k_0)^{-1}dF_y/dx$, where the upper sign and $\gamma(x) = 1$ for all layers of the waveguide structure correspond to the H_z component of the TE modes, while the lower sign and $\gamma(x) = \varepsilon_j$ correspond to the E_z component of the TM modes.

Solution of the problem. For a nonabsorbing waveguide structure, the quantities p, q, and h are real values. In this case, the cutoff condition is expressed as

$p = 0$, whereby the mode is radiated into the substrate. The cutoff waveguide thickness L_c is determined from the dispersion equation obtained using the boundary conditions for the tangential components of the electric and magnetic fields in the structure with $p = 0$. The loss of the waveguide properties also takes place for $h = 0$, in which case trigonometric solutions in the waveguide layer change to hyperbolic. This leads to violation of the continuity condition for the field components with amplitudes decreasing with increasing distance from the waveguide layer.

In the case of the complex parameters p, q, and h, it follows from relations (2) that the waveguide mode is radiated into the substrate for $p' = 0$ and into the coating material for $q' = 0$. Violation of the waveguide properties in the whole structure (by analogy with the absorbing structure) takes place for $h' = 0$. According to expressions (3), these equalities hold provided that $u_j \le 0$ and $v_j = 0$. From this it follows that, in the waveguide regime, the propagation constant and the mode damping obey the following conditions:

$$0 \le \beta_1 \le k_0\sqrt{\frac{|\varepsilon_2| + \varepsilon_2'}{2}}, \quad 0 \le \beta_2 \le k_0\sqrt{\frac{|\varepsilon_2| - \varepsilon_2'}{2}}. \tag{4}$$

The appearance of radiative modes in the substrate and/or coating material takes place for $\beta_2 = 0$ and, respectively,

$$k_0\sqrt{\varepsilon_3} \le \beta_1 \le k_0\sqrt{\varepsilon_1}, \quad 0 \le \beta_1 \le k_0\sqrt{\varepsilon_3} \tag{5}$$

(for certainty, here and below we assume that $\varepsilon_2' > \varepsilon_1$). Thus, the cutoff thickness in a waveguide with gain can be determined by solving a dispersion equation with the parameters p, q, and h corresponding to the above cutoff conditions:

$$h_cL_c = \arctan\left(\frac{\eta p_c}{h_c}\right) + \arctan\left(\frac{\zeta q_c}{h_c}\right) + m\pi. \tag{6}$$

Here, $\eta = 1$ for TE modes and $\varepsilon_2/\varepsilon_1$ for TM modes; $p_c = \sqrt{\beta_1^2 - k_0^2\varepsilon_1}$, $q_c = \sqrt{\beta_1^2 - k_0^2\varepsilon_3}$, and $h_c = \sqrt{k_0^2\varepsilon_2 - \beta_1^2}$ for $\beta_2 = 0$. Equation (6) is complex and can be separated into real and imaginary parts, which yields two equations for the unknown parameters L_c and β_{1c}. These equations possess no analytical solutions and are not presented here due to their being too cumbersome. The results of analysis, performed based on the numerical solution, are presented below in plots of certain waveguide characteristics.

Numerical analysis. For a numerical analysis of the cutoff regime in the waveguide structure under consideration, let us assume for certainty that $\varepsilon_1 > \varepsilon_3$ (this implies the cutoff for a waveguide mode converting

into a radiative mode at the waveguide–substrate interface). The values of the parameters of structure and radiation were selected as follows: $\varepsilon_1 = 14.44$; $\varepsilon_2 = (3.86 + in_2'')^2$, $\varepsilon_3 = 1.00$, and $\lambda = 0.6328$ μm. This set corresponds to a real waveguide structure with a silicon substrate and an active waveguide layer based on doped silicon [10]. The positive and negative signs at n_2'' correspond to the cases of gain and damping, respectively.

Figure 1 presents the plots of the propagation constant and the mode gain for the TE (solid curves) and TM (dashed curves) modes with $m = 0$–3 at an amplification parameter of $n_2'' = 0.05$. As can be seen from these data, the propagation constants at the cutoff thickness β_{1c} for the modes of various orders are different (in contrast to the case of nonabsorbing waveguide). As the mode index increases, the cutoff onset is observed at greater waveguide thickness and smaller propagation constants. This leads to a significant expansion of the region of propagation constants for which the waveguide regimes are realized. At a fixed thickness L of the waveguide, the TE modes exhibit greater values of the propagation constant and gain as compared to those of the TM modes. An analysis shows that an increase in gain in the waveguide layer leads to an increase in the difference $\Delta\beta_{1,2} = \beta_{1,2}^{TE} - \beta_{1,2}^{TM}$ and to the appearance of features in the behavior of the TM mode near the cutoff, whereby the propagation constant increases with thickness L at a slower rate. In addition, radiative modes in a substrate with the given n_2'' appear at a smaller thickness for the TE modes than for the TM modes.

Figure 2 presents the plots of the propagation constant β_{1c} and the waveguide thickness L_c in the cutoff regime as functions of the parameter n_2'' for the TE (solid curves) and TM (dashed curves) modes with $m = 0$–3. The initial values (at $n_2'' = 0$) of the parameters $\beta_{1c} = k_0\sqrt{\varepsilon_1}$ and L_c for all modes correspond to the case of a transparent waveguide structure. As can be seen, these values for the TE modes decrease virtually monotonically with increasing n_2'', the drop being more pronounced for the higher modes. For the TM modes, no such monotonic behavior is observed. The appearance of a break in the $\beta_{1c}(n_2'')$ curve and a step in $L_c(n_2'')$ observed for the TM$_3$ mode is related to the regime of radiative modes in the coating material being approached: $\beta_{1c} = k_0\sqrt{\varepsilon_3}$. An analogous break takes place with increasing n$_2$ for each subsequent TM mode of a lower order. As a result, the TM modes of various orders differing by unity (TM$_2$ and TM$_3$ in Fig. 2b) can possess the same cutoff thickness and different critical propaga-
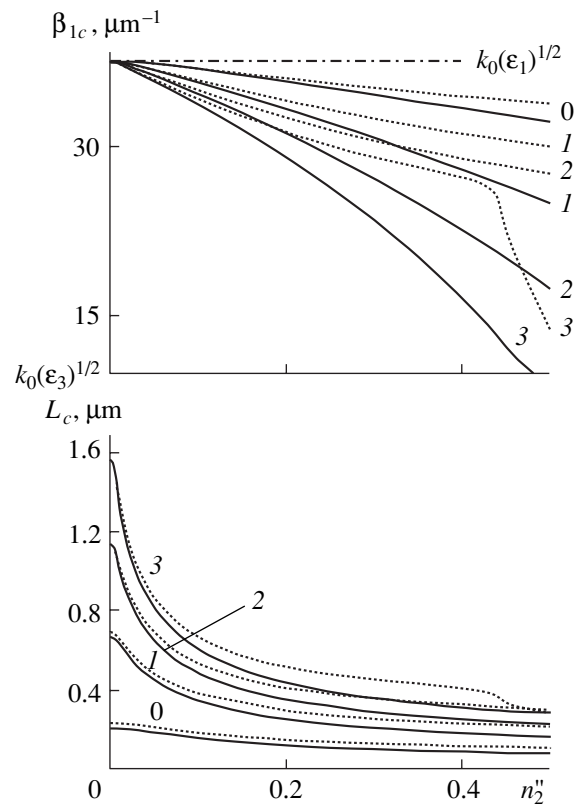

Fig. 2. Plots of the propagation constant β_{1c} and the waveguide thickness L_c in the cutoff regime as functions of the parameter n_2'' for the first four TE (solid curves) and TM (dashed curves) modes.

tion constants β_{1c}. In the case of absorbing waveguide layers ($n_2'' < 0$), the dependences of the propagation and damping constants of various modes on the layer thickness are analogous to those depicted in Fig. 1, except that β_2 acquires negative values. It should also be noted that the interval of values of the parameter n_2'' in Fig. 2 in fact corresponds to the waveguides with absorption. Only the initial parts of these curves describe waveguide structures with gain that are characterized by $n_2'' \ll 1$.

The features of the cutoff regimes observed for both orthogonal mode polarizations in the waveguide structures with amplifying (absorbing) waveguide layers can be used to create active optoelectronic devices based on structures of the insulator–semiconductor–insulator type.

REFERENCES

1. M. Adams, *An Introduction to Optical Waveguides* (Wiley, New York, 1981; Mir, Moscow, 1984).

2. A. Reisinger, Appl. Opt. **12** (5), 1015 (1973).

3. P. V. Adamson, Opt. Spektrosk. **66** (5), 1172 (1989) [Opt. Spectrosc. **66**, 684 (1989)].

4. D. I. Sementsov and A. M. Shutyĭ, Opt. Spektrosk. **81** (1), 153 (1996) [Opt. Spectrosc. **81**, 139 (1996)].

5. D. I. Sementsov, A. M. Shutyĭ, and D. G. Sannikov, Pis'ma Zh. Tekh. Fiz. **25** (21), 8 (1999) [Tech. Phys. Lett. **25**, 849 (1999)].

6. V. G. Fedoseev and P. V. Adamson, Zh. Tekh. Fiz. **51** (12), 2546 (1981) [Sov. Phys. Tech. Phys. **26**, 1503 (1981)].

7. T. D. Visser, H. Blok, and D. Lenstra, IEEE J. Quantum Electron. **31** (10), 1803 (1995).

8. G. Nykolak, M. Haner, and P. Becker, IEEE Photonics Technol. Lett. **5**, 1185 (1993).

9. S. P. Svetlov, V. Yu. Chalkov, and V. G. Shengurov, Pis'ma Zh. Tekh. Fiz. **26** (1), 84 (2000) [Tech. Phys. Lett. **26**, 41 (2000)].

10. X. Zhao, S. Komuro, and H. Isshiki, Appl. Phys. Lett. **74** (1), 120 (1999).

11. K. H. Schlereth and M. Tacke, IEEE J. Quantum Electron. **26** (4), 627 (1990).

12. J. J. Burke, G. I. Stegeman, and T. Tamir, Phys. Rev. B **33** (8), 5186 (1986).

Translated by P. Pozdeev

On the Darcy Law under Enthalpy Conservation Conditions

S. O. Gladkov

Moscow State Pedagogical University, Moscow, Russia
Received April 17, 2002

Abstract—A relation between the Joule–Thomson effect and the Darcy law is established within the framework of a kinetic approach. This relation is of a purely dissipative nature. The dependence of the Joule–Thomson coefficient α_W on the permeating liquid viscosity is studied. © *2002 MAIK "Nauka/Interperiodica".*

During the diffusion saturation of porous structures with a liquid [1], it is possible to realize conditions of the so-called Joule–Thomson effect. Although this effect is considered in every textbook on statistical physics, it is expedient to briefly describe the physical essence of the phenomenon observed.

Consider a cylinder provided with a perfect thermal insulation arbitrarily separated into two compartments by a porous (e.g., paper) spacer, the pressures and temperatures in the left and right compartments being P_1, T_1 and P_2, T_2, respectively. When compressed by a piston, a liquid in the left compartment with a volume of V_1 will slowly permeate through the porous spacer (also referred to as the membrane) into the right compartment, thus increasing its volume V_2. In this system, the dependence of the pressure on the temperature is sharply manifested in both compartments. Introducing the temperature difference $\delta T = T_1 - T_2$ and the pressure difference $\delta P = P_1 - P_2$, we can express the relation between these quantities as $\delta T = \alpha \delta P$. Owing to the smallness of the temperature and pressure variations, the coefficient α can be formally defined as a coefficient of expansion of $T(P)$ in a Taylor series and represented by the partial derivative $(\partial T/\partial P)_W$, where W denotes the enthalpy, which remains constant in the course of the process under consideration. Indeed, since $(\delta E)_{S, V, N} = (\delta \Omega)_{\mu, V, T}$ and $E_1 - E_2 = \Omega_1 - \Omega_2 = P_2 V_2 - P_1 V_1$ (where $\Omega = -PV$), it follows that $E_1 + P_1 V_1 = E_2 + P_2 V_2 = W = \text{const}$.

It is evident that the entropy is not conserved (despite the condition that the cylinder is thermally insulated and the global entropy is conserved), since a real system always features a friction of liquid in the pores of the membrane.

In order to evaluate the derivative $(\partial T/\partial T)_W$, let us pass from the variables (P, W) to a more convenient pair, for example, (P, T). In these terms,

$$\alpha = \alpha_W = (\partial T/\partial P)_W = \frac{\partial(T, W)}{\partial(P, W)}\frac{\partial(T, P)}{\partial(T, P)}$$

$$= \frac{\partial(T, P)}{\partial(P, W)}\frac{\partial(T, W)}{\partial(T, P)} = -(\partial W/\partial P)_T(\partial T/\partial W)_P$$

and we eventually arrive at the formula

$$\alpha_W = (\partial T/\partial P)_W = C_p^{-1}[T(\partial V/\partial T)_p - V].$$

From this expression, it follows that (according to the equation of state $pV = NT$) for the ideal gas the derivative $(\partial V/\partial T)_p = V/T$ and the coefficient α_W is zero. Such a result suggests a relation between the coefficient α_W and the interaction of permeating liquid with the surface of pores. Thus, the Joule–Thomson coefficient α_W represents a purely dissipative characteristic of the irreversible thermodynamic process and must be related to the permeability coefficient K, which enters into the Darcy formula and is dependent on the liquid viscosity η.

The aim of this study is to establish a relation between α_W and K on a strict mathematical level. For this purpose, let us calculate the dissipative function dQ/dt. By definition, $dQ/dt = TdS/dt$, where S is the entropy. Since we are dealing with a classical Boltzmann gas of molecules, a general expression for the entropy through a nonequilibrium distribution function f_p can be written as

$$S = -\frac{\int f_p \ln(f_p/e) d\Gamma}{\int \langle f_p \rangle d\Gamma}, \qquad (1)$$

where $d\Gamma = Vd^3p$ is the element of the phase space volume, $\langle f_p \rangle$ is the equilibrium Boltzmann distribution function,

$$\langle f_p \rangle = \exp\{-\varepsilon_p/T_0\}, \qquad (2)$$

$\varepsilon_p = p^2/2M$ is the translational energy of molecules, and T_0 is the equilibrium temperature.

As can be seen, the volume V does not enter into the final expression. The integral in the denominator of (1) can be readily calculated to yield

$$Z = \int \langle f_p \rangle d^3p = \int_0^\infty \langle f_p \rangle p^2 dp 4\pi = (2\pi M T_0)^{3/2}.$$

By differentiating formula (1) with respect to time, we obtain

$$\dot{S} = -\int \dot{f}_p \ln f_p d^3p / Z. \tag{3}$$

According to the Boltzmann equation, $\dot{f}_p = L\{f_p\}$. Here, $L\{f_p\}$ denotes the collision integral for molecules of a classical gas. In the so-called tau-approximation, $L\{f_p\} = -\delta f_p/\tau_p$, where τ_p is the relaxation time and $\delta f_p = f_p - \langle f_p \rangle$. Using the expression for the total derivative,

$$\dot{f}_p = \partial f_p/\partial t + \mathbf{v}(\partial f_p/\partial \mathbf{r}) + \mathbf{F}(\partial f_p/\partial \mathbf{p}) = -\delta f_p/\tau_p,$$

assuming the force $\mathbf{F}$ acting upon the molecules to be equal to zero, and considering the distribution to be stationary for the times $\delta t \gg \langle \tau_p \rangle$, we obtain a formula for the required correction δf_p,

$$\delta f_p = -\tau_p \mathbf{v} \nabla f_p^*. \tag{4}$$

Here, a quasi-equilibrium distribution is introduced due to the relation

$$f_p^* = \exp\{-(\varepsilon_p - \mathbf{p}\mathbf{V})/T\}, \tag{5}$$

where $\mathbf{V}(\mathbf{r}, t)$ and $T(\mathbf{r}, t)$ are the inhomogeneous distributions of the macroscopic velocity and temperature in the liquid flow.

Relation (4) yields, in a linear approximation with respect to small gradients, the required correction to the equilibrium distribution function:

$$\delta f_p = -(\tau_p \langle f_p \rangle / T_0)$$
$$\times [(\mathbf{p}\nabla)(\mathbf{v}\mathbf{V}) + (\mathbf{v}\nabla T/T_0)(\varepsilon_p - \mathbf{p}\mathbf{V})]. \tag{6}$$

Now, we can return to formula (2). By putting $f_p = \langle f_p \rangle + \delta f_p$, taking the total derivative with respect to time equal to $df_p/dt = df_p^*/dt = -\delta f_p/\tau_p$, and using the known expansion of the natural logarithm into the Taylor series (according to which $\ln(1 + x) \approx x$ for small x), we obtain the following expression for the dissipative function:

$$\dot{Q} = T_0 \dot{S}$$
$$= (T_0/Z)\int (\delta f_p/\tau_p)\ln(\langle f_p \rangle + \delta f_p)d^3p \approx J_1 + J_2, \tag{7}$$

where

$$\begin{cases} J_1 = (T_0/Z)\int (\delta f_p/\tau_p)\ln \langle f_p \rangle d^3p, \\ J_2 = (T_0/Z)\int (\delta f_p^2/\langle f_p \rangle \tau_p) d^3p. \end{cases}$$

Let us consider each of the two terms separately, beginning with J_1. Using expression (6) and taking into account that the equilibrium distribution function is

$\langle f_p \rangle = \exp\{-\varepsilon_p/T_0\}$, we obtain

$$J_1 = (T_0/Z)\int (\delta f_p/\tau_p)\ln \langle f_p \rangle d^3p$$
$$= -(ZT_0)^{-1}\int \langle f_p \rangle \varepsilon_p \{(\mathbf{p}\nabla)(\mathbf{v}\mathbf{V}) + (\mathbf{v}\nabla T)\varepsilon_p/T_0\}d^3p.$$

Upon integration with respect to the angular variables, the second integrand (proportional to the temperature gradient) yields zero. By employing the rule of averaging over the angular variables, according to which $\int v_i p_k (\ldots)d^3p = (\delta_{ik}/3)\int \mathbf{v}\mathbf{p}(\ldots)d^3p$, the first term can be eventually transformed to

$$J_1 = -(\mathrm{div}\mathbf{V}/3ZT_0)\int \mathbf{p}\mathbf{v}\langle f_p \rangle d^3p. \tag{8}$$

Using one of the major equations of hydrodynamics (continuity equation) $\partial \rho/\partial t + \mathrm{div}(\rho\mathbf{V}) = 0$, where ρ is the liquid density, and assuming that the liquid is incompressible, we put $\rho = \mathrm{const}$ and obtain $\mathrm{div}\mathbf{V} = 0$. This result implies that $J_1 = 0$.

Returning to Eq. (7), we obtain

$$\dot{Q} = \int \delta f_p^2 d^3p / \tau_p \langle f_p \rangle.$$

As can be seen, this quantity is non-negative for any value of the parameters (according to the second law of thermodynamics). By substituting solution (6) into this formula, we arrive at

$$\dot{Q} = (ZT_0)^{-1}\int \tau_p \langle f_p \rangle$$
$$\times [(\mathbf{v}\nabla T)(\varepsilon_p - \mathbf{p}\mathbf{V})/T_0 + (\mathbf{p}\nabla)(\mathbf{v}\mathbf{V})]^2 d^3p.$$

By calculating the square of the expression in square brackets and retaining only even powers of the product of $\mathbf{p}$ and $\mathbf{v}$ (odd powers will vanish upon integration with respect to the angular variables), we obtain

$$\dot{Q} = (ZT_0)^{-1}\int \tau_p \langle f_p \rangle \{(\mathbf{v}\nabla T)^2[\varepsilon_p^2 + (\mathbf{p}\mathbf{V})^2]/T_0^2$$
$$+ [(\mathbf{p}\nabla)(\mathbf{v}\mathbf{V})]^2 - 2(\mathbf{v}\nabla T)(\mathbf{p}\mathbf{V})(\mathbf{p}\nabla)(\mathbf{v}\mathbf{V})/T_0\}d^3p. \tag{9}$$

In order to simplify this expression for the dissipative function, we will us the rule of integration (averaging) over the angular variables. Let us introduce $\langle v_i v_k \rangle = (\delta_{ik}/3)v^2$ and $\langle v_i v_k p_n p_m \rangle = v^2 p^2 a(\delta_{ik}\delta_{nm} + \delta_{in}\delta_{km} + \delta_{im}\delta_{kn})$, where a is the unknown coefficient to be determined. This is achieved through convolution with respect to indices i–k and n–m in the left and right sides of the last expression, which yields $a = 1/15$. Thus, we arrive at

$$\dot{Q} = (ZT_0)^{-1}\int \tau_p \langle f_p \rangle \{(v^2\varepsilon_p^2/3T_0^2)(\nabla T)^2 + (p^2v^2/15)$$
$$\times [(\mathrm{div}\mathbf{V})^2 + (\partial V_k/\partial x_i)^2 + (\partial V_k/\partial x_i)(\partial V_i/\partial x_k)]$$
$$- (2p^2v^2/15T_0)[(\mathbf{V}\nabla T)\mathrm{div}\mathbf{V}$$
$$+ \nabla T(\mathbf{V}\nabla)\mathbf{V} + \mathbf{V}(\nabla T\nabla)\mathbf{V}]\}d^3p. \tag{10}$$

This expression is sufficient to establish a relation between the permeability coefficient K in the Darcy law

and the dissipative characteristics of the permeating liquid flow. Taking into account that, in order of magnitude, $\int \mathbf{F} \, d\mathbf{V} \cong \mathbf{F}\mathbf{V} = \dot{Q}$ (see [1]) and ignoring the flow inhomogeneity over distances on the order of the membrane thickness in Eq. (10), we can assume all even derivatives of the flow velocity to be zero. As a result,

$$\mathbf{F}\mathbf{V} = (1/3ZT_0)\int \tau_p v^2 \langle f_p \rangle \{\varepsilon_p^2 (\nabla T)^2 \\ + 0.2p^2[(\nabla T)^2 \mathbf{V}^2 + 2(\mathbf{V}\nabla T)^2]\} d^3p. \quad (11)$$

As for the force $\mathbf{F}$ in the left-hand side of this relation, this value can be estimated as follows. Since $\mathbf{F} = \mathbf{S}(P_1 - P_2) = -\delta|\mathbf{S}|\nabla P$, where $|\mathbf{S}| = S$ is the membrane area, we can approximately write $\mathbf{F}\mathbf{V} = -\delta S\nabla P\mathbf{V}$. At the same time, the permeation rate according to the Darcy law is $\mathbf{V} = -K\nabla P$ and the dissipative function can be expressed as

$$\dot{Q} = \delta S K (\nabla P)^2. \quad (12)$$

By equating (11) and (12), we obtain the relation

$$\delta S K (\nabla P)^2 = (1/3ZT_0)\int \tau_p v^2 \langle f_p \rangle \{\varepsilon_p^2 (\nabla T)^2 \\ + 0.2p^2[(\nabla T)^2 \mathbf{V}^2 + 2(\mathbf{V}\nabla T)^2]\} d^3p. \quad (13)$$

According to the Joule–Thomson effect, the temperature and pressure variations on the two sides of the substrate are related as $\delta T = \alpha_W \delta P$. Rewriting this relation in terms of gradients, we obtain $\nabla T = \alpha_W \nabla P$. By substituting this into the right-hand side of Eq. (13) and assuming that both the flow velocity and temperature gradient possess a single nonzero component—namely, that perpendicular to the membrane plane (coinciding with the xy plane), whereby $\mathbf{V} = (0, 0, V_z)$ and $\nabla T = (0, 0, \partial T/\partial z)$—we eventually arrive at the desired relation,

$$K = (\alpha_W^2/3\delta Z S T_0^3)\int \tau_p v^2 \langle f_p \rangle (\varepsilon_p^2 + 0.6p^2 V_z^2) d^3p. \quad (14)$$

Thus, we have analytically strictly proved (although it was evident from the very beginning) that the permeation rate is related to the entropy of the liquid (more precisely, to the derivative of the entropy with respect to time!) and determined by friction in the pores of the membrane. In turn, the entropy is proportional to the logarithm of the phase space volume ($S = \ln\Delta\Gamma$), from which it follows that the entropy production is $dS/dt = (\Delta\Gamma)^{-1}d(\Delta\Gamma)/dt$. According to the Liouville theorem, the phase space volume $\Delta\Gamma$ is conserved in the absence of collisions, so that $\Delta\Gamma = \Delta\Gamma_{max}$, $dS/dt = 0$ and, hence, $S = S_{max} = \ln(\Delta\Gamma_{max})$. Taking into account the irreversibility of the filtration process, we may now ascertain that the derivative $d(\Delta\Gamma)/dt$ is positive and, with allowance for collisions, the phase space volume increases. For large times ($t \longrightarrow \infty$), this volume tends to acquire the maximum value $\Delta\Gamma_{max}$. Thus, under nonequilibrium conditions, the phase volume decreases at the initial time instant ($t = 0$) and then ($t > 0$) increases.

Owing to the presence of the flow velocity $\mathbf{V}$, the Maxwell distribution function becomes quasi-equilibrium and includes, in addition to the kinetic energy of the translational motion $\varepsilon_p = p^2/2M$, the term $\mathbf{p}\mathbf{V}$ (see above). Thus, the entropy S becomes dependent on the flow velocity $\mathbf{V}$. For this very reason, a derivative of the dissipative function with respect to velocity yields the friction force $\mathbf{F} = \mathbf{F}_{fr}$, which can be expressed as $\mathbf{F} = \partial(TdS/dt)/\partial\mathbf{V}$. This circumstance was employed above to establish a relation between the permeability coefficient and microscopic properties of the liquid (formula (14)).

Returning to formula (14) and employing the gasokinetic approximation, according to which the kinematic viscosity coefficient ν is estimated as $\nu \approx Z^{-1}\int \tau_p v^2 \langle f_p \rangle d^3p$, we can readily establish a relation between K and ν. Indeed, by assuming that $\varepsilon_p \sim T_0$ and $v_T \gg V_z$ (the latter condition allows us to ignore the term $0.6p^2 V_z^2$ as compared to ε_p^2), we obtain

$$K = \alpha_W^2 \nu/3\delta S T_0. \quad (15)$$

In fact, formula (15) reflects a solution of the problem concerning a relation between the permeability coefficient K and the Joule–Thomson coefficient α_W. However, we also planned to find a relation between α_W and the dissipative properties of the membrane, in particular, with friction. In expressing α_W from formula (15), we obtain $\alpha_W = (3KV_pT_0/\nu)^{1/2}$, where $V_p = S\delta$ is the volume of pores. Now let us use the well-known relation $K = A/\eta$, where A can be expressed, for example, via the Slichter formula $A = A_S = m^2 d^2/96(1 - m)$ (d is the diameter of closely packed cylinders in the Slichter model). In denoting the liquid density by ρ, we obtain a dissipative relation for the real Joule–Thomson coefficient:

$$\alpha_W = (md/4\nu)[V_pT_0/2\rho(1 - m)]^{-1/2}. \quad (16)$$

For the ideal liquid (or gas), the interaction between molecules is zero and the relaxation time tends to infinity ($\tau \longrightarrow \infty$). Since the kinematic viscosity $\nu = \tau v_T^2$, we conclude that $\nu \longrightarrow \infty$ and, hence, $\alpha_W = 0$.

Thus, we have (i) found a relation between the Joule–Thomson coefficient and the Darcy law (membrane permeability), (ii) established that α_W is inversely proportional to the square root of viscosity (equation (16)), and (iii) derived a relation between the dissipative function and the friction force.

REFERENCES

1. S. O. Gladkov, *Physics of Porous Structures* (Nauka, Moscow, 1997).

Translated by P. Pozdeev

Copper Nanoparticles Synthesized in Sapphire by Ion Implantation

A. L. Stepanov

Institute of Physics 1, Aachen Technical University, 52056 Aachen, Germany
Kazan Physicotechnical Institute, Russian Academy of Sciences, Kazan, Tatarstan, 420029 Russia
e-mail: anstep@dionis.kfti.knc.ru
Received April 25, 2002

Abstract—Sapphire-based composite layers implanted with 40-keV Cu^+ ions to a total dose of 1.0×10^{17} cm^{-2} at an ion beam current density varied from 2.5 to 10 μA/cm^2 were studied using Rutherford backscattering and optical reflectance methods. The appearance of optical plasma resonance lines in the reflectance spectra indicates that ion implantation allows copper nanoparticles to be synthesized in the subsurface region of the dielectric crystal studied. © *2002 MAIK "Nauka/Interperiodica"*.

Composite materials representing dielectric matrices containing dispersed metal nanoparticles are promising for applications in optoelectronics. An example of such optoelectronic devices is offered by a prototype of an integrated circuit (microchip) in which the function of connecting elements (replacing conventional conductors) is performed by optical waveguides (OWGs) and the signals are transmitted by light [1].

The OWGs can be represented by layers of synthetic sapphire (Al_2O_3) deposited onto semiconducting substrates. The sapphire layer accommodates optical detectors that convert electric signals into light. The focused light beam in a sapphire OWG is generated by a miniature laser and transmitted via optical paths to a high-speed photodetector capable of converting the photon flux into electrons. It is believed that the use of OWGs instead of metal conductors will provide for a 100-fold increase in the rate of data transfer. It is even more important that the use of insulators (sapphire) instead of semiconductors provide for a considerable decrease in the energy consumption [1]. Prototypes of the integrated optoelectronic devices created to date allow controlled data transfer at a rate of up to 1 Gbit/s, with good prospects for increasing the switching rate up to 5 Gbit/s.

An important position among the key elements of dielectric-based OWGs belongs to nonlinear optical switches, which ensure signal conversion at a characteristic time of the laser action of the order of pico- and femtoseconds. As is known [2, 3], insulators containing metal nanoparticles synthesized by the ion implantation method exhibit giant values of the nonlinear cubic permittivity in this range of action times and, hence, can be successfully implemented in integrated optoelectronic devices.

Experience gained from using the ion implantation techniques for various purposes has allowed metal nanoparticles to be successfully synthesized in various glasses and ionic crystals (in particular, in sapphire substrates). The table presents data compiled from available publications on the types of metal nanoparticles and conditions for their formation in Al_2O_3 directly by ion implantation without additional post-implantation treatments (such as thermal or laser annealing). It should be noted that, from the standpoint of the efficiency of manifestation of the nonlinear optical properties by nanoparticles, noble metals are most preferred, especially copper [4]. However, as can be seen from the data in the table, no successful syntheses of copper nanoparticles in the volume of Al_2O_3 have been reported in the literature.

In this context, the purpose of our study was to check for the principal possibility of obtaining composite materials via synthesis of metal nanoparticles in a sapphire substrate through the implantation of copper ions. Although the bombardment of sapphire by copper ions has been studied before, the implantation of high-energy (130 keV–2.1 MeV) copper ions did not led to the nucleation of copper nanoparticles, whereas the subsequent thermal treatment resulted in the formation of copper oxide nanoparticles [16, 17]. Such data are not included in the table. In our experiments, the formation of metal nanoparticles was studied under the conditions of low-energy (<100 keV) ion implantation.

Substrates for the synthesis of composite materials represented Al_2O_3 characterized by high optical transparency in a broad spectral range from ~220 to 900 nm. The substrates were implanted with 40-keV Cu^+ ions to a total dose of 1.0×10^{17} cm^{-2} at an ion beam current density varied from 2.5 to 10 μA/cm^2. The implantation

was effected at room temperature in an ILU-3 implanter at a controlled residual pressure of 10^{-5} Torr. The implanted samples were analyzed by Rutherford back-scattering (RBS) using a beam of 2-MeV ^{4}He$^+$ ions extracted from a Van de Graaf accelerator. The RBS spectra were converted into depth–concentration profiles of implanted copper ions with the aid of a Data Furnace computer program. The optical reflectance spectra in a wavelength range from 350 to 800 nm were measured on a Monolight single-beam optic fiber device using a primary light beam incident at 90° to the sample surface.

Figure 1 shows typical depth–concentration profiles reconstructed from the RBS data for copper ions implanted into the subsurface layer of a sapphire substrate. Both curves, constructed for two values of the primary ion beam current density, reveal a maximum in the copper concentration near the surface, followed by a monotonic decrease in the metal content with a depth up to 60 nm. The features of these profiles and the factors determining such implant distributions were considered elsewhere [18] and will not be dwelled upon here. It should only be noted that a shift in the position of the maximum in the depth–concentration profile observed for a sample irradiated at a greater ion beam
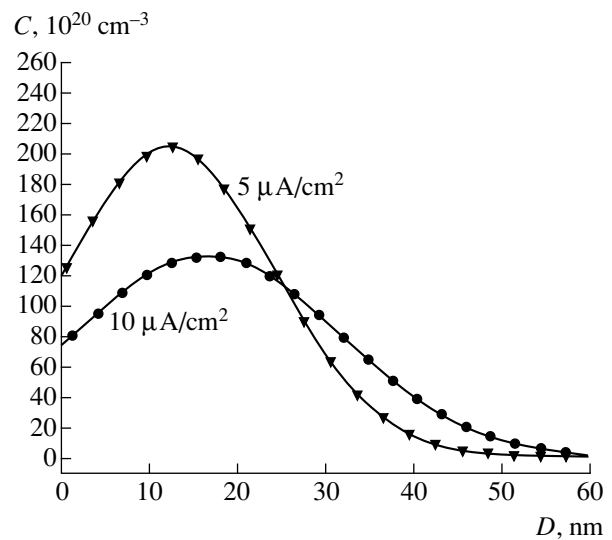

Fig. 1. Profiles (reconstructed from the RBS data) of the atomic concentration C versus depth D for Cu$^+$ ions implanted at various ion beam current densities into sapphire substrates irradiated to a total ion dose of 10^{17} cm^{-2}.

current density is related to a higher temperature of the target and, hence, a greater diffusion mobility of copper in the dielectric matrix.

A summary of data on the types of metal nanoparticles and the conditions of their synthesis in Al$_2$O$_3$ by ion implantation

| Implanted metal	Matrix	Ion beam energy, keV	Ion dose, cm^{-2}	Ion current density, μA/cm^2	Substrate temperature, K	Refs.
α-Fe	α-Al$_2$O$_3$ [0001]	100 160	4×10^{16}–2×10^{17}	–	300 77	McHargue *et al.*, 1987 [5] 1990 [6] 1998 [7]
α-Fe	α-Al$_2$O$_3$ [0001]	160	1×10^{17}	2	300	Sklad *et al.*, 1992 [8]
α-Fe	α-Al$_2$O$_3$ Poly-Al$_2$O$_3$	60	2×10^{16}–1.2×10^{17}	2	–	Jang *et al.*, 1997 [9]
α-Fe	α-Al$_2$O$_3$	100	1×10^{17}	3	300	Sakamoto *et al.*, 1999 [10]
α-Fe	α-Al$_2$O$_3$	160	1×10^{17} 4×10^{17}	–	–	Monteiro *et al.*, 2002 [11]
Co	α-Al$_2$O$_3$ [0001] [0221] [1120]	150	5×10^{17}	–	300	Margues *et al.*, 2001 [12]
Ag	Al$_2$O$_3$	50	5–19×10^{16}	1–5	300 77	Rahmani and Townsend, 1989 [13]
Ag	Al$_2$O$_3$	25–30	2×10^{16}–2×10^{17}	0.6–6.2	300	Steiner *et al.,* 1998 [14]
Pt	Al$_2$O$_3$ [0001]	160	5×10^{16}	0.4	300	Alves *et al.*, 1999 [15]
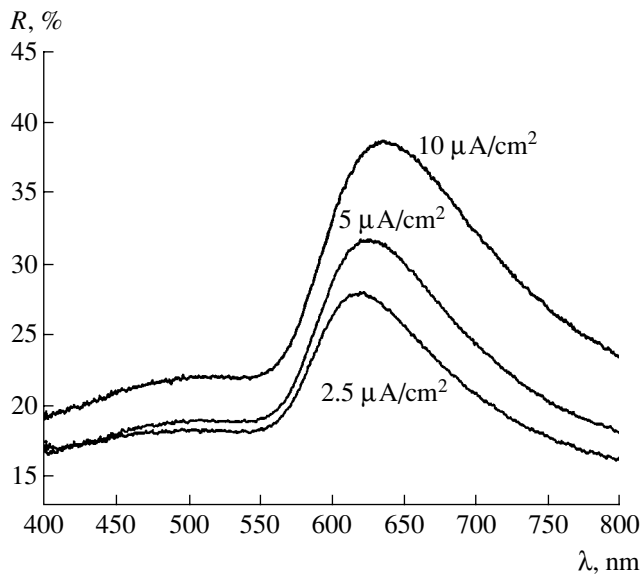
Fig. 2. Optical reflectance spectra of Al_2O_3 substrates implanted with 40-keV copper ions at various ion beam current densities.

During implantation, the concentration of Cu^+ ions in the target exceeds their limiting solubility in Al_2O_3, which leads to the nucleation and growth of metal nanoparticles. Assuming that the metal clusters form as a result of the sequential attachment of Cu^0 (neutralized Cu^+ ions), we may suggest that the growth of nanoparticles is controlled simultaneously by the diffusion coefficient and by the local concentration of copper ions. If the mobility of Cu^0 in the glass matrix is not large, the nanoparticles grow predominantly at the expense of incorporated Cu^+ ions. Since the absolute concentration of metal ions in the implanted layer increases, in accordance with the implant depth–concentration profile, in proportion to the implantation time (or the accumulated ion dose), the process of nanoparticle nucleation and growth is time-dependent as well. It is evident that the dimensions of metal particles formed at various depths are proportional to the factor of glass matrix filling by the metal at the same depths and, hence, are also determined by the implant depth–concentration profile. At the same time, the substrate temperature is another important factor influencing the nucleation and growth of nanoparticles. We may expect coarser metal nanoparticles to form under conditions of elevated target temperature and higher implant mobility.

Figure 2 presents the experimental optical reflectance spectra of the samples obtained by implantation of Cu^+ into Al_2O_3 at various ion beam current densities. Broad selective bands being observed in the visible spectral range is direct evidence of the formation of copper nanoparticles in the bulk of sapphire: these bands are caused by the plasma polariton resonance in

the metal nanoparticles [19]. Preliminary comparative analysis of the electron-microscopic and spectroscopic data for metal particles synthesized by various methods showed that these optical resonances (related to the collective oscillations of free electrons) are manifested in copper particles in the visible spectral range when the particle size exceeds ~2 nm and can be observed in nanoparticles as large as several tens of nanometers [19]. As can be seen from Fig. 2, the position of the maximum in the reflectance spectrum shifts toward longer wavelengths (from 620 to 650 nm) and significantly grows in intensity with increasing ion beam current density. In accordance with the optical properties of small metal particles described by the Mie electromagnetic theory [20], both the wavelength shift and the intensity buildup indicate that increasing the ion beam current leads to a growth of metal nanoparticles in size.

Thus, we have experimentally demonstrated the principal possibility of synthesizing copper nanoparticles in a volume of sapphire substrates at a depth of a several tens of nanometers, which is required for the development of miniature optoelectronic devices. It is shown that the dimensions of the synthesized metal nanoparticles can be controlled by varying the primary ion beam current density in the course of ion implantation. The use of ion implantation for the synthesis of metal nanoparticles, which is widely used in semiconductor technologies, offers a decrease in the general energy consumption during the fabrication of combined optoelectronic microchips based on sapphire–semiconductor compositions.

REFERENCES

1. A. Prieto and A. Andreou, Analog Integr. Circuits Signal Process. **30**, 87 (2002).

2. A. L. Stepanov, I. B. Khaĭbullin, P. D. Townsend, *et al.*, RF Patent No. 2156490 (2000).

3. J. Olivares, J. Requejo-Isidro, R. del Coso, *et al.*, J. Appl. Phys. **90**, 1064 (2001).

4. R. F. Haglund, Jr., L. Yang, R. H. Magruder III, *et al.*, Nucl. Instrum. Methods Phys. Res. B **91**, 493 (1994).

5. C. J. McHargue, G. C. Farlow, P. S. Sklad, *et al.*, Nucl. Instrum. Methods Phys. Res. B **19–20**, 813 (1987).

6. C. J. McHargue, P. S. Sklad, and C. W. White, Nucl. Instrum. Methods Phys. Res. B **46**, 79 (1990).

7. C. J. McHargue, S. X. Ren, and J. D. Hunn, Mater. Sci. Eng. A **253**, 1 (1998).

8. P. S. Sklad, C. J. McHargue, C. W. White, and G. C. Farlow, J. Mater. Sci. **27**, 5895 (1992).

9. H.-G. Jang, H.-B. Kim, J.-H. Joo, *et al.*, Nucl. Instrum. Methods Phys. Res. B **124**, 528 (1997).

10. I. Sakamoto, S. Honda, H. Tanoue, *et al.*, Nucl. Instrum. Methods Phys. Res. B **148**, 1039 (1999).

11. T. Monteiro, C. Boemare, M. J. Saares, *et al.*, Nucl. Instrum. Methods Phys. Res. B (2002) (in press).

12. C. Marques, M. M. Cruz, R. C. da Silva, and E. Alves, Nucl. Instrum. Methods Phys. Res. B **175-177**, 500 (2001).

13. M. Rahmani and P. D. Townsend, Vacuum **39**, 1157 (1989).

14. G. Steiner, M. T. Pham, C. Kuhne, and R. Salzer, Fresenius J. Anal. Chem. **362**, 9 (1998).

15. E. Alves, R. C. da Silva, O. Conde, *et al.*, Nucl. Instrum. Methods Phys. Res. B **146**, 1049 (1999).

16. G. C. Farlow, P. S. Sklad, C. W. White, and C. J. McHargue, J. Mater. Res. **5**, 1502 (1990).

17. M. Ikeyama, S. Nakao, M. Tazawa, *et al.*, Nucl. Instrum. Methods Phys. Res. B **175**-**177**, 652 (2001).

18. A. L. Stepanov, V. I. Zhikharev, and I. B. Khaĭbullin, Fiz. Tverd. Tela (St. Petersburg) **43** (4), 733 (2001) [Phys. Solid State **43**, 766 (2001)].

19. U. Kreibig and M. Vollmer, *Optical Properties of Metal Clusters* (Springer-Verlag, Berlin, 1995).

20. C. F. Bohren and D. R. Huffman, *Absorption and Scattering of Light by Small Particles* (Wiley, New York, 1983; Mir, Moscow, 1986).

Translated by P. Pozdeev

A Method for Constructing Explicit Solutions to Integral Equations with Difference Kernels on Finite Segments

A. M. Radin

e-mail: amradin@mail.ru
Received April 22, 2002

Abstract—A method for constructing explicit solutions of integral equations with difference kernels on finite segments is proposed. Equations with kernels of sufficiently general type are considered. The method opens a promising direction for the investigation and practical application of solutions for this class of equations. © 2002 MAIK "Nauka/Interperiodica".

The integral equations with difference kernels on finite segments can be represented as

$$\int_a^b K(x-t)g(t)dt = \lambda g(x) + f(x), \quad x \in [a, b],$$

where $K(x) \in L_1(a, b)$. Such equations have been derived for a number of problems in physics and technologies, including the problems of optimum synthesis, light scattering in the atmosphere, diffraction from a ribbon, a cylinder with a slit, a sphere with holes [1], and the motion of a wing under water. These equations are also encountered in solving important mathematical problems such as the theory of inverse problems, reduction of the Volterra operators to the simplest form, and factorization of operators. Thus, the equations with difference kernels are rather widely applied. Extensive literature on related questions is cited in review [2] and in monograph [3].

Here, we will consider an equation of the first kind:

$$\int_a^b K(x-t)g(t)dt = f(x), \quad x \in [a, b]. \quad (1)$$

To date, the most complete results for Eq. (1) were published in [3]. According to this monograph, for Eq. (1) with an arbitrary right-hand part $f(x)$, $g(t)$ can be expressed by an explicit formula, provided that a solution to this equation is known for $f(x) = 1$. Unfortunately, the problem of constructing an explicit solution to Eq. (1) with $f(x) = 1$ has not yet been solved. This gap is filled, to a certain extent, by this paper, which proposes a method of constructing an explicit solution to Eq. (1) in a sufficiently general situation. According to this, there is no need to assume that $f(x) = 1$. For the

sake of brevity, Eq. (1) can be transformed through a linear change of variables to the following form:

$$\int_{-\pi/2}^{\pi/2} K(x-t)g(t)dt = f(x), \quad x \in [-\pi/2, \pi/2]. \quad (2)$$

We assume that $K(z)$ can be represented on the segment $[-\pi, \pi]$ by the Fourier series

$$K(z) = \sum_n k_{n-\frac{1}{2}} \exp\left[i\left(n-\frac{1}{2}\right)z\right], \quad z \in [-\pi, \pi], \quad (3)$$

$$k_{n-\frac{1}{2}} = \frac{1}{2\pi}\int_{-\pi}^{\pi} K(z)\exp\left[-i\left(n-\frac{1}{2}\right)z\right]dz, \quad (4)$$

where the quantities $k_{n-\frac{1}{2}}$ for large n can be estimated as

$$k_{n-\frac{1}{2}} = O\left(\left(n-\frac{1}{2}\right)^{-m-\alpha}\right), \quad (5)$$

$$m = 0, 1, 2\ldots, \quad 0 \le \alpha < 1, \quad m + \alpha \ne 0.$$

By substituting expression (3) into Eq. (2) and integrating, we arrive at the following form of the initial equation:

$$\sum_n k_{n-\frac{1}{2}} \exp\left[i\left(n-\frac{1}{2}\right)x\right] \int_{-\pi/2}^{\pi/2} g(t)\exp\left[i\left(n-\frac{1}{2}\right)t\right]dt = f(x), \quad (6)$$

$$x \in \left[-\frac{\pi}{2}, \frac{\pi}{2}\right].$$

In using estimate (5), Eq. (6) can be differentiated m

times ($m = 0, 1, 2, \ldots$), which yields

$$\sum_n \left[i\left(n - \frac{1}{2}\right)\right]^m k_{n-\frac{1}{2}} \exp\left[i\left(n - \frac{1}{2}\right)x\right] g_n = \frac{1}{\pi} f^{(m)}(x), \quad (7)$$

$$x \in \left[-\frac{\pi}{2}, \frac{\pi}{2}\right],$$

where

$$g_n = \frac{1}{\pi} \int_{-\pi/2}^{\pi/2} g(t) \exp\left[-i\left(n - \frac{1}{2}\right)t\right] dt \qquad (8)$$

are unknown coefficients. Introducing the notation

$$\left[i\left(n - \frac{1}{2}\right)\right]^m k_{n-\frac{1}{2}} = x_n, \quad x_n g_n = y_n, \qquad (9)$$

we can rewrite Eq. (7) as

$$\sum_n y_n \exp\left[i\left(n - \frac{1}{2}\right)x\right] = \frac{1}{\pi} f^{(m)}(x), \quad x \in \left[-\frac{\pi}{2}, \frac{\pi}{2}\right]. (10)$$

Finally, after introduction of the variable

$$\xi = \exp(ix), \qquad (11)$$

Eq. (10) takes the form

$$\sum_n y_n \xi^n = \frac{1}{\pi} f^{(m)}(arg\xi) \exp\left(\frac{i}{2} arg\xi\right) = F(\xi), \qquad (12)$$

$$\xi \in L,$$

where L is a right-hand semicircle of unit radius (see figure). Equation (12) with unknown coefficients y_n is readily reduced to the classical Riemann problem [4] on the arc L by representing the series in (12) as a sum of two functions, $\Phi^+(\xi)$ and $\Phi^-(\xi)$, representing limiting values of a certain analytical function $\Phi(z)$ outside and inside a unit circle, respectively:

$$\Phi^+(\xi) + \Phi^-(\xi) = F(\xi), \quad \xi \in L. \qquad (13)$$

The choice of functions $\Phi^+(\xi)$ and $\Phi^-(\xi)$ uniquely determines the behavior of the solution $\Phi(z)$ to the Riemann problem at infinity. Both the existence of a solution $g(t)$ to this equation and its behavior in the vicinity of ends ($t = \pm\pi/2$) of the finite integration interval depend on this selection and on the character of decay of the Fourier coefficients (5) of the kernel of the initial equation (1). As a rule, all these conditions are well known, being determined by the physical or mathemat-
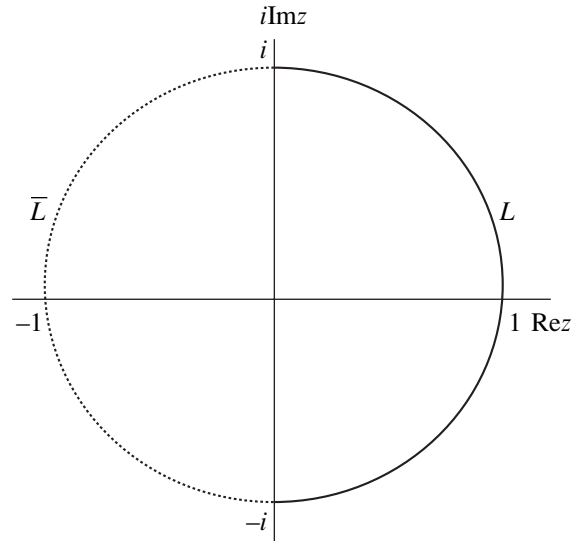

Figure.

ical problem reduced to Eq. (1). In particular, for the solutions $\Phi(z)$ limited at infinity, the functions $\Phi^+(\xi)$ and $\Phi^-(\xi)$ should be selected in the following form:

$$\Phi^+(\xi) = \sum_{n \geq 1} y_n \xi^n, \quad \Phi^-(\xi) = \sum_{n < 1} y_n \xi^n, \quad \xi \in L. (14)$$

For the solutions tending to zero at infinity, these functions should take the form

$$\Phi^+(\xi) = \sum_{n \geq 0} y_n \xi^n, \quad \Phi^-(\xi) = \sum_{n < 0} y_n \xi^n, \quad \xi \in L. (15)$$

It should be noted that other conditions can be selected as well, for example, for $\Phi(z)$ possessing poles either in the unit circle or at infinity. Of course, the course of action can be reversed, whereby the behavior of the solution $g(t)$ at the ends of the integration interval can be determined and the solutions to Eq. (2) can be studied by selecting $\Phi(z)$ with the appropriate behavior at infinity in the Riemann problem (13). Since this problem has been well studied [4–6], choice of the appropriate variant for representing series (12) as a sum of two functions $\Phi^+(\xi)$ and $\Phi^-(\xi)$ for the Riemann problem (13) is quite possible.

For example, let us find solutions to Eq. (2) for the functions $\Phi^+(\xi)$ and $\Phi^-(\xi)$ adopting representation (15). This case corresponds to finding a solution to the Riemann problem (13) that would tend to zero at infinity. According to [4–6], this solution has the form

$$\Phi(z) = \Phi_0^{(s)}(z)\left[\frac{1}{2\pi i}\int_L \frac{F(\xi)}{\Phi_0^{(s)}(\xi)}\frac{d\xi}{\xi - z} + C\delta_s^1\right], \qquad (16)$$

where C is an arbitrary constant, δ_s^1 is the Kronecker delta, and $\Phi_0^{(s)}(z)$ ($s = 1$–4) are solutions to the corresponding homogeneous Riemann problems:

$$\Phi_0^{(1)}(z) = \frac{1}{\sqrt{z^2+1}}, \quad \Phi_0^{(2)}(z) = \sqrt{z^2+1},$$

$$\Phi_0^{(3)}(z) = \sqrt{\frac{z+i}{z-i}}, \quad \Phi_0^{(4)}(z) = \sqrt{\frac{z-i}{z+i}}. \tag{17}$$

In the case of $s = 2$, the function $F(\xi)$ must obey the condition

$$\int_L \frac{F(\xi)}{\sqrt{z^2+1}} d\xi = 0. \tag{18}$$

In all formulas, the square root branch is determined by being positive at infinity.

After application of the Sokhotsky formulas [4–6], representation of $\Phi(z)$ in the form of (16) allows the series (12) to be restored on the entire circle $L + \bar{L}$ (see figure) for all the cases under consideration ($s = 1$–4):

$$\sum_n y_n^{(s)} \xi^n = F(\xi), \quad \xi \in L,$$

$$\sum_n y_n^{(s)} \xi^n = \Phi_0^{(s)}(\xi) \left[\frac{1}{\pi i} \int_L \frac{F(\tau)}{\Phi_0^{(s)}(\tau)} \frac{d\tau}{\tau - \xi} + C\delta_s^1 \right], \tag{19}$$

$$\xi \in \bar{L} \ (s = 1, 2, 3, 4).$$

From (19), we find the coefficients $y_n^{(s)}$, and then, by using (9), we obtain the Fourier coefficients $g_n^{(s)}$ for the function $g(t)$ representing a solution to the initial equation (2). In the example under consideration, we obtain four sets of the coefficients for $g_n^{(s)}$ ($s = 1$–4):

$$g_n^{(s)} = \frac{1}{2\pi \left[i\left(n - \frac{1}{2}\right) \right]^m k_{n-\frac{1}{2}}} \left[\int_L F(\xi)\xi^{-n-1} d\xi \right.$$

$$+ \frac{1}{\pi i} \int_{\bar{L}} \Phi_0^{(s)}(\xi) \xi^{-n-1} d\xi \left(\int_L \frac{F(\tau)}{\Phi_0^{(s)}(\tau)} \frac{d\tau}{\tau - \xi} + C\delta_s^1 \right) \right] \tag{20}$$

$$(s = 1, 2, 3, 4).$$

It should be noted that, if some of the Fourier coefficients $k_{n-\frac{1}{2}}$ of the kernel of the initial equation turn zero, this can be readily taken into account in posing the Riemann problem (13) and these quantities will not be present in formula (20). Based on representation (8), solutions to the initial equation (2) can be written using one of the following formulas:

$$g^{(s)}(t) = \sum_n g_{2n}^{(s)} \exp\left[i\left(2n - \frac{1}{2}\right)t \right]$$

$$= \sum_n g_{2n+1}^{(s)} \exp\left[i\left(2n - \frac{1}{2}\right)t \right] = \frac{1}{2} \sum_n g_n^{(s)} \exp\left[i\left(n - \frac{1}{2}\right)t \right], \tag{21}$$

$$t \in \left(-\frac{\pi}{2}, \frac{\pi}{2} \right) \ (s = 1, 2, 3, 4),$$

where the coefficients $g_n^{(s)}$ are determined by expressions (20).

Let us estimate the convergence of series (21). As is known [4], a special integral over the arc L entering into formula (20) has a finite value at the ends of arc L. Therefore, the convergence of series (21) is determined by the behavior of functions (17) from the homogeneous Riemann problem in the vicinity of the ends of arc L and by the exponent α from the estimate (5) of the decay of the Fourier coefficients of the kernel of the initial equation (2). As a result, we obtain the following estimate:

$$g_n^{(s)} = O\left(n^{\alpha - \frac{1}{2}}\right), \quad 0 \le \alpha < \frac{1}{2} \ (s = 1, 3, 4); \tag{22}$$

$$g_n^{(2)} = O\left(n^{\alpha - \frac{3}{2}}\right), \quad 0 \le \alpha < 1. \tag{23}$$

Thus, Eq. (2) for $s = 1$ has a single integrable solution $g(t)$ unlimited at the ends of the interval $t = \pm\pi/2$, provided that the exponent α obeys the conditions in (22). For $s = 2$, the solution is limited at the ends of the interval for $0 \le \alpha < 1/2$ and is unlimited for $1/2 < \alpha < 1$. In the case of $s = 2$, the right-hand part must also satisfy the condition of solvability (18). For $s = 3$ and 4, the solution is limited in the vicinity of one end of the interval and unlimited at the other end, while the exponent α must obey the same conditions as in (22).

In conclusion, it should be pointed out that the proposed method allows explicit solutions to be constructed for equations with arbitrary kernels admitting representation (3)–(5) on a finite interval. The results known to date (the primary of which are considered in [2–4]) represent particular cases of the proposed method. For example, consider the equation

$$\int_{-\pi/2}^{\pi/2} \ln\left| 2\sin\frac{x-t}{2} \right| g(t)dt = -1, \quad x \in [-\pi/2, \pi/2]. \tag{24}$$

According to [3], this equation possesses the explicit solution $g(t) = \text{const}/\sqrt{\cos(t)}$, which can be checked directly. Let us apply the proposed method to this problem. By calculating the Fourier coefficients of the ker-

nel in (24) according to (4), where the integral can be explicitly calculated, we obtain

$$k_{n-\frac{1}{2}} = -\frac{1}{2\pi} \int_{-\pi}^{\pi} \ln\left|2\sin\frac{t}{2}\right| \exp\left[i\left(n-\frac{1}{2}\right)t\right] dt$$

$$= \frac{(-1)^n 2\ln 2}{\pi(2n-1)}, \quad n = 0, \pm 1, \pm 2, \dots. \tag{25}$$

Thus, we have $m = 1$, $\alpha = 0$, $f(x) = 1$, and $F(x) = 0$. A solution corresponding to $s = 1$ will be unlimited at the ends of the interval $t = \pm\pi/2$. Upon substituting the Fourier coefficients of the kernel from (25) into (20) and (21), we obtain the same result as above: $g(t) = \text{const}/\sqrt{\cos(t)}$.

Acknowledgments. The author is grateful to V.M. Babich, A.B. Plachenov, and other participants of the diffraction seminar at the Steklov Institute (POMI-RAN) for helpful discussions.

REFERENCES

1. A. M. Radin and V. P. Shestopalov, Dokl. Akad. Nauk SSSR **212** (4), 838 (1973) [Sov. Phys. Dokl. **18**, 642 (1973)].
2. L. A. Sakhnovich, Usp. Fiz. Nauk **35** (4), 69 (1980).
3. I. Ts. Gokhberg and M. G. Kreĭn, *Theory of Volterra Operators in Hilbert Space and Its Applications* (Nauka, Moscow, 1967).
4. F. D. Gakhov, *Boundary Value Problems* (Fizmatgiz, Moscow, 1963; Addison-Wesley, Reading, 1966).
5. F. D. Gakhov and Yu. I. Cherskiĭ, *Convolution Equation* (Nauka, Moscow, 1978).
6. F. D. Gakhov, *Boundary Value Problems* (Nauka, Moscow, 1977).

Translated by P. Pozdeev

New Values of the Ag–*n*-GaP Potential Barrier

A. N. Pikhtin, S. A. Tarasov, and B. Kloth

St. Petersburg State Electrotechnical University, St. Petersburg, Russia
e-mail: ANPikhtin@mail.eltech.ru
Received May 22, 2002

Abstract—Surface-barrier structures of the Ag–GaP type based on high-quality epitaxial *n*-GaP layers with $n = (0.5–30) \times 10^{16}$ cm^{-3} were studied. It was found that the potential barrier height depends on the method of surface treatment prior to the metal deposition and correlates with the structural nonideality coefficient and the intermediate layer thickness. For high-quality structures with a reverse current below 10^{-14} A, the barrier height is $\varphi = 1.55 \pm 0.04$ eV. For structures with a relatively thick intermediate layer, the barrier may reach up to $\varphi = 1.7 \pm 0.07$ eV. The dependence of the barrier height on the method of the GaP surface treatment is related to the absence of rigid pinning of the Fermi level on the GaP surface. © *2002 MAIK "Nauka/Interperiodica".*

Surface-barrier structures of the metal–gallium phosphide type are of considerable interest for applications, primarily due to the large bandgap width in GaP ($E_g = 2.27$ eV at 300 K) and good technological properties of this material. While the surface barrier height in silicon- and gallium arsenide-based metal–semiconductor structures weakly depends on the metal type [1], the situation in metal–GaP structures is different. It is believed that the maximum potential barrier height is achieved in Pt–*n*-GaP (1.45 eV) and Au–*n*-GaP (1.36 eV) structures, while the value reported for the Ag–*n*-GaP system is 1.2 eV [2]. For this reason, the latter system is less interesting from the standpoint of the development of electronic devices for high-temperature and high-power applications, shortwave photodetectors (Schottky UV photodiodes), etc.

Below we will demonstrate that, in contrast to the commonly accepted opinion, the potential barrier height of Ag–*n*-GaP structures is essentially greater than that of the Pt–*n*-GaP structure, which makes the former system preferable for the aforementioned applications.

Sample structures of the Me–GaP type (Me = Ag, Pt, Au) were prepared by vacuum deposition (Ag, Au), ion-plasma sputtering (Pt), and magnetron sputtering (Pt, Ag) of a metal after preliminary ion-sputter cleaning of a semiconductor substrate surface. The main experiments were performed with epitaxial *n*-GaP layers grown by liquid- or vapor-phase epitaxy; the epitaxial layers were usually doped with sulfur (in some cases with tellurium) to a free charge carrier concentration of $(0.5–5) \times 10^{16}$ cm^{-3}. The ohmic contacts in the base region were fabricated using laser techniques [3] or by vacuum deposition of gold according to the standard procedure.

The longwave photosensitivity threshold of the sample structures was well described by the relationship

$$\sqrt{I_{ph}} \sim (\hbar\omega - \varphi), \qquad (1)$$

which offered the possibility of determining the surface barrier height φ with a high precision, as illustrated in Fig. 1. The reverse current reached 10^{-14} A at $V = 1$ V. The direct branch of the current–voltage characteristic obeyed the exponential law

$$I \sim \exp(eU/\beta kT), \qquad (2)$$

for the current varied within six orders of magnitude (for the best samples). The structural nonideality coefficient β was found to vary from 1.05 to 5, depending both on the method of contact preparation and on the surface processing technique. We suggested that this scatter could be explained by the presence of an inter-
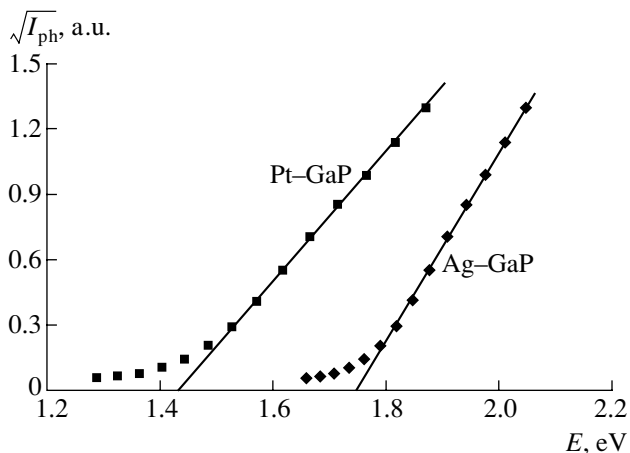

Fig. 1. Determination of the potential barrier height from the photoelectric measurements.

mediate (transition) layer between the metal and semiconductor. For most methods employed for fabricating metal–semiconductor structures, the appearance of such interlayers cannot be avoided in practice.

In order to verify the hypothesis, we studied the depth-composition profiles of the surface of several samples treated by various methods. The profiles were obtained by measuring the Auger electron spectra in the course of layer-by-layer etching of the samples by argon ions to a total depth of 35 nm. An analysis of the Auger spectra showed that the samples upon preliminary mechanochemical polishing were characterized by the most perfect semiconductor surface and by a minimum thickness of the intermediate layer (about 3 nm). The structures treated by other methods exhibited intermediate layers with a thickness of 10 nm or greater.

There was a certain correlation between the intermediate layer thickness, the nonideality coefficient β, and the reverse dark current. As mentioned above, the structures of highest quality were obtained using the method of mechanochemical polishing, in which the intermediate layer thickness was below 3 nm and the nonideality coefficient was $\beta = 1.1$–1.2. For the samples prepared by etching in *aqua regia* (HF + NHNO$_3$ mixture), the intermediate layer was 3–5-nm thick and the nonideality coefficient increased to $\beta = 1.6$–1.8. The samples prepared by magnetron sputtering were characterized by β values as large as 3–5 and dark currents of 1 nA or greater.

It was found that the height of the Ag–GaP potential barrier also depends on the technology of structure preparation and exhibits a correlation with the nonideality coefficient (and, hence, with the intermediate layer thickness). The results of these measurements are summarized in Fig. 2. As is seen, an increase in β is accompanied by a clear growth in the reverse (dark) current. The values of the potential barrier height usually fall within one of three spots, corresponding to the three methods of surface treatment. The average levels of ϕ for these groups are indicated by dashed lines in Fig. 2. The samples upon mechanochemical polishing possessed nonideality coefficients close to unity and showed minimum values of the dark current (about 10 fA). For these samples, the potential barrier height in the Ag–GaP structure amounted to 1.55 ± 0.04 eV.

The structures with an etched surface of the epitaxial layer probably contained a maximum amount of defects at the metal–semiconductor boundary, which accounted for an increase in the reverse current of up to 10^{-13} A. The barrier height in these samples was 1.7 ± 0.07 eV. We believe that the difference in ϕ observed for the samples treated by various methods is indicative
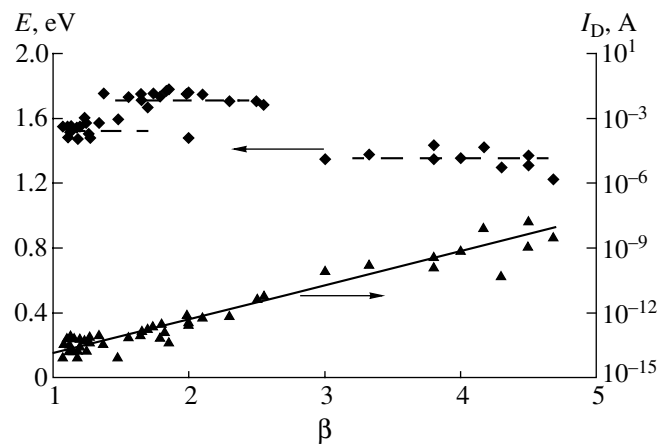

Fig. 2. Plots of the potential barrier height and reverse dark current versus nonideality coefficient for the Ag–GaP structures.

of the absence of rigid pinning of the Fermi level on the GaP surface.

Since the values of ϕ presented above for the Ag–GaP structures studied here significantly differ from the published value of $\phi = 1.2$ eV obtained more than three decades ago and commonly accepted as a reference value, we undertook control measurements of the barrier height in well-characterized platinum–gallium phosphide contacts. According to the data obtained by various researchers, the potential height of the Pt–GaP barrier is 1.45 eV [2–4]. Our measurements yielded 1.45 ± 0.02 eV (Fig. 1), which fully agrees with the published data.

In the sample structures with thick intermediate layers, a large nonideality coefficient β, and a reverse current of 1 nA or greater, the ϕ values decreased to 1.35 eV (to fall within the third spot in Fig. 2). The structures based on *n*-GaP with $n > (2$–$3) \times 10^{17}$ cm^{-3} possessed low quality and showed ϕ as low as ≈ 1.2 eV, which probably explains the low values reported previously.

REFERENCES

1. Z. Chen and W. Kim, J. Appl. Phys. **74** (3), 3634 (1994).
2. S. Sze, *Physics of Semiconductor Devices* (Wiley, New York, 1981; Mir, Moscow, 1984).
3. A. N. Pikhtin, V. A. Popov, and D. A. Yas'kov, Prib. Tekh. Éksp. **2**, 238 (1970).
4. B. V. Tsarenkov, Yu. A. Gol'dberg, A. P. Izergin, *et al.*, Fiz. Tekh. Poluprovodn. (Leningrad) **6** (4), 710 (1972) [Sov. Phys. Semicond. **6**, 610 (1972)].

Translated by P. Pozdeev

Electron Transitions and Radiation of Atoms Interacting with Ultrashort Electromagnetic Pulses

V. I. Matveev

Pomorskiĭ State University, Arkhangelsk, Russia
e-mail: matveev.victor@pomorsu.ru
Received May 15, 2002

Abstract—Excitation and ionization of an atom interacting with a short electromagnetic pulse is studied within the framework of the sudden perturbation approximation. The excitation and ionization probabilities and the spectra and cross sections of reradiation of the pulse by the atom are calculated. It is suggested that the process of reradiation of ultrashort electromagnetic pulses by multielectron atoms possesses a coherent character. © 2002 MAIK "Nauka/Interperiodica".

Recently, Kaplan and Shkolnikov [1] reported on the possibility of generating electromagnetic pulses with a duration of $\tau \sim 10^{-21}$–10^{-22} s. This opens new prospects for investigation of the interaction of ultrashort electromagnetic pulses with matter. In this context, it is important to study the interaction of atoms with ultrashort pulses of a strong electromagnetic field. It should be noted that a nonperturbative description of the interaction of atoms with field pulses of a duration comparable with (or exceeding) the characteristic atomic times presents a difficult task and requires application of numerical methods. An example is offered by the study [2] of the excitation and ionization of atoms interacting with a strong pulsed electromagnetic field at a pulse duration of 3.8–15.2 fs (see also [3–6] and references therein).

In the systems considered above, the characteristic atomic time $\tau_\alpha \sim 10^{-17}$ s is much greater than the duration of the aforementioned ultrashort pulses. In such cases, a basis for the solution can be provided by the approximation of sudden perturbations [7], which poses no restrictions on the magnitude of perturbation and is applicable provided that $\tau/\tau_a \ll 1$. There are numerous examples when atoms are excited or ionized under the action of sudden perturbations. In many of the practically important cases, the perturbation is insufficiently small for the perturbation theory to apply; however, there are also many cases [7–17] when the perturbation duration is much shorter than the characteristic atomic times. This makes it possible to solve the problem using analytical methods without posing limitations on the magnitude of perturbation.

We have used the sudden perturbation approximation to study the excitation and ionization of an atom interacting with a short electromagnetic pulse. The excitation and ionization probabilities and the spectra and cross sections of reradiation of the pulse by the atom are calculated.

The potential of interaction of the atomic electrons with an electromagnetic field pulse possessing a Gaussian shape

$$\mathbf{E} = \mathbf{E}_0 \exp\{-\alpha^2 t^2\} \cos(\omega_0 t) \qquad (1)$$

can be written as follows (here and below, we use the atomic system of units):

$$V(t) \equiv V(\mathbf{r}_a, t) = \mathbf{E}(t) \sum_{a=1}^{a=N} \mathbf{r}_a. \qquad (2)$$

Here, $\mathbf{r}_a$ are the coordinates of atomic electrons ($a = 1, 2, \ldots, N$) and N is the number of atomic electrons. The function $V(t)$ differs from zero only during a time period of $\tau \sim \alpha^{-1}$, which is much shorter than the characteristic periods of an unperturbed atom described by a Hamiltonian H_0. Then, in solving the Schrödinger equation, we can ignore evolution of the wave function under the action of unperturbed Hamiltonian during the perturbation action. Therefore, the amplitude of transition of the atom from an initial state φ_0 to a certain final state φ_n as a result of the sudden perturbation is [7]

$$a_{0n} = \left\langle \varphi_n \left| \exp\left\{ -i \int_{-\infty}^{+\infty} V(t) dt \right\} \right| \varphi_0 \right\rangle, \qquad (3)$$

where φ_0 and φ_n belong to a complete orthonormalized system of eigenfunctions of the unperturbed Hamiltonian H_0, so that $H_0\varphi_n = \varepsilon_n \varphi_n$. Using formula (3), it is possible to calculate the probabilities $w_{0n} = |a_{0n}|^2$ of the excitation or ionization of the perturbed atom. Representation of the perturbation in the form of potential (2)

allows the probabilities w_{0n} to be expressed through well-known inelastic atomic formfactors [9]:

$$w_{0n} = \left| \left\langle \varphi_n \left| \exp\left\{-i\mathbf{q}\sum_a \mathbf{r}_a\right\} \right| \varphi_0 \right\rangle \right|^2, \qquad (4)$$

where

$$\mathbf{q} = \int_{-\infty}^{+\infty} dt \mathbf{E}(t) = \frac{\sqrt{\pi}}{\alpha}\mathbf{E}_0 \exp\left\{-\frac{\omega_0^2}{4\alpha^2}\right\}.$$

Figure 1 presents data on the excitation probabilities for several initial levels and on the total ionization probability of a hydrogen atom calculated as functions of the momentum transfer $\mathbf{q}$. Figure 2 shows the results of our calculations of the single and double ionization probabilities for a helium atom. These figures also illustrate unitarity of the approach following from expressions (4), according to which $\sum_n = 1$, where the summation is performed over all possible final states of the atom.

The cross sections for reradiation of the sudden pulse of a strong electromagnetic field can be calculated using the following procedure. In the sudden perturbation approximation, evolution of the initial state is described by the function

$$\Psi_0(t) = \exp\left\{-i\int_{-\infty}^{t} V(t')dt'\right\}\varphi_0 \qquad (5)$$

satisfying the equation

$$i\frac{\partial\Psi_0(t)}{\partial t} = V(t)\Psi_0(t) \qquad (6)$$

and obeying the condition $\Psi_0(t) \longrightarrow \varphi_0$ for $t \longrightarrow -\infty$. Let us also introduce a total orthonormalized system of functions

$$\Phi_n(t) = \exp\left\{i\int_{t}^{+\infty} V(t')dt'\right\}\varphi_n \qquad (7)$$

satisfying Eq. (6) and obeying the condition $\Phi_n(t) \longrightarrow \varphi_n$ for $t \longrightarrow +\infty$. Obviously, the transition amplitude (3) can be rewritten as $a_{0n} = \langle\Phi_n(t)|\Psi_0(t)\rangle$. The amplitude of photon emission will be calculated in the first order of perturbation theory (as corrections to states (5) and (7)) for the interaction U between atomic electrons and the electromagnetic field [18]. The sudden perturbation $V(t)$ is taken into account by functions $\Phi_n(t)$ and $\Psi_0(t)$ (without limitations on the magnitude of V):

$$U = -\sum_{a,\mathbf{k},\sigma} \left(\frac{2\pi}{\omega}\right)^{1/2} \mathbf{u}_{\mathbf{k},\sigma}(a_{\mathbf{k},\sigma}^+ \exp\{-i(\mathbf{k}\mathbf{r}_a)\}$$
$$+ a_{\mathbf{k},\sigma}\exp\{i\mathbf{k}\mathbf{r}_a\}) \cdot \widehat{\mathbf{p}}_a, \qquad (8)$$
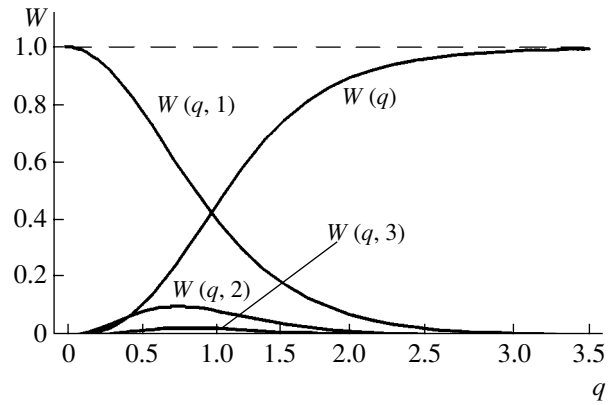

Fig. 1. The results of calculations for hydrogen atom: $W(q, 1)$, the probability of staying in the ground state; $W(q, 2)$ and $W(q, 3)$, the probabilities of excitation to the states with $n = 2$ and 3, respectively; $W(q)$, total ionization probability.
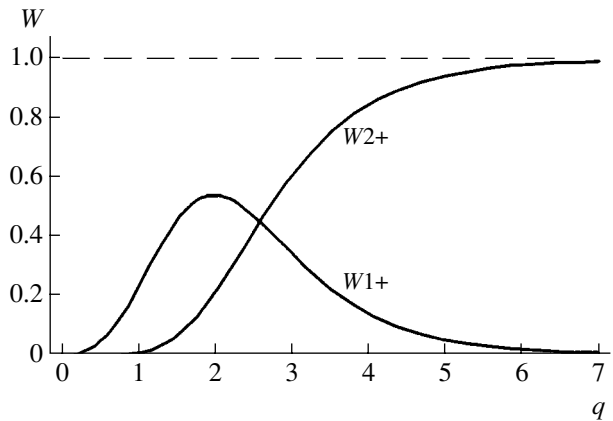

Fig. 2. Calculated probabilities of the single ($W1+$) and double ($W2+$) ionization of a helium atom.

where $a_{\mathbf{k},\sigma}^+$ and $a_{\mathbf{k},\sigma}$ are the operators of creation and annihilation of a photon with the frequency ω, momentum $\mathbf{k}$, and polarization σ ($\sigma = 1, 2$); $\mathbf{u}_{\mathbf{k},\sigma}$ are the unit vectors of polarization; $\mathbf{r}_a$ are the coordinates of atomic electrons; and $\widehat{\mathbf{p}}_a$ are the momentum operators of atomic electrons. In the dipole approximation, the amplitude of a photon emission with simultaneous transition of the atom from state φ_0 to state φ_n is

$$b_{0n}(\omega) = \left(\frac{2\pi}{\omega}\right)^{1/2} \mathbf{u}_{\mathbf{k},\sigma} \int_{-\infty}^{+\infty} dt \frac{\exp(it\omega)}{\omega}$$
$$\times \left\langle \varphi_n \left| \sum_a \frac{\partial V(t)}{\partial\mathbf{r}_a}\exp\left\{-i\int_{-\infty}^{+\infty} V(t')dt'\right\} \right| \varphi_0 \right\rangle. \qquad (9)$$

Upon summation of the amplitudes $|b_{0n}(\omega)|^2$ over polarizations, integration over the photon emission angles, and summation over all final atomic states φ_n, we obtain the total emission spectrum:

$$\frac{dW}{d\omega} = \frac{2}{3\pi}\frac{1}{c^3\omega}\left\langle \varphi_0 \left| \sum_a \frac{\partial \tilde{V}^*(\omega)}{\partial \mathbf{r}_a} \sum_{a'} \frac{\partial \tilde{V}(\omega)}{\partial \mathbf{r}_{a'}} \right| \varphi_0 \right\rangle, \quad (10)$$

where $c = 137$ is the speed of light and

$$\tilde{V}(\omega) = \int_{-\infty}^{+\infty} V(t)e^{i\omega t}dt. \quad (11)$$

Thus, we determined the total spectrum of emission from the atom during the time of action of the sudden perturbation $V(t)$. For $V(t)$ expressed by formula (2), the total emission spectrum is as follows:

$$\frac{dW}{d\omega} = \frac{2}{3\pi}\frac{1}{c^3\omega}\left|\tilde{\mathbf{E}}(\omega)\right|^2 N^2, \quad (12)$$

where N is the number of atomic electrons and $\tilde{\mathbf{E}}(\omega)$ is the Fourier image of the function $\mathbf{E}(t)$:

$$\tilde{\mathbf{E}}(\omega) = \frac{\sqrt{\pi}}{2\alpha}\mathbf{E}_0\left[\exp\left\{-\frac{(\omega-\omega_0)^2}{4\alpha^2}\right\} + \exp\left\{-\frac{(\omega+\omega_0)^2}{4\alpha^2}\right\}\right].$$

Using formula (9), it is also possible to obtain the spectrum of photons emitted with simultaneous transition of the atom from state φ_0 to an arbitrary state φ_n under the action of perturbation (2):

$$\frac{dW_{0n}}{d\omega} = \frac{dW}{d\omega}\left|\left\langle \varphi_n \left| \exp\left\{-i\mathbf{q}\sum_a \mathbf{r}_a\right\} \right| \varphi_0 \right\rangle\right|^2. \quad (13)$$

The total spectrum (12) has the form $dW/d\omega = \sum_n dW_{0n}/d\omega$, where the summation is performed over the complete set of atomic states. As follows from (4), the relative contribution of transitions with excitation of the atom to an arbitrary state φ_n is $dW_{0n}/dW = w_{0n}$. Therefore, Figs. 1 and 2 also present the corresponding relative contributions to the total pulse reradiation spectrum due to transitions with simultaneous excitation or ionization of a hydrogen or helium atom.

In order to determine cross sections for the pulse reradiation, according to [19], it is necessary to multiply spectra (10), (12), and (13) by ω and divide by the energy flux I expressed as the integral over time of the absolute value of the Poynting vector $S(t) = c(4\pi)^{-1}\mathbf{E}^2(t)$:

$$I = \int_{-\infty}^{+\infty} S(t)dt = \frac{c}{4\pi}\mathbf{E}_0^2\frac{\sqrt{\pi}}{2\sqrt{2}\alpha}\left(\exp\left\{-\frac{\omega_0^2}{2\alpha^2}\right\} + 1\right).$$

It is necessary to note an important feature of the emission under the action of a sudden perturbation:

according to (12) and (13), the intensity of emission for multielectron atoms is proportional to the number of atomic electrons squared, which is evidence of a coherent character of the process of ultrashort pulse reradiation.

REFERENCES

1. A. E. Kaplan and P. L. Shkolnikov, Phys. Rev. Lett. **88**, 074801 (2002).

2. A. Scrinzi and B. Piraux, Phys. Rev. A **56**, R13 (1997).

3. A. D. Kondorskiy and L. P. Presnyakov, J. Phys. B **34**, L663 (2001).

4. J. B. West, J. Phys. B **34**, R45 (2001).

5. J. Bauer, J. Plucinski, B. Piraux, *et al.*, J. Phys. B **34**, 2245 (2001).

6. G. Lagmago Kamta, T. Grosges, B. Piraux, *et al.*, J. Phys. B **34**, 857 (2001).

7. A. M. Dykhne and G. L. Yudin, Usp. Fiz. Nauk **125**, 377 (1978).

8. A. B. Migdal, *Qualitative Methods in Quantum Theory* (Nauka, Moscow, 1975; Benjamin, Reading, 1977).

9. L. D. Landau and E. M. Lifshitz, *Course of Theoretical Physics*, Vol. 3: *Quantum Mechanics: Non-Relativistic Theory* (Nauka, Moscow, 1989, 4th ed.; Pergamon, New York, 1977, 3rd ed.).

10. V. I. Matveev and É. S. Parilis, Usp. Fiz. Nauk **138**, 573 (1982) [Sov. Phys. Usp. **25**, 881 (1982)].

11. J. Eichler, Phys. Rev. A **15**, 1856 (1977).

12. G. L. Yudin, Zh. Éksp. Teor. Fiz. **80**, 1026 (1981) [Sov. Phys. JETP **53**, 523 (1981)].

13. V. I. Matveev, Fiz. Élem. Chastits At. Yadra **26**, 780 (1995) [Phys. Part. Nucl. **26**, 329 (1995)].

14. I. C. Percival, in *Atoms in Astrophysics*, Ed. by P. G. Burke, W. B. Eissner, D. G. Hummer, and I. C. Percival (Plenum, New York, 1983; Mir, Moscow, 1988).

15. A. J. Baltz, Phys. Rev. Lett. **78**, 1231 (1997).

16. A. J. Baltz, Phys. Rev. A **64**, 022718 (2001).

17. V. I. Matveev, Zh. Éksp. Teor. Fiz. **121**, 260 (2002) [JETP **94**, 217 (2002)].

18. V. B. Berestetskii, E. M. Lifshitz, and L. P. Pitaevskii, *Course of Theoretical Physics,* Vol. 4: *Quantum Electrodynamics* (Nauka, Moscow, 1989; Pergamon, New York, 1982).

19. L. D. Landau and E. M. Lifshitz, *Course of Theoretical Physics*, Vol. 2: *The Classical Theory of Fields* (Nauka, Moscow, 1973; Pergamon, Oxford, 1975).

Translated by P. Pozdeev

Interaction of a Simple Prandtl–Meyer Wave with a Weakly Vortexed Layer

A. V. Omel'chenko

St. Petersburg State University, St. Petersburg, Russia

e-mail: vmu@peterlink.ru

Received May 23, 2002

Abstract—The problem of interaction of a centered wave of rarefaction with a shear layer is solved in the case of a small flow vorticity in the shear layer. The solution is found in the form of an asymptotic series with respect to a small parameter of the problem. A system of equations derived in the zero approximation describes the flow in a simple wave. A uniformly applicable first-order expansion is constructed using the method of deformed coordinates. © 2002 MAIK "Nauka/Interperiodica".

Let us consider the interaction of a centered rarefaction wave *1* with a vortex (shear) layer *2* of finite thickness (Fig. 1). The region of interaction is bounded from the left by a weak discontinuity $A_1A_2A_3$ (which is a continuation of the weak discontinuity OA_1 separating the uniform flow and the Prandtl–Meyer wave) and from below by a weak discontinuity $A_1F_1C_1$ originating from point A_1 (the point of intersection of weak discontinuities OA_1 and QA_1). The Mach numbers M_1 and M_2 (in the regions below and above the shear layer, respectively), the distribution $M(y)$ of this number across the layer, and the slope angle φ_2 of a weak discontinuity OB_1 terminating the simple wave are considered to be preset.

The interaction of a simple wave with a shear layer is encountered in descriptions of supersonic streams [2] and shock waves interacting with simple waves [3] and in the problems of external aerodynamics [4, 5]. A small level of vorticity of the shear layers involved in these problems allows this factor to be ignored and the flow to be considered as potential. However, this simplification leads to physically incorrect consequences (see, e.g., [4]) and hinders adequate description of the flow pattern [2].

The main purpose of this paper is to obtain an analytical solution, with allowance for the flow vorticity, based on an asymptotic expansion of the gasdynamic functions with respect to a small parameter $\delta = \max_y |M(y) - M_1|/M_1$ characterizing the flow vorticity in the shear layer *2* (Fig. 1).

A flow in the region of interaction is described by a system of Euler equations. It is convenient to pass from this system to an extended system of equations [1]. For a flat supersonic flow, the new system is as follows:

$$\frac{\partial P_{1,2}}{\partial x} + \tan(\vartheta \pm \alpha)\frac{\partial P_{1,2}}{\partial y} = \pm\frac{\psi}{\cos^2(\vartheta \pm \alpha)}$$

$$\times [-M^2 P_{1,2}^2 - (2\mu - M^2)P_1 P_2 + 2\mu P_{1,2}P_3]$$

$$\pm Z\Bigg[\frac{-2P_1 P_2\cos\alpha}{\cos(\vartheta - \alpha)\cos(\vartheta + \alpha)}$$

$$+ \frac{P_1 P_3}{\cos(\vartheta + \alpha)\cos\vartheta} + \frac{P_2 P_3}{\cos(\vartheta - \alpha)\cos\vartheta}\Bigg],$$

$$\frac{\partial P_3}{\partial x} + \tan\vartheta\frac{\partial P_3}{\partial y} = \frac{P_3}{2\Gamma(M)\cos^2\vartheta}(P_2 - P_1),$$

$$\Gamma(M) = \frac{\gamma M^2}{A}, \quad A = \sqrt{M^2 - 1}, \tag{1}$$

$$\frac{\partial\vartheta}{\partial x} = \frac{P_2\tan(\vartheta - \alpha) - P_1\tan(\vartheta + \alpha)}{2\Gamma(M)},$$

$$\frac{\partial M}{\partial x} = \nu\Bigg[-P_3\tan\vartheta + \frac{P_2\tan(\vartheta - \alpha) - P_1\tan(\vartheta + \alpha)}{2}\Bigg],$$

$$\frac{\partial\vartheta}{\partial y} = \frac{P_1 - P_2}{2\Gamma(M)}, \quad \frac{\partial M}{\partial y} = \nu\Bigg[P_3 - \frac{P_1 + P_2}{2}\Bigg],$$

$$\nu = \frac{\mu}{(1 + \varepsilon)M}.$$

Here, ϑ is the slope of the flow velocity vector relative to the abscissa axis, $\alpha = \arcsin(1/M)$, γ is the adi-
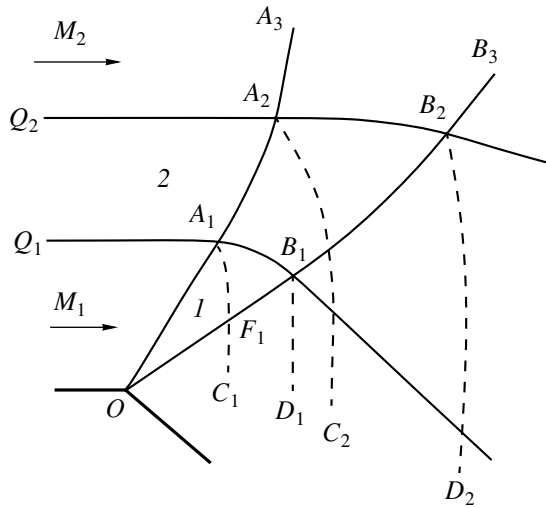
Fig. 1. A schematic diagram illustrating the interaction of a centered wave of rarefaction with a shear layer.

abate index, and

$$Z = \frac{(M^2-2)}{2(M^2-1)(1+\varepsilon)M^3}\frac{\mu}{}, \quad \psi = \frac{1}{2(1+\varepsilon)M^2\sqrt{M^2-1}},$$

$$\mu = 1 + \varepsilon(M^2-1), \quad \varepsilon = \frac{\gamma-1}{\gamma+1}.$$

The functions

$$P_{1,2} = \frac{\partial \ln p}{\partial y} \pm \Gamma(M)\frac{\partial \vartheta}{\partial y},$$

$$P_3 = \frac{\partial \ln p}{\partial y} + \frac{(1+\varepsilon)M^2}{\mu}\frac{\partial \ln M}{\partial y}$$

characterize the intensity of small perturbations propagating along characteristics of the first (P_1) and second (P_2) families and along the current lines (P_3). In particular, for a simple Prandtl–Meyer wave, $P_2 = P_3 = 0$ and

$$P_1 = \frac{2(1+\varepsilon)\sqrt{M^2-1}\cos^2(\vartheta+\alpha)}{x-c}. \quad (2)$$

Here, the constant c changes upon passage from one to another characteristic of the first family. For a centered wave, this value is constant over the wave and equal to the abscissa x_0 of the wave center (x_0, y_0). For wave *1* in Fig. 1, $x_0 = y_0 = 0$. In the shear layer *2*, which is parallel to the abscissa axis, $P_1 = P_2 = 0$ and P_3 is proportional to the vorticity:

$$P_3(y) = \frac{-1}{(\gamma-1)}\frac{dS(y)}{dy} = \frac{(1+\varepsilon)M(y)}{\mu(y)}\frac{dM(y)}{dy}, \quad (3)$$

where $M(y)$ and $S(y)$ are distributions of the Mach number and the entropy in the shear layer.

Let us seek a solution in the region of interaction in the following form:

$$f = \sum_{k=0}^{\infty} \delta^k f^{(k)}, \quad \delta \longrightarrow 0, \quad f \in \{A, \vartheta, P_1, P_2, P_3\}. \quad (4)$$

In the zero approximation, system (1) describes the flow in a centered Prandtl–Meyer wave with $P_2^{(0)} = P_3^{(0)} = 0$ and $P_1^{(0)}$ determined by formula (2). The quantities $\nu^{(0)}$ and $A^{(0)}$ are related to the Mach number M_1 of the uniform flow ahead of wave *1* and to the polar angle φ by the relations

$$\vartheta^{(0)} + \omega(M^{(0)}) = \omega(M_1),$$

$$A^{(0)} = \frac{1}{\sqrt{\varepsilon}}\tan(\sqrt{\varepsilon}[g(M_1)-\varphi]).$$

Now let us pass to a polar coordinate system in Eqs. (1), substitute series (4) into this system, and equate the terms at equal powers of δ. As a result, we obtain for the functions $f^{(1)}$

$$\frac{\partial P_3^{(1)}}{\partial \varphi} - r\cot(\varphi-\vartheta^{(0)})\frac{\partial P_3^{(1)}}{\partial r} = \alpha_3(\varphi)P_3^{(1)},$$

$$\frac{\partial P_2^{(1)}}{\partial \varphi} - r\cot(\varphi+\alpha^{(0)}-\vartheta^{(0)})\frac{\partial P_2^{(1)}}{\partial r}$$

$$= \alpha_{22}(\varphi)P_2^{(1)} + \alpha_{23}(\varphi)P_3^{(1)},$$

$$\frac{D^{(1)}}{r}\frac{\partial \vartheta^{(0)}}{\partial \varphi} + \frac{\partial \vartheta^{(1)}}{\partial r} = \alpha_{\vartheta 2}(\varphi)P_2^{(1)}, \quad D^{(1)} = \vartheta^{(1)} - \frac{A^{(1)}}{(M^{(0)})^2}, \quad (5)$$

$$\frac{D^{(1)}}{r}\frac{\partial A^{(0)}}{\partial \varphi} + \frac{\partial A^{(1)}}{\partial r} = \alpha_{A2}(\varphi)P_2^{(1)} + \alpha_{A3}(\varphi)P_3^{(1)},$$

$$\frac{D^{(1)}}{r}\frac{\partial P_1^{(0)}}{\partial \varphi} + \frac{\partial P_1^{(1)}}{\partial r} = \alpha_{11}(\varphi) + \alpha_{12}(\varphi)P_2^{(1)}$$

$$+ \alpha_{13}(\varphi)P_3^{(1)} + \alpha_{1\vartheta}(\varphi)\vartheta^{(1)} + \alpha_{1A}(\varphi)A^{(1)}.$$

System (5), as well as the initial system (1), is written in the invariant form [1]. In addition, the matrix in the right-hand part of (5) is triangular. These circumstances allow us to obtain an analytical solution to system (5) by sequentially solving the linear inhomogeneous first-order equations in partial derivatives with respect to functions $P_3^{(1)}$, $P_2^{(1)}$, $\vartheta^{(1)}$, $A^{(1)}$, and $P_1^{(1)}$.

It should be noted that the region of interaction is infinite in r. This circumstance leads to nonuniformity of the asymptotic expansion. Indeed, integration of the last three equations of system (5) along the characteristics of the first family leads to the appearance of secular terms of the type $r\alpha(\varphi)$ in the expressions for $\vartheta^{(1)}$, $A^{(1)}$,
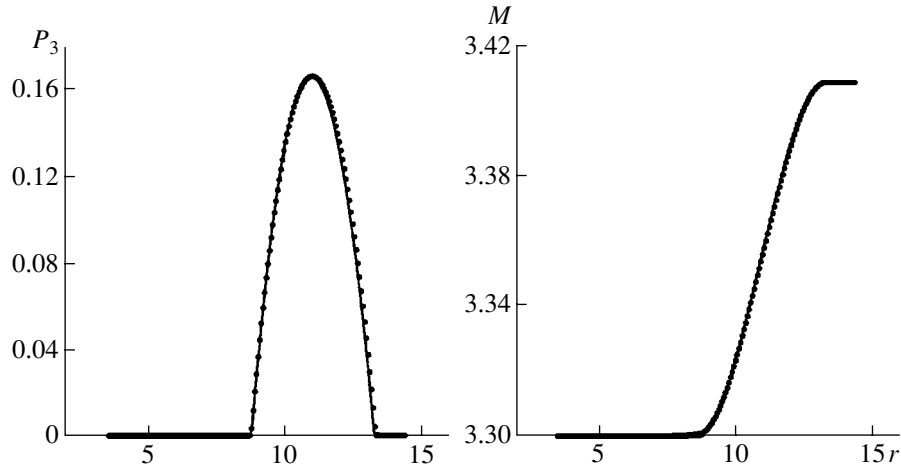
Fig. 2. A comparison of the results of analytical and numerical calculations (see the text for explanations).

and $P_1^{(1)}$, which makes the expansion inapplicable at large distances from the wall.

In order to obtain a uniformly applicable first approximation, let us employ the method of deformed coordinates [6, 7] and pass from (r, φ) to the new variables (s, t) using the formulas

$$\varphi = s + \delta \varphi_2(s, t) + \dots, \quad r = t.$$

As a result, the new equation for $\vartheta^{(1)}$ is

$$\frac{\partial \vartheta^{(1)}}{\partial t} - \frac{\partial \varphi_2}{\partial t} \frac{\partial \vartheta^{(0)}}{\partial s}$$

$$-\frac{1}{t} \frac{\partial \vartheta^{(0)}}{\partial s} \left(\varphi_2 - \vartheta^{(1)} + \frac{A^{(1)}}{(M^{(0)})^2} \right) = \alpha_{\vartheta 2}(\varphi) P_2^{(1)}.$$

By selecting φ_2 from the condition

$$\frac{\partial \varphi_2}{\partial t} + \frac{1}{t} \left(\varphi_2 - \vartheta^{(1)} + \frac{A^{(1)}}{(M^{(0)})^2} \right) = 0, \qquad (6)$$

we arrive at

$$\frac{\partial \vartheta^{(1)}}{\partial t} = 0 \longrightarrow \vartheta^{(1)} = \vartheta^{(1)}(s),$$

where the function $\vartheta^{(0)} + \delta \vartheta^{(1)}$ remains constant in the region above the vortex layer. Equation (6) can be rewritten as

$$\frac{\partial}{\partial t}(t\varphi_2) = \vartheta^{(1)} - \frac{A^{(1)}}{(M^{(0)})^2} \longrightarrow \varphi_2(s, t)$$

$$= \frac{1}{t}\tilde{\varphi}(s) + \frac{1}{t}\int_{t_0}^{t} \left[\vartheta^{(1)} - \frac{A^{(1)}}{(M^{(0)})^2} \right] dt.$$

At $t = t_0$, we obtain the flow in a simple wave with $\varphi = s$. For this reason, the arbitrary function $\tilde{\varphi}(s)$ in the last equation should be taken equal to zero. With this choice of $\tilde{\varphi}(s)$, the parametric variable s is determined by the implicit relation

$$\varphi = s + \frac{\delta}{t}\int_{t_0}^{t} \left[\vartheta^{(1)} - \frac{A^{(1)}}{(M^{(0)})^2} \right] dt + O(\delta^2). \qquad (7)$$

Figure 2 presents the results of calculations of the distribution of vorticity P_3 and the Mach number M on the terminal wave characteristic OB_3. These results were obtained for $M_1 = 3$, $M_2 = 3.1$, $M_{w1} = 3.3$, and a velocity profile in the vortex layer described by a cubic parabola. For these initial conditions, $\delta = 0.033$. Solid curves in Fig. 2 correspond to the data obtained using an asymptotic expansion, while dotted curves represent the values calculated by the method of characteristics. As can be seen from this figure, even the former approximation provides for a good coincidence with the exact calculation: the maximum relative error of determination of the Mach number was about 10^{-4}. It is interesting to note that an increase in the level of vorticity does not lead to a catastrophic growth in the error. Indeed, for a Mach number of $M_2 = 4$, the parameter δ is 0.33 and the maximum relative error of determination of the Mach number is on the order of 10^{-2}.

Conclusion. We have demonstrated that the problem under consideration belongs to the class of singularly perturbed problems of vortex gasdynamics. A uniformly applicable first approximation was obtained using the method of deformed coordinates.

REFERENCES

1. B. L. Rozhdestvenskiĭ and N. N. Yanenko, *Systems of Quasilinear Equations and Their Applications to Gasdynamics* (Nauka, Moscow, 1968).

2. A. E. Medvedev and V. M. Fomin, Prikl. Mekh. Tekh. Fiz. **39** (3), 52 (1998).

3. H. Li and G. Ben-Dor, AIAA J. **34** (2), 418 (1996).

4. W. D. Hayes and R. F. Probstein, *Hypersonic Flow Theory* (Academic, New York, 1959; Inostrannaya Literatura, Moscow, 1962).

5. G. G. Chernyĭ, *Gas Flows with Fair Supersonic Speed* (Fizmatgiz, Moscow, 1959).

6. A. H. Nayfeh, *Introduction to Perturbation Techniques* (Wiley, New York, 1981; Mir, Moscow, 1984).

7. M. Van Dyke, *Perturbation Methods in Fluid Mechanics* (Academic, New York, 1964; Mir, Moscow, 1967).

Translated by P. Pozdeev